TÉCNICO LISBOA

Sizing and Integration of an Electric Propulsion System for a VTOL UAV

Sara de Almeida Pedro

Thesis to obtain the Master of Science Degree in

Aerospace Engineering

Supervisors: Prof. Afzal Suleman
Dr. José Lobo do Vale

Examination Committee

Chairperson: Prof. Fernando José Parracho Lau
Supervisor: Prof. Afzal Suleman
Member of the Committee: Prof. Pedro Vieira Gamboa

January 2021

To my one and only. Couldn't have done it without you...

Acknowledgments

I would like to start by thanking my grandfather for the countless afternoons teaching me all he knew, for introducing me to the wonders of maths and physics at an early age and making me want to become an engineer. It is to him that I owe most of my academic success.

I'm very grateful to my parents for the emotional encouragement and financial support throughout my academic journey. You have motivated me to keep trying and taught me the values I guide myself by. Making you proud has always been a great source of motivation that inspired me to try and reach beyond what is comfortable, challenging me.

A special thank you goes to Dr. Afzal Suleman, for the opportunity he gave to me as well as for the support throughout this journey in Canada. Without him this whole experience wouldn't have been possible.

I'm grateful to Dr. José Vale for all the advice and expertise given to me as well as the numerous rides to work. He has taught me how to carry out research and it was a privilege working by his side. His orientation throughout this process is invaluable.

A warm thank you goes to all the guys at the Centre for Aerospace Research and especially to all working on the Mini-e. It took the contributions of all of us to accomplish this project.

Finally, I'd like to thank the University of Victoria for it's endorsement during the development of my thesis and Instituto Superior Técnico for the education it gave me during these five years.

Resumo

As vantagens dos sistemas de propulsão de VTOL (vertical take-off and landing) elétricos levaram ao desenvolvimento de veículos aéreos não tripulados (UAVs) com essa capacidade. Esta tese apresenta o design do sistema de propulsão de quatro UAVs e-VTOL, avaliando a massa e o consumo de energia das configurações lift-and-cruise e vectored-thrust.

Com o objetivo de diminuir a interferência magnética, o estudo da distribuição assimétrica de propulsão para quadrotores e trirrotores foi realizado, concluindo que para a missão definida, o uso de menos motores tem um impacto maior no peso total do sistema do que a eficiência das configurações, tornando a configuração vectored-thrust tri-rotor a de melhor desempenho. Em relação à eficiência, verificou-se que dimensionar o sistema para VTOL, rodando os rotores traseiros para voo retilíneo não tem um impacto negativo na energia necessária para a missão.

Adicionalmente, foram realizados estudos sobre a interferência asa-rotor, determinando que, para uma força necessária dos rotores, a distância mínima entre as superfícies pode ser calculada conhecendo a percentagem de área coberta do rotor.

Os métodos aplicados para a escolha do sistema de propulsão incluem vortex propeller theory e a teoria da hélice de Corke, enquanto que a interferência asa-rotor foi estimada com estudos CFD. O desempenho estimado das configurações foi então comparado com o seu desempenho experimental através de testes estáticos, tendo-se obtido resultados semelhantes.

Finalmente, um modelo dinâmico foi desenvolvido, confirmando que as configurações eram estáveis e controláveis, antes da realização de um voo pairado da aeronave desenvolvida.

Palavras-chave: e-VTOL, propulsão eléctrica, UAV, interferência asa-rotor

Abstract

The advantages of electric vertical take-off and landing (e-VTOL) propulsion systems for military applications have led to the development of unmanned aerial vehicles (UAVs) with this capability. This thesis presents the propulsion system sizing of four e-VTOL UAVs, assessing the mass, power consumption and installed power for lift-and-cruise and vectored-thrust configurations, for a magnetic anomaly detection application.

A study of asymmetric thrust distributions for quadrotors and tri-rotors was performed in order to decrease magnetic interference, concluding that for the defined mission, the use of fewer motors has a higher impact on the total system weight than the efficiency of the configurations, making the vectored-thrust tri-rotor configuration the best performing of all. Regarding efficiency, it was found that sizing the system for VTOL and tilting the rear rotors for forward-flight does not have a negative impact on the required energy for the mission.

Additionally, studies on wing-rotor interference were conducted, determining that, for a required minimum relative net force from the rotors, a minimum distance between surfaces can be calculated knowing the percentage of rotor covered area.

The methods applied for propulsion sizing include vortex theory and Corke's empirical method, while CFD studies were completed to determine wing-rotor interference. The estimated performance of the configurations was then compared with their experimental performance through static tests, rendering similar results.

Finally, a dynamic model was developed, confirming the configurations were stable and controllable, prior to an indoor hover test of the manufactured UAV.

Keywords: e-VTOL, electric propulsion, UAV, wing-rotor interference

I declare that this document is an original work of my own authorship and that it fulfills all the requirements of the Code of Conduct and Good Practices of the Universidade de Lisboa

Contents

List of Tables

List of Figures

.

Nomenclature

Greek symbols

α	Boom rotation angle
β	Boom angle.
β_r	Aerodynamic pitch angle at blade tip.
ϵ_b	Downwash angle.
ϵ_i	Induced angle.
η	Efficiency.
Γ	Circulation.
ω, Ω	Angular velocity.
ϕ, θ, ψ	Euler angles.
ρ	Density.
σ	Blade solidity.

Roman symbols

A	Area.
c	Chord.
C_τ	Torque coefficient.
C_d	Coefficient of drag.
C_l	Coefficient of lift.
C_T	Thrust coefficient.
C_{d_0}	Blade drag coefficient
$C_{d_{\alpha_0}}$	Zero angle of attack drag coefficient
D	Drag.

d	Diameter.
F	Force.
f	Tip loss factor.
I	Inertia
K_τ	Torque constant.
k_i	induced power factor.
K_T	Thrust constant.
m	Mass.
M	Moment.
p	Pressure.
p, q, r	Angular Velocity components.
P	Power.
p	Pressure.
R	Radius.
S_c	Canard surface area.
S_f	Fuselage surface area.
S_w	Wing surface area.
T	Thrust.
$\mathbf{V}$	Velocity vector.
u, v, w	Velocity Cartesian components.
W	Weight.
x, y, z	Position Cartesian components.

Subscripts

0	Trim condition
∞	Free-stream condition.
θ	Tangential direction
B	Body.
b	Blade.

c Climb.

d Downstream.

f Front

p Blade.

p Propeller.

r Rear.

u Upstream.

x Axial direction

x, y, z Cartesian components.

x_a, y_a, z_a Cartesian Aerodynamic components.

x_p, y_p, z_o Cartesian Propulsion components.

xx, yy, zz, xz Inertia tensor components.

i Induced component.

ref Reference condition.

Superscripts

T Transpose.

Chapter 1

Introduction

1.1 State of the Art

The history of unmanned aerial vehicles (UAVs) dates back to World War I, to gather and transmit real-time information from hostile areas without endangering aircrew. Those early models suffered from landing and stabilization issues, which resulted in their progress being slower when compared to that of manned aviation, with other factors such as insufficient cost-effectiveness and lack of investment backing. It would not be until the state of the art progressed in automatic stabilization, remote-control, and autonomous navigation that UAVs would become a viable alternative to manned aircraft [1]. The development of multirotor manned aircraft happened simultaneously with that of UAVs, backdating to 1907 with the Breguet-Richet Gyroplane, the first quadrotor. However, it took almost half a century more to develop a rotary-wing vehicle that allowed different thrust per rotor to perform manoeuvres without additional rotors - the Convert wings Model A. Figure 1.1 presents these aircraft.

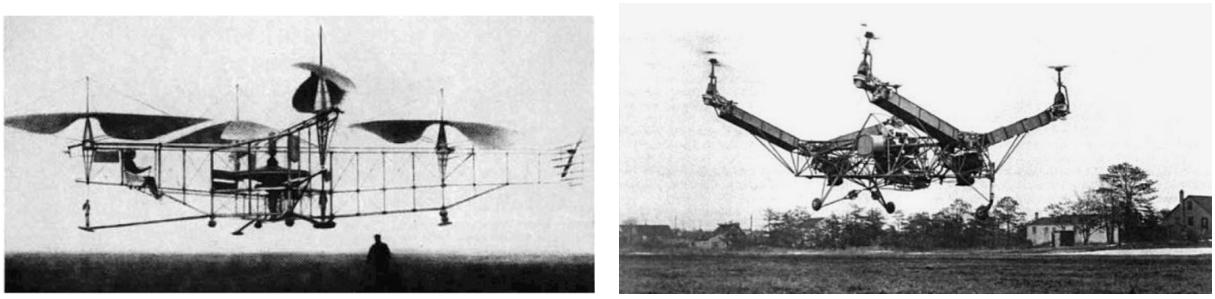

(a) Breguet-Richet [2] (b) Convertawings [3]

Figure 1.1: The first quadrotors

As UAVs evolved, new developments would fit into one of three categories: fixed-wing, rotary-wing, and flapping wing [4] [5] [6] [7]. While the first is destined towards long-range, long-distance, and high-altitude roles, rotary wings are used for missions that require the ability to hover as they are less susceptible to air turbulence. Flapping wing UAVs, on the other hand, are low-payload, low-power, low-endurance devices with vertical take-off and landing (VTOL) capability.

Through the available UAV configurations, electric vertical take-off and landing (eVTOL) [8] capability is one of the most common features, as it combines the negligible variation in efficiency at different dimensions of electric motors with the ability to take-off without a runway [9][10]. More specifically, the decrease in efficiency of gas engines as they are scaled down united to the added weight make electric propulsion a favourable choice for small scale UAVs [11]. To that point, over 130 eVTOL concepts have been proposed in categories such as vectored thrust, lift-and-cruise and wingless over the last few years. While both the first and second categories feature a fixed-wing, their major difference is the use of the same rotors for VTOL and forward flight in vectored thrust, against the dedicated rotors for each flight segment in lift-and-cruise. Wingless UAVs are multirotor concepts [12] [13].

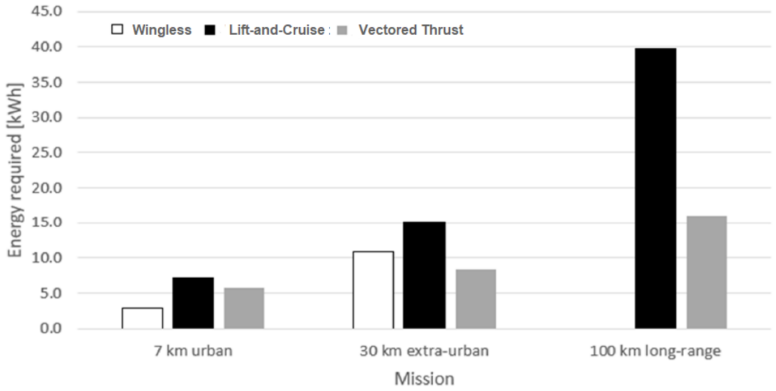

Figure 1.2: Energy consumption of eVTOL configurations per mission range [14].

Bacchini and Cestino [14] have determined that the efficiency of the chosen configuration depends on the ratio of VTOL to cruise flight time, as vectored thrust better performs in long-range missions, where cruise is predominant, and wingless are better for short-range missions, where the VTOL and cruise flight times are balanced. Lift-and-cruise concepts are a compromise between both. Figure 1.2 presents the energy required per mission range for the three aforementioned types of configurations.

While choosing the right configuration highly impacts mission performance, sizing the propulsion system itself also plays a major role in achieving an efficient design. Therefore, the propulsion system's two main components - propeller and motor - determine the overall efficiency of the system.

In electrically-propelled UAVs , brushless DC motors are the most common choice, as the lack of brushes decreases maintenance costs. The sizing of the motor depends on the mission and configuration, as the required thrust-to-weight ratio per motor will dramatically increase with manoeuvres [15][16] [17][18]. Since take-off is the most demanding flight stage, requiring the highest thrust-to-weight ratio, it dictates the motor selection in vectored thrust configurations. However, motors for lift-and cruise configurations can be sized according to the flight stage they perform.

On the other hand, propeller choice hinges on design priority, as performance and efficiency can be traded for stealth or even compliance with a specific motor. Assuming a design to maximize thrust output, while maintaining a power consumption compatible with the chosen motor, around a specific design point, parameters such as thrust and power coefficients, in addition to efficiency indicate performance [19]. These are dependant on advance ratio and pitch, as presented in figure 1.3.

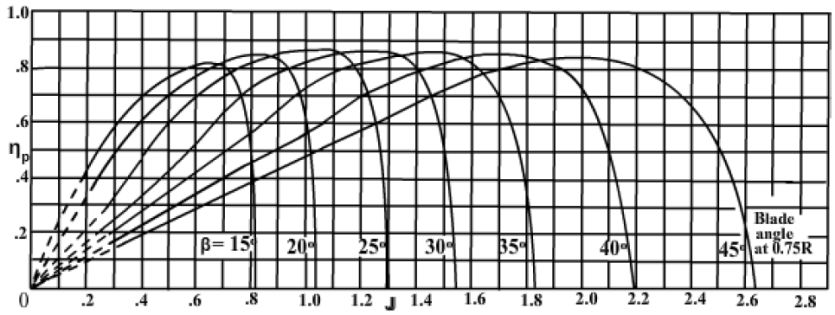

Figure 1.3: Efficiency (η_P) vs advance ratio (J) for different pitch (β) values for two bladed propellers [20].

Pitch is a critical parameter for a propeller, as it highly affects performance. Considering efficiency peaks at a specific advance ratio, for a given fixed-pitch propeller, the choice is often a compromise between the pitch that maximizes performance for take-off and the one that maximizes efficiency for cruise [21]. Alternatively, variable-pitch propellers offer the benefit of adjusting their pitch to the flight condition, increasing the overall efficiency of the system. Taking into account that the use of a variable-pitch propeller results in a heavier, more complex structure, their application is most effective in tilt-rotor configurations, where the same propeller is operated at different flight conditions [22] [23] [24]. Figure 1.4 presents how fine changes in pitch can result in a peak propeller efficiency throughout a large range of airspeed.

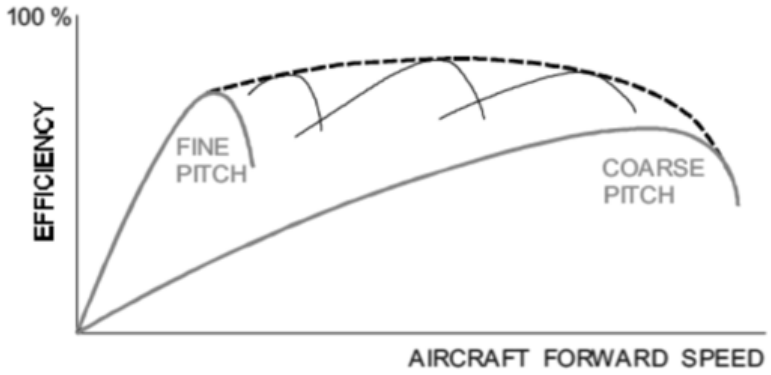

Figure 1.4: Illustration of the effect of variable-pitch [25]

.

When considering fixed-pitch propellers, optimized design methods can be applied to increase the system's efficiency. These have a large range of both complexity and accuracy, going from blade element methods, passing by vortex methods, to numerical ones [26] [27] [28]. The simplest axial momentum theory was developed by Rankine and Froude, modelling the rotor as an infinitely thin, finite area, actuator disc. Its simplicity didn't account for blade geometry, which made blade element methods more accurate, while still requiring correction factors for induced velocity. These correction factors originated blade element momentum methods (BEM) [29] [30] [31], the most accurate of the above. Vortex theory is another valid approach for optimized propeller design [32] [33] [34], started by Prandt [35] with his fixed-wing theory, that ultimately let to Betz's rigid wake condition [36] [37]. Later on, Goldstein [38] [39] was able to determine an exact solution that was built on by both Theodorsen and Larrabee to produce

a straightforward process to optimized propeller design.

Piancastelli [40], in a recent paper, compared Larrabee's [41] [42] and Theodorsen's methods, concluding that Larrabee's renders thin blades with a very large chord that are more efficient but also heavier, while Theodorsen's generates tapered blades where the maximum chord section is closer to the hub . Figure 1.5 presents geometry obtained by application of Larrabee and Theodorsen's methods.

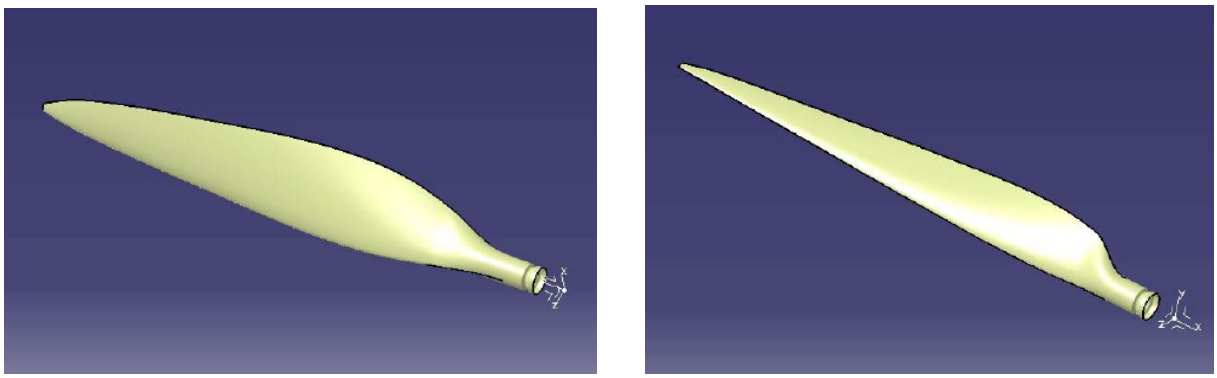

(a) Larrabee [40]

(b) Theodorsen [40]

Figure 1.5: Comparison of geometries obtained with propeller design methods

While propeller optimized design increases the overall efficiency of the propulsion system, a multidisciplinary optimization (MDO) of the whole system delivers better results, as it can take into account not only the aerodynamic effects of the propeller's geometry but also noise signature, structural considerations, motor and battery performance [8]. An alternative to MDO studies is parametric studies using computational fluid dynamics (CFD) software.

Currently, CFD software is used to determine propeller behaviour and assess performance by solving the Reynolds-Averaged Navier-Stokes (RANS) equations [43] . Since the RANS method is computationally costly, BEM methods can be coupled with RANS for quicker solutions without significantly compromising in accuracy [44].

CFD analysis allows the study of more complex problems and flow conditions, such as the interaction between rotor and wing. In hybrid - fixed-wing VTOL - UAV configurations [45], due to the positioning of both rotors and wing, these can overlap, interfering in each other's performance. Rotor coverage CFD analysis is particularly interesting to compare against available empirical/experimental data, quantifying the decrease in rotor performance by wing proximity [46]. Figure 1.6 presents the experimental data and setup obtained by Chen in a recent paper [47], where he concluded that as the rotor is lowered towards the wing, the thrust ratio increases up to 33%, at a quarter radius of vertical distance.

Granting that optimized propulsion design can increase efficiency and performance, there are some other fundamental aspects to be considered in order to achieve a successful mission. For instance, parameters derived from control, like perceiving the environment, analyzing the sensed information, communicating, path planning and manoeuvre performance as well as basic dynamic stability should be investigated when evaluating the UAVs behaviour. The controller addresses this topic, predicting and adjusting the UAVs attitude by managing the actuators [48].

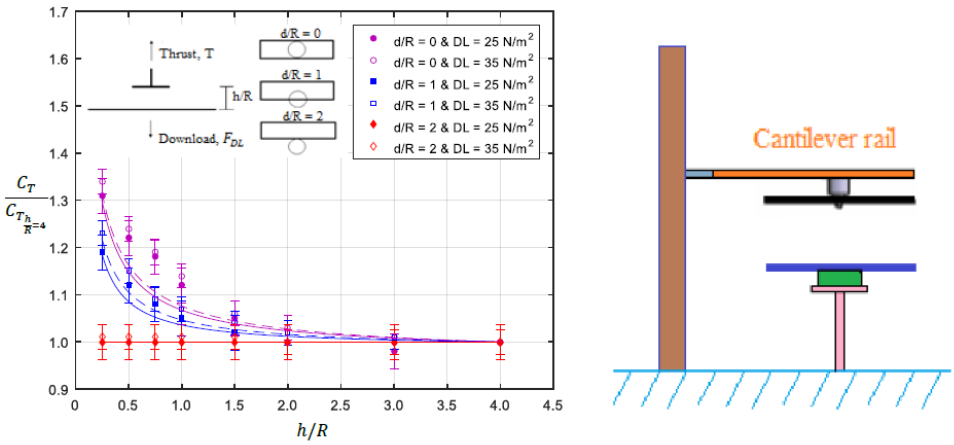

Figure 1.6: Chen's experimental results on rotor-wing interference [47]

Multicopters, specifically quadcopters, present a particular challenge control-wise, as they are underactuated systems, unstable in open loop, requiring extra labour to balance and reach the desired attitude [49] [50]. These difficulties can be addressed by control schemes categorized as linear, nonlinear or learning-based intelligent, as shown in figure 1.7.

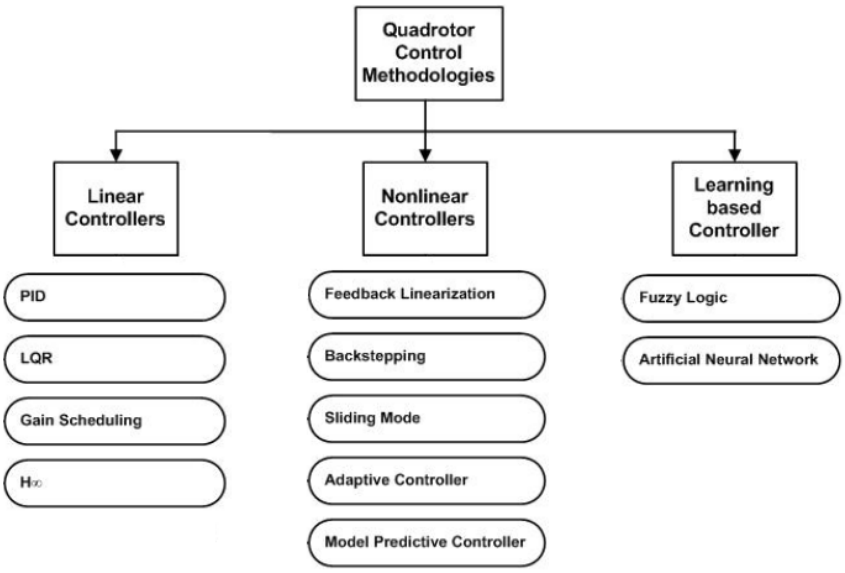

Figure 1.7: Different quadrotor control methodologies [51]

Linear controllers have been widely used in quadrotor applications due to their ease of design and implementation, rendering good experimental results. The most common linear controller is the PID (proportional integrative derivative), considering it can be applied without knowing the dynamic model and tuned by trial and error [52] [53] [54] [55] [56]. These controllers are well suited for a stationary or quasi-stationary flight where the dynamics are approximately linear, but have issues with disturbances and manoeuvres, inducing large errors in the system that affect the transient response, presenting weaker robustness and yielding large tracking errors. These issues have been addressed by Czyba [52], introducing different PID structures by moving either the derivative term or both the derivative and propor-

tional terms to feedback, as well as by Wang [57], that introduced cascade PID controllers to effectively improve robustness when compared to regular PIDs. These controllers have also been applied in combination with linear quadratic regulators (LQR) [58] for a more robust controller, improving performance and efficiency.

Since linear controllers suffer when the quadrotor is operating outside of the designated regime, a combination of linear and nonlinear models can frequently be found in the literature, including gain scheduling [59] and $H\infty$ methods, as well as nonlinear methods [60] [61].

Nonlinear methods offer better robustness, disturbance rejection and trajectory tracking, yet their high computational costs to implement hinder their progress [62]. The most common nonlinear method is backstepping, for its fast convergence rate and great responses to external disturbances, achieving inner loop stability for both attitude and altitude. Other methods, such as model predictive controller (MPC) [63] [64], along with the adaptive controller [65], and sliding mode controller (SMC) [66], have also shown better performance when compared to linear methods.

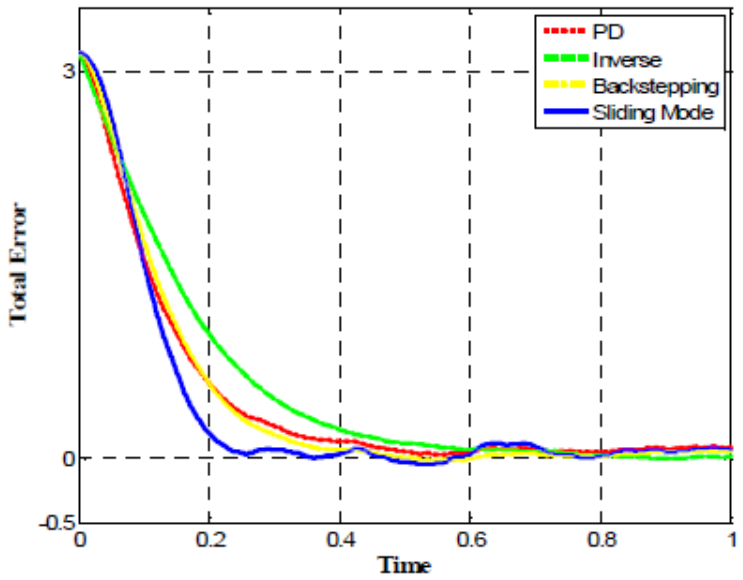

Figure 1.8: Control Methods Comparison [67]

Figure 1.8 presents a comparison of linear and nonlinear methods published by Dikmen [68], where SMC methods converge significantly faster than backstepping and PD [69]. It is also common to find combinations of nonlinear methods, as the adaptive integral backstepping controller as well as learning-based methods [70] [71].

The latter is trained via data obtained and validated through flight experiments, enabling the controller to be used in different UAV configurations. This approach is well suited for models where the dynamics are not well known, since it is model-free, yet the high computational costs, increased complexity and unavailability of training data has limited these methods to simulation work [72].

.

1.2 Motivation

The pressure from resource scarcity and environmental concerns on the industry of today has resulted in alternative propulsion systems garnering renovated attention [73]. Electrically-propelled, high-efficiency vehicles offer an answer to this paradigm shift [15].
This fundamental change has made UAVs an attractive investment, resulting in numerous developments in the area. Military grade surveillance is one of the new purposes that rose from such innovations. To thrive in this field, low heat and noise signatures as well as efficiently sized propellers and weight management have to be implemented [74]. Additionally, the current interest in urban air mobility (UAM) [75] has stimulated major aviation companies to put their electric VTOL prototypes forward, further propelling the field. As a result, the focal point of these vehicles becomes the propulsion system [76].
As such, experimenting with different propulsion architectures and configurations, determining which one best fits a specific mission type is highly useful for both current and future applications.

1.3 Project Overview and Requirements

Under the authority of Defence and Research Department Canada (DRDC), the Center for Aerospace Research (CfAR) and Quaternion Aerospace are developing a UAV with vertical take-off and landing capability to monitor the Canadian coast, surveilling passing submarines with a magnetic signature sensor, the MAD-XR.
The end goal of this project is to achieve an efficient design featuring a canard and tilt tri-rotor configuration. The propulsion system should have two rotors at the front, producing twenty percent of thrust and a rear rotor that produces the remaining, tilting for forward-flight. This distribution of power allows the front rotors to be further from the magnetic sensor, decreasing the interference between the two.
To achieve this, the project was divided into four stages propulsion-wise: starting with a regular quadrotor lift-and-cruise configuration, evolving it into an 20-80 VTOL power distribution, changing this 20-80 from lift-and-cruise to vectored-thrust and finalizing with a trirotor configuration, tilting the rear rotor for forward-flight.
As a proof of concept, scaled down prototypes are being developed, resembling the four stages of the full scale aircraft as much as possible. This thesis focuses on the propulsion system's evolution, sizing, analysing, building and comparing the small scale UAVs, while respecting a few requirements.
In order to maintain the proof of concept UAVs similar to the full scale aircraft, the prototypes would have the same ratio between cruise and dash speed, as well as a the same lift and thrust distributions. Additionally, it would have to carry a small magnetic sensor, while maintaining a maximum take-off weight (MTOM) of seven kilograms.
Regarding specific propulsion requirements, the system must be fully electric, functioning with one battery only - all motors must work with the same voltage. Also, the VTOL system would have to satisfy a minimum maximum thrust-to-weight ratio of 1.3, take-off thrust-to-weight ratio of 1.05, and a maximum propeller diameter of fifteen inches. Other, more specific requirements will be displayed later on.

1.4 Objectives

The purpose of this thesis is to size the propulsion system for VTOL and forward-flight of the four scaled down prototype UAV's. To that end, all four configurations will be designed and compared against each other, determining which best fits the mission.
In addition, this thesis aims to prove that an asymmetric propulsion distribution in VTOL is favourable when compared to the usual system, especially when progressing to a tilt-rotor instead of a lift-and-cruise configuration.
To reach a conclusion in this matter, studies will be performed comparing size, weight, efficiency, performance, stability and dynamic response.
To validate the used models, one of the scaled down prototypes will be developed and flown, gathering data to compare with the estimated performance.

1.5 Thesis Outline

Chapter 2

This chapter contains the theoretical concepts used to develop the thesis. In the first instance, it presents the necessary approach to size the VTOL system, choosing the adequate motor, propeller and electric speed controller (ESC). Afterwards, it explains the methods used to estimate the required power for forward flight, facilitating the choice of the motor-propeller combination.
This chapter also contains some of the theory behind the used software for computational fluid dynamics (CFD) analysis, justifying some of the applied simulation parameters, and introduces the procedure used to develop the flight dynamics model (FDM) and the controller.

Chapter 3

This chapter contains the parametric studies performed on both the rotor positioning and the T/W ratio, that led to the chosen configurations. Additionally, it describes the four configurations in detail, explaining the requirements for each rotor as well as the process for it's selection and validation.
Afterwards, it presents the expected energy consumption of each configuration, based on data from the manufacturers, in order to assess the required battery and lists all the components used to estimate the propulsion the system's mass. Finally, it presents a computational study for wing-rotor interference to compute the required distance as a function of rotor coverage.

Chapter 4

This chapter contains the results of the static tests performed to validate the performance of the selected propulsion system, describing the setup and the software used. It compares the results with the ones obtained through theoretical models, in the previous chapter. Additionally, it presents studies done with partially covered rotors to determine the required wing-rotor distance as a function of covered area.

Finally, it presents the thrust and torque constants computed from experimental results to be used in the flight dynamics model.

Chapter 5

This chapter contains the flight dynamics model (FDM) derived to compare against the experimental hover tests. It describes the SIMULINK® model as well as all the assumptions made during its development, showcasing the different steps taken to ensure a satisfactory degree of accuracy. Additionally, it explains the tuning process and the methodology to calculate actuator inputs. Finally, it shows the results achieved with step commands to the system, for the modeled configurations.

Chapter 6

This chapter describes the procedure established to perform the different flight tests, explaining the necessary commissioning required by Transport Canada (TA), as well as the safety measures and flight protocol. It compares the experimental data with the estimated from models and static tests, assessing the propulsion system's performance.

Chapter 7

This chapter recapitulates the previous chapters, assessing the overall performance of the propulsion system against the objectives set in the beginning of the project. It contains a review of the work done and lists the next steps that should be taken, proposing alterations to the current propulsion system to increase performance.

Chapter 2

Theoretical Background

This chapter presents the theoretical notions used in the development of the UAV's propulsion system, for both sizing and performance evaluation, as well as the methodology to develop the flight dynamic model and implement the controller.

2.1 Propeller Design

Development of propeller theory has advanced from the simple leadscrews from Da Vinci [77], to actuator disks, reaching the complex vortex theories of Betz, Goldstein, Theodorsen and Larrabee. Figure 2.1 presents an illustration of Betz's wake model as well as the values that Goldstein obtained for circulation as a function of the radius.

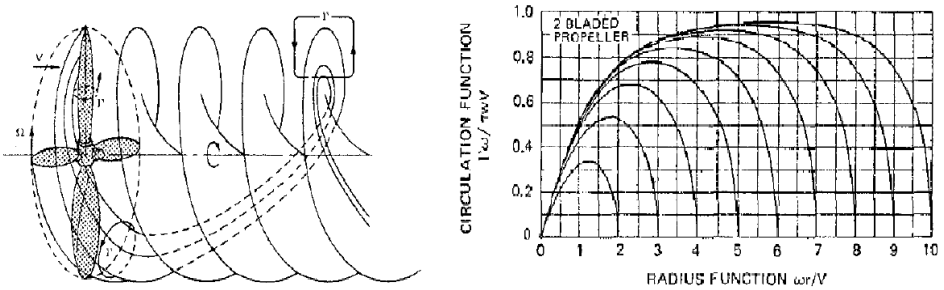

Figure 2.1: Betz's propeller wake model and Goldstein's typical results [77]

2.1.1 Corke's Propeller Design for Cruise

The sizing of the pusher propeller was done, in an initial stage, with Corke's methodology. This method is an empirical approach that assumes a known altitude and Mach number for cruise, as well as propeller diameter and estimated motor shaft power. By application of this method, the propeller's advance ratio and efficiency can be computed, in addition to both power and thrust coefficients. This process assumes a three-bladed propeller, requiring additional corrections for propellers with a different number of blades.

In the selection process, equation 2.1 was used to estimate efficiency [78].

$$\eta_p = \frac{TV}{P}, \tag{2.1}$$

where *T* is the required thrust in N, *V* is the velocity in m/s, *P* is the required power by the propeller in W and η_p is the propeller's efficiency.

2.1.2 Vortex Theory of Screw Propellers

Vortex theory of screw propellers assumes there is circulation around the blade, that vanishes at root and tip, and can be replaced by a bound vortex system of strength Γ, the circulation round the blade section. From the bound vortex, trailing free vortices are shed, building a helical or screw surface - helical sheet.

This approach allows the performance assessement of propellers of known geometry as well as the design of propellers optmized for a specific design point - such as cruise condition. Figure 2.2 presents some of the important geometrical parameters used in this theory [79].

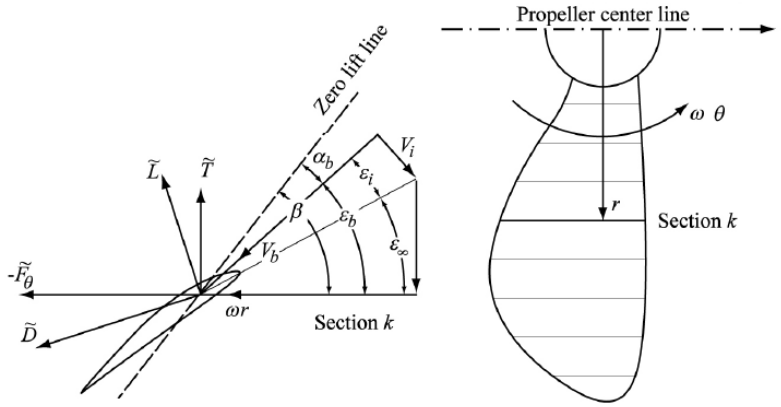

Figure 2.2: Geometry of the vortex theory for screw propellers [79]

The incident velocity on the blade, V_b can be decomposed into free stream velocity V_∞, induced velocity V_i and rotational velocity ωr. The induced velocity contains V_{xi}, in the axial direction and $V_{\theta i}$ in the tangent direction.

$$V_b{}^2 = \omega^2 r^2 \left[\left(1 - \frac{V_{\theta i}}{\omega r} \right)^2 + \left(\frac{V_\infty}{\omega r} + \frac{V_{xi}}{\omega r} \right)^2 \right] \tag{2.2}$$

Equation 2.2 relates the blade incident velocity with the remaining ones, where ω is the blade's rotational speed and *r* is the radial coordinate.

Knowing the blade section's 2D drag, C_d, and lift, C_l, coefficients as well as the section's chord, c_b, differential thrust and torque can be computed, as show in equations 2.3 and 2.4.

$$\frac{dT}{dr} = \frac{n_{blades}}{2} \rho c_b \omega^2 r^2 \left[\left(1 - \frac{V_{\theta i}}{\omega r} \right)^2 + \left(\frac{V_\infty}{\omega r} + \frac{V_{xi}}{\omega r} \right)^2 \right] (C_l \cos \varepsilon_B - C_d \sin \varepsilon_B) \tag{2.3}$$

$$\frac{dQ}{dr} = \frac{n_{blades}}{2}\rho c_b \omega^2 r^3 \left[\left(1 - \frac{V_{\theta i}}{\omega r}\right)^2 + \left(\frac{V_\infty}{\omega r} + \frac{V_{xi}}{\omega r}\right)^2\right](C_d \cos\varepsilon_B + C_l \sin\varepsilon_B) \tag{2.4}$$

In order to obtain the overall thrust and torque by integration, both the induced angle ε_i and the downwash angle ε_B must be known. These parameters can be derived from Betz's principle - $V_{\theta i}$ is normal to the resultant velocity - combined with the geometrical relations present on Figure 2.2. Equations 2.5 and 2.6 represent these relations.

$$V_b = \frac{\omega r}{\cos\varepsilon_\infty}\cos\varepsilon_i \tag{2.5}$$

$$V_i = \frac{\omega r}{\cos\varepsilon_\infty}\sin\varepsilon_i = \sqrt{{V_{\theta i}}^2 + {V_{xi}}^2} = \sqrt{[V_i \sin(\varepsilon_i + \varepsilon_\infty)]^2 + [V_i \cos(\varepsilon_i + \varepsilon_\infty)]^2} \tag{2.6}$$

The circulation, Γ, can be calculated with Prandtl's tip loss factor, *f*, where β_r is the aerodynamic pitch angle at the blade tip, combined with Goldstein's relation between $V_{\theta i}$ and the section's circulation.

$$f = \frac{2}{\pi}\cos^{-1}\left[exp\left(\frac{n_{blades}(1 - 2r/r)}{2\sin\beta_r}\right)\right] \tag{2.7}$$

$$n_{blades}\Gamma = 4\pi f r V_{\theta i}. \tag{2.8}$$

Solving the equations above for ε_i, all the variables are known to accurately calculate both torque and thrust, by integration, as well as the consumed power, for a lightly loaded propeller.

2.1.3 Propeller Momentum Theory

Propeller momentum theory assumes that a streamtube encloses the propeller, extending to planes far upstream and downstream that are parallel to the propeller [80]. The flow, of constant velocity and pressure across each streamtube section, enters the upstream plane of the streamtube, passes the propeller and exits at the far downstream plane, as shown in figure 2.3.

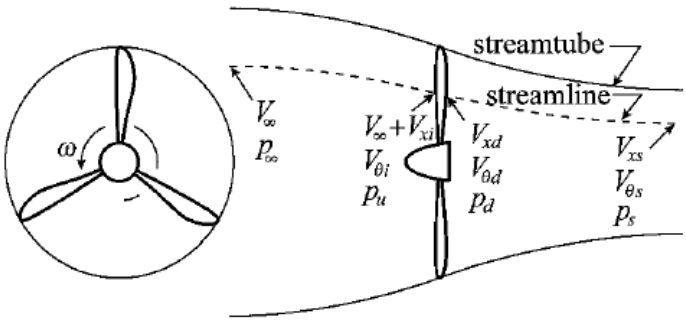

Figure 2.3: Propeller momentum theory model [80]

Like vortex theory, this model assumes an inviscid and incompressible flow, yet it neglects any fluid rotation [81].

Considering the velocity upstream of the propeller is given by $V_\infty + V_i$, the free stream velocity and the induced velocity, respectively, the velocity on the dowstream of the propeller V_d can be obtained from

mass conservation.

$$\rho V_d A_p = \rho(V_\infty + V_i)A_P \Rightarrow V_d = V_\infty + V_i \tag{2.9}$$

By application of Bernuilli's principle both upstream and dowstream of the propeller,

$$\frac{{V_s}^2 - {V_\infty}^2}{2} = \frac{p_d - p_u}{\rho}, \tag{2.10}$$

where V_s is the slipstream velocity, p_d is the downstream pressure, p_u is the upstream pressure, A_p is the disk area and ρ is the air density.
The thrust and brake power can be calculated with equations 2.11 and 2.12,

$$T = 2A_p\rho(V_\infty + V_i)V_i, \tag{2.11}$$

$$P = 2A_p\rho(V_\infty + V_i)^2V_i. \tag{2.12}$$

Solving equation 2.11 for the induced velocity,

$$V_i = \sqrt{\frac{{V_\infty}^2}{4} + \frac{T}{2A_p\rho}} - \frac{V_\infty}{2}. \tag{2.13}$$

Substituting equation 2.13 in equation 2.12, the required power can be calculated as a function of thrust and freestream velocity.

$$P = T\left(\frac{V_\infty}{2} + \sqrt{\frac{{V_\infty}^2}{4} + \frac{T}{2A_p\rho}}\right) \tag{2.14}$$

2.2 Computational Fluid Dynamics (CFD)

Computational fluid dynamics numerically analyze fluid flow, heat transfer and related phenomena, predicting its behaviour under specified conditions. It iteratively solves the Navier-Stokes equations with additional models to account for turbulence, multiphase flow, chemical reactions, and radiative heat transfer, providing information such as pressure loss and flow distribution [82] [83].

2.2.1 Frozen Rotor Model

The multiple reference frame model (MRF), also known as the frozen rotor model, assumes that a control volume rotates at a constant speed, considering non-wall boundaries as surfaces of revolution. This is a steady-state approximation, used for its accurate results and simplicity while requiring less computational time than the alternatives.
For the case of a propeller rotating in a control volume, a moving reference frame is assigned to the propeller, used to solve its surrounding flow. The outside flow is solved in a stationary frame, assuming steady-state flow conditions at the interfaces [84] [85] [86].

2.2.2 Mixing Plane Model

The mixing plane model, just like MRF, is a steady-state method that uses relative and absolute reference frames. In this case, the coupling between the two domains is done by exchanging circumferentially averaged flow quantities. This method is the simplest steady-state model, requiring 50x less computational effort than sliding mesh model, with the capacity of calculating flow properties for rotor and stator almost independently[86].
The low computational costs combined with its simplicity have led this model to be widely used in turbomachinery, rendering accurate predictions of flow conditions in axial flow machines [87] [88] .

2.2.3 Transient Rotor-Stator Model

Sliding mesh model (SM), also known as transient rotor-stator, is theoretically the most accurate approach, describing the transient start-up without requiring mesh deformation. It requires two domains, a cylindrical one that contains the propeller, rotating a prescribed angle per time step during the simulation, and a second one where the mesh doesn't move during calculations. The interface of the two domains uses an arbitrary mesh interface (AMI), that projects patches of one geometry into the other, ensuring the values are the same on both sides. This method is computationally costly, requiring 30x more computational time than the previous model [88] [89] [90] [91] [86] . Figure 2.4 presents an illustration of the domains used in CFD analysis when the MRF or SM models are applied .

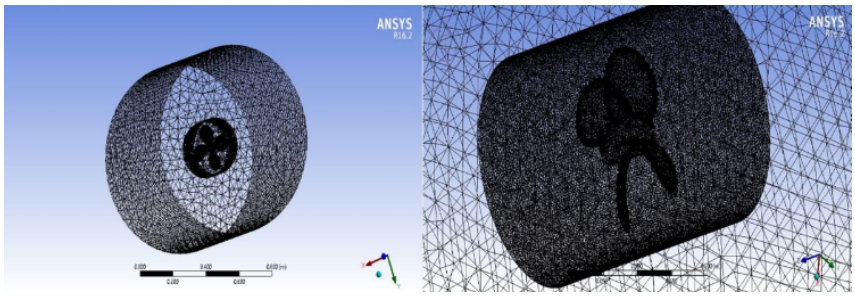

Figure 2.4: Typical domains for SM and MRF simulations [92]

2.2.4 Turbulence Model - Shear Stress Transport

Shear-stress transport (SST) is a two-equation eddy-viscosity model that uses k-ω formulation for the inner parts of the boundary layer, switching to a k-ϵ behaviour in the free stream. It solves both the equation for turbulent kinetic energy, k and the equation for turbulence frequency, ω, by taking advantage of k-ω's accurate predictions of adverse pressure gradient and separating flows while avoiding its sensitivity to inlet free-stream turbulence properties, that is best represented by the k-ϵ model. This Reynolds-averaged Navier-Stokes method accounts for the transport of the principal turbulent shear-stress, assuming the turbulent boundary layer shear stress is proportional to the turbulent kinetic energy [93] [94].

2.2.5 Finite Volume

Finite volume method, (FVM), is a numerical technique that transforms the partial differential equations, (PDE's) that represent the conservation laws over differential volumes into discrete algebraic equations over finite elements. It requires the discretization of the geometric domain into non-overlapping finite volume to then transform the PDE's into algebraic equations by integration over a discrete volume, solving them to obtain the values of the dependant variable for each of the volumes.
This is a strictly conservative approach that can be formulated with unstructured polygonal meshes as well as a variety of boundary conditions, since the variables are evaluated at the centroids of the volume elements [95] .

2.3 Flight Dynamic Modeling

The flight dynamic model for the developed prototypes was derived with a Newton-Euler formulation, assuming the structure is rigid with y-symmetry, the center of gravity coincides with the origin of the fixed body frame and both thrust and torque are proportional to the square of the propeller's angular velocity. Additionally, the propeller's gyroscopic effects were neglected, for simplicity [96].

Reference Frames

To derive the equations of motion, two reference frames are required: the Earth frame and the body frame. The first is a fixed, inertial frame, connected to Earth, with a NED (North-East-Down) orientation, while the latter is a moving reference frame, connected to the body, often called ABC (Aircraft body-centred). Figure 2.5 presents both reference frames [97].

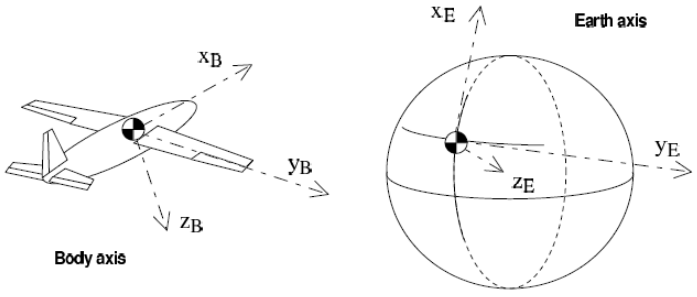

Figure 2.5: Earth and body frames [98]

The distance between the origins of the reference frames, represented by $r = [x \;\; y \;\; z]^T$, describes the absolute position of the prototype, while the orientation is given by Euler angles $\eta = [\phi \;\; \theta \;\; \psi]$, that represent roll, pitch and yaw, respectively. The rotation matrix R transforms the body frame's orientation into inertial frame coordinates, to relate vector quantities measured in both frames. The rotational velocity of the UAV can be represented by the body rates $\omega = [p \;\; q \;\; r]$ or by the inertial Euler rates $\dot{\eta} = [\dot{\phi} \;\; \dot{\theta} \;\; \dot{\psi}]$, that are related by equation 2.15.

$$\omega = R_r \dot{\eta} \tag{2.15}$$

The rotation matrices R and R_r are presented below.

$$R = \begin{bmatrix} c\theta c\psi & s\phi s\theta c\psi & c\phi s\theta c\psi + s\phi s\psi \\ c\theta & s\phi s\theta s\psi + c\theta s\psi & c\phi s\theta s\psi - s\theta c\psi \\ -s\theta & s\phi c\theta & c\phi c\theta \end{bmatrix} \tag{2.16}$$

$$R_r = \begin{bmatrix} 1 & 0 & -\sin\theta \\ 0 & \cos\phi & \sin\phi\cos\theta \\ 0 & -\sin\phi & \cos\phi\cos\theta \end{bmatrix} \tag{2.17}$$

To derive the dynamics equations, the relative position of the rotors in the body frame must be defined. The two typical configurations are (+) and (x) and have different purposes. In this case, the rotors aren't positioned in a way that allows a (+) configuration, therefore an (x) configuration was selected. Figure 2.6 presents illustrations of both possible types of configurations. A tri-rotor configuration will be designed and its reference frame presented with the equations to develop its flight dynamics model.

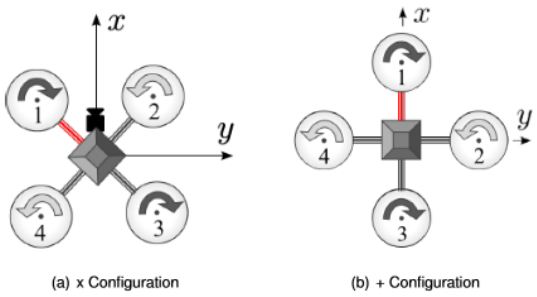

(a) x Configuration (b) + Configuration

Figure 2.6: Types of quadrotor reference frames [99]

2.3.1 Dynamics Model

The classical Newton-Euler approach can be used to derive the dynamics equations for the prototype, in the body frame. Equations 2.18 and 2.19 present the translational and rotational motions, respectively.

$$\frac{d}{dt}[mV]_B + \omega \times [mV]_B = F, \tag{2.18}$$

$$\frac{d}{dt}[I\omega]_B + \omega \times [I\omega]_B = M, \tag{2.19}$$

where *m* is the mass of the prototype in kg, *V* is the linear velocity vector in m/s, ω is the angular velocity in rad/s and *I* is the inertia tensor in kgm^2. The forces and moments generated by each rotor in the body frame are calculated with equations 2.20 and 2.21, where the quadratic relation to the angular speed is used. The torque and thrust constants -K_τ and K_T -, were experimentally determined [57] [100] [101].

$$F_i = K_T \omega_i^2 \tag{2.20}$$

$$M_i = K_\tau \omega_i^2 \tag{2.21}$$

The remaining forces to account for in the model are drag and gravity. These are included on equations 2.18 and 2.19 [102].

2.3.2 State Space Representation

The state space equation is a first order differential equation that represents the dynamics of any system, namely a UAV. Assuming a model with no disturbances or noise, the equation is given by,

$$\dot{x} = Ax + Bu, \tag{2.22}$$

where *A* is the dynamics matrix, *B*t is the input matrix, *x* is the state vector and *u* is the input vector. The state vector defines the linear and angular velocity of the UAV, as well as its position and orientation. It is represented by,

$$X = [u \;\; v \;\; w \;\; p \;\; q \;\; r \;\; x \;\; y \;\; z \;\; \phi \;\; \theta \;\; \psi]. \tag{2.23}$$

The input vector represents the rotation of each rotor in rad/s. For the case of a quadrotor it is given by

$$U = [\Omega_1 \;\; \Omega_2 \;\; \Omega_3 \;\; \Omega_4]. \tag{2.24}$$

The *B* matrix is a four line matrix with as many columns as there are actuators, rotors in this case. It's lines represent the upwards force and the three moments generated due to the rotors. On the other hand, the *A* matrix's purpose is mostly to account for the effects of drag and gravity [102][103][104].

2.3.3 Control

To verify the validity of the assumptions previously established, as well as to ascertain the accuracy of the mathematical model, a closed-loop controller was derived by use of PID controllers [105]. As suggested by figure 2.7, these controllers compute the desired output signal to the rotors by summing the proportional, integral and derivative responses.

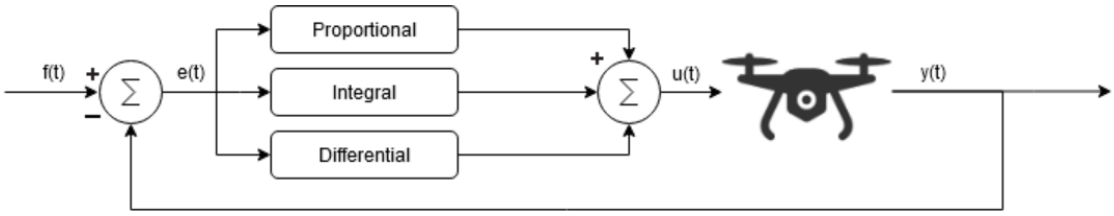

Figure 2.7: Schematic structure of a PID controller

The proportional component of the PID controller has the most impact, changing the output proportionally to the error. It depends on the proportional gain constant K_P; the system could become unstable if set too high, or insensitive to control if set too low.

The integral side of the PID is responsible for the speed of the response, controlled by the integral constant, K_I. In this case, the system's response becomes faster with a higher value of K_I, though it may begin to oscillate past a certain threshold; should the value be too low, the influence on the system would be negligible, making the integral component of the system inadequate. Additionally, it eliminates the static error.

Lastly, the derivative control mode is responsible for the rate of change of the error, which renders it ineffective with constant errors. Its performance is tied to the derivative constant K_D, which may also produce oscillations if set too high. The combination of these three components results in a faster control action while reducing the effects of disturbances [106] [106].

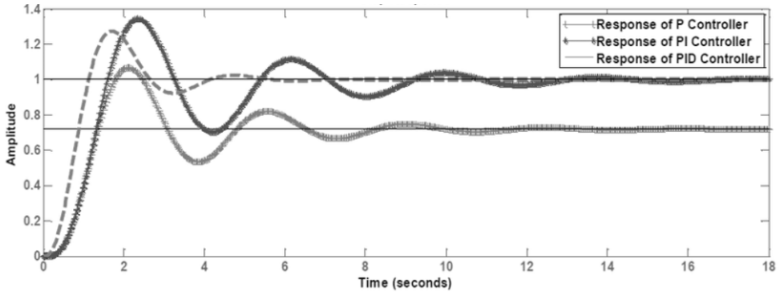

Figure 2.8: Response comparison for different controllers [107]

Figure 2.8 presents a comparison of step responses with a proportional P controller, a proportional-integral controller PI and a PID controller. The PID has a faster response time with less oscillation than the other options.

Chapter 3

Propulsion System Sizing

This chapter describes the steps taken to size the propulsion system for the selected configurations, including the methodology for the motor selection and the process of estimating the total mass of the system. It also describes the chosen configurations, comparing their performance in cruise, dash and hover. Finally, it quantifies wing-rotor interference.

3.1 VTOL Parametric Studies

The initial phase of the project development was characterised by the study of the different propulsion options available. With a defined maximum take-off mass (MTOM) of 7kg, electrical propulsion was already pre-determined, leaving rotor position, number of rotors, and available T/W ratio to be stipulated. To help the decision-making process, parametric studies were performed.

3.1.1 Power estimations

Given the interest in asymmetric VTOL thrust distributions, studying power demands for a quadrotor became necessary, considering different RPM and propeller sizes. Aside from the regular symmetric quadcopter, estimates were done considering 60%-40% to 90%-10% thrust distributions between the front and rear rotors, favouring the latter. To perform these studies, the rotor position as a function of its thrust output had to be computed. Equation 3.1 presents this relation .

$$\begin{cases} 2(T_r x_r + T_f x_f) = 0 \\ 2(T_r + T_f) - W - D = 0, \end{cases} \tag{3.1}$$

where T_r and T_f are the thrust produced by the rear and front motors, respectively, and x_r and x_f are the distances of the rotors to the centre of gravity. The drag force D had been stipulated as 5% of the UAV's weight for take-off and climb, defining a required T/W ratio of 1.05. For each of the five possible thrust distributions, the required power per rotor P_i was calculated with equation 3.2, based on propeller momentum theory.

$$P_i = T_i V_c - \frac{k_i}{2} T_i V_c + \frac{k_i T_i}{2} \sqrt{{V_c}^2 + \frac{2T_i}{\rho A_i}} + \frac{\sigma C_{d0}}{8} \rho A_i {V_{tip}}^3 \tag{3.2}$$

Where T_i and A_i are the thrust and area of each rotor, V_c is the axial climb speed and V_{tip} is the blade's tip velocity. The remaining parameters were defined according to typical values.

- The rotor blade solidity $\sigma \in$ [0.07, 0.12], using 0.1 in all calculations [108];
- The blade drag coefficient C_{d0} can take the typical value of 0.01 [108];
- The induced power correction factor k_i, has a value of 1.15 for axial flight [109];

The blade tip speed followed from equation 3.3, where R_p is the radius of the ith propeller and ω_p is the propeller rotation speed.

$$V_{tip} = \Omega_p R_p \tag{3.3}$$

Rotor Positioning

For a given T/W ratio and axial climb speed, the required power for take-off will depend on the position of the rotors, radius and the rotational speed of the propeller. Table 3.1 seen bellow, presents the thrust requirements for each possible configuration with a T/W ratio of 1.05.

Rotor Positioning	50-50	60-40	70-30	80-20	90-10
T_f [N]	18.03	14.42	10.82	7.21	3.61
T_r [N]	18.03	21.63	25.24	28.84	32.45

Table 3.1: Required thrust per configuration

To estimate the minimum required power per case, the derivative of the required power with radius is calculated, obtaining the radius that minimizes power consumption for a given propeller rotation. Table 3.2 shows the results for minimized power for a total area of $\sum A_i = 0.4\ m^2$ at a climb speed V_c of 2 m/s, where the reference power is the required for a symmetric configuration.

Rotor Positioning	50-50	60-40	70-30	80-20	90-10
Power front [W]	245.61	192.86	136.89	88.32	37.38
Power rear [W]	245.61	298.47	359.85	408.49	455.93
Radius front [m]	0.1777	0.1646	0.1553	0.1444	0.1232
Radius rear [m]	0.1777	0.1906	0.1974	0.2077	0.2191
Total power [W]	982.46	981.86	993.47	997.61	986.63
Total power [%]	100%	99.94%	101.12%	101.54 %	100.42%

Table 3.2: Required power and area distribution per configuration

For a given total disc area and thrust-to-weight ratio, the power doesn't shift significantly with the position of the rotors, which made a 90-10 configuration most appealing considering that the main objective is to have an asymmetric thrust distribution, favoured towards the rear rotors. However, placing 90% of

the trust at the back would result in having less margin to locate the rear rotors, shifting the front ones beyond the UAV's nose with the potential of lacking authority for manoeuvres. For that reason, an 80-20 configuration was chosen as the best compromise.

Maximum Thrust-to-Weight Ratio

The maximum trust-to-weight ratio impacts power consumption of the VTOL system, linearly increasing it as shown in figure 3.1(a). The data estimated for comparison assumes a 2m/s axial climb speed, with a total disc area of 0.4m^2 for an 80-20 configuration.
The increase of power demands with T/W ratio is significant enough to choose the minimum ratio that fulfils the manoeuvrability requirements defined by the control team at $T/W = 1.3$.

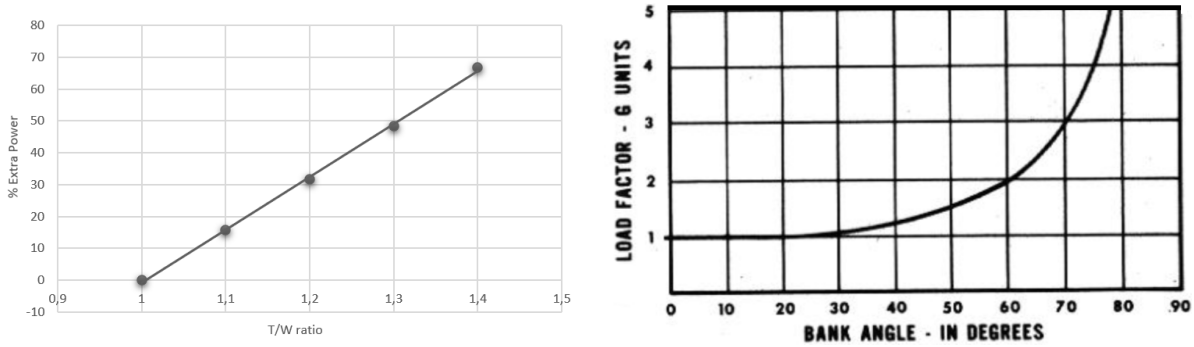

(a) Power variation with T/W ratio

(b) Load factor chart

Figure 3.1: Effects of T/W ratio [110]

Typical UAV T/W ratios are usually higher, depending on the application - from 1.67 for aerial photography to 2.22 for first-person view race copters [76]. However, a T/W ratio of 1.3 is already enough to sustain flight with a bank angle of 40° , as shown in figure 3.1(b), which was deemed sufficient for the mission.

3.2 Configuration Definition

To study the effects of an asymmetric propulsion system, four configurations were defined and compared. The first configuration, a symmetrical quadrotor with a lift-and-cruise propulsion system was established as the base for all comparisons. The second configuration is the first attempt at an asymmetric thrust VTOL system, having a ratio of distance to the c.g. of 4/1, that distributes 20% of the thrust to the front rotors and the remaining to the rear ones. Similarly to the first configuration, configuration two is also a lift-and-cruise quadrotor. The third configuration has the same VTOL rotor positioning as the second, changing the lift-and-cruise into vectored-thrust, tilting the rear rotors for forward-flight. The last configuration is the end goal of the project, where configuration three is transformed into a tri-rotor, while maintaining a vectored-thrust setup and the thrust ratio between front and rear rotors. Figures 3.2 through 3.5 present representations of VTOL rotor positioning for the configurations mentioned, where configurations three and four feature retractable booms for forward-flight, being stored in the fuselage.

The direction of the tilt of configurations three and four has yet to be defined and will depend on the chosen mechanism. In configurations two through four, the rotors are expected to be covered by the wing and/or canard, which will impact their thrust output. This topic will be discussed further later in this chapter.

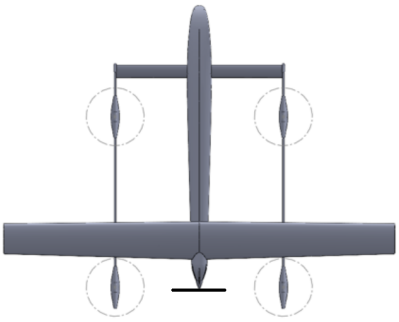

Figure 3.2: Configuration 1

Figure 3.3: Configuration 2

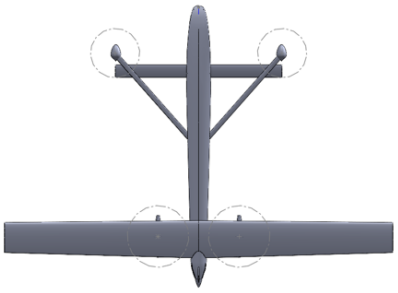

Figure 3.4: Configuration 3

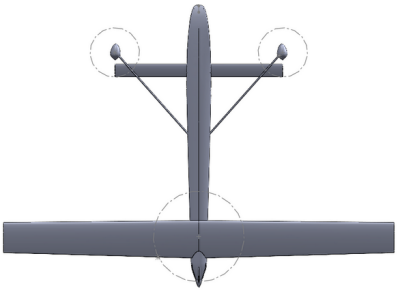

Figure 3.5: Configuration 4

3.3 Propulsion System Selection

The selection of the propulsion system was divided into two categories: VTOL and forward-flight. For the VTOL subsystem, the demands were based on static thrust, as the axial speed is low, thus making the approximation valid, while for forward-flight, the estimations were based on power consumption. The propulsion requirements are presented on table 3.3.

Requirement	Description
Minimum T/W_{max}	1.3
T/W_{Climb}	1.05
$T/W_{Descent}$	0.95
Cruise speed	20 m/s
Dash speed	35 m/s
D_{pusher} propeller	15 in
D_{max} propeller	15 in (quadrotors)
Single battery	6S - 22.2V (quadrotors)

Table 3.3: Propulsion requirements

Additionally, the propulsion system must be able to perform the defined mission, requiring a battery capable of providing 60 seconds of power for take-off, 30 seconds of power for landing, 10 seconds of power at maximum throttle, 20 minutes of cruise time and a 20% backup.

Selection Criteria

The selection was made based on the least system mass, including components and battery mass. On the components side, the full set of propeller, motor and ESC was considered, while the battery mass was estimated from the power consumption during the mission. Figure 3.6 presents a flow chart of the selection process for the defined criteria.

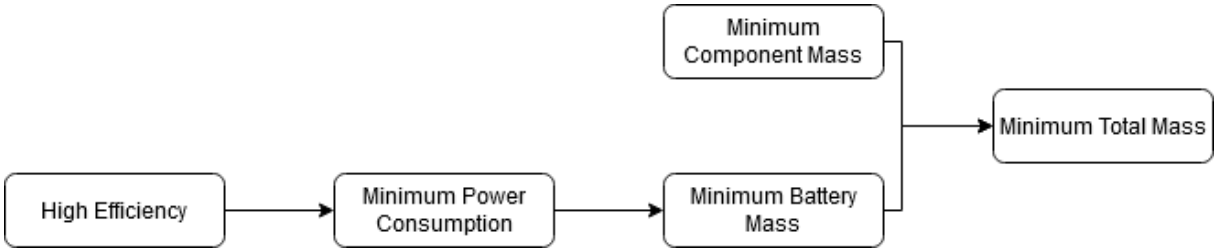

Figure 3.6: Flow chart of motor selection process

3.3.1 VTOL System Selection and Validation

The selection of the motor-propeller combination for the VTOL system was done via a survey of the available options in the market while respecting the project requirements.

The three major brands considered were KDE motors, T-Motors and AXI motors, all of which have high-efficiency products with a long life-span. For VTOL, brands with experimental static thrust data for motor-propeller combinations were privileged, as it added an extra security factor to the previous estimations while providing data for comparison with the performed static thrust tests. For that reason, T-motors was chosen as the go-to brand for all VTOL motors.

Table 3.4 presents the required maximum thrust values - correspondent to a T/W ratio of 1.3 - that were used for the selection process of the motor-propeller combinations from T-motors.

Thrust	Configuration 1	Configuration 2	Configuration 3	Configuration 4
Front Rotor [N]	22.31	8.93	8.93	8.93
Rear Rotor [N]	22.31	35.71	35.71	71.42

Table 3.4: Required thrust per configuration

Selected Components

The components for each configuration are listed on table 3.5, where the ESCs were chosen based on voltage and current compatibility with the motor, taking into consideration the manufacturers advice.

All the chosen motors for configurations one through three are from the Navigator series, with a speed constant - KV - from 420 to 480 RPM/V. The rear rotor of configuration four required a more powerful motor, from the P series, with a speed constant of 170 RPM/V.

Component	Configuration 1	Configuration 2	Configuration 3	Configuration 4
Front rotor motor	MN4012 KV480	MN3110 KV470	MN3110 KV470	MN3110 KV470
Front rotor propeller	14x4.8	11x3.7	11x3.7	11x3.7
Front rotor ESC	Air 40	Air 20	Air 20	Air 20
Rear rotor motor	MN4012 KV480	MN5212 KV420	MN5212 KV420	P60 KV170
Rear rotor propeller	14x4.8	15x5	15x5	22x6.6
Rear rotor ESC	Air 40	Flame 70	Flame 70	Flame 60

Table 3.5: Component list

Component Validation

Prior to purchasing the components, the experimental data available from the T-motors website was compared against data derived from vortex theory. To do so, a MATLAB® script was developed, based on the mentioned theory, where the thrust output of a specific motor-propeller combination was compared to the experimental data for the same power and RPM.

In order to increase the fidelity of the model, the propeller's characteristics were also entered into the script, accounting for number of blades, pitch, diameter, chord distribution along the radius and hub size. Since chord distribution and hub size were not provided, these were extrapolated from known propellers. The results are presented on table 3.6, where the values correspond to maximum throttle.

Propeller D[in]xP[in]	Power [W]	Rotation [RPM]	Thrust Experimental [N]	Thrust Theoretical [N]	Thrust Difference [%]
11x3.7	164.28	8200	10.89	12.31	13.23
14x4.8	472.86	8000	25.50	29.02	13.8
15x5	881.3	9091	40.95	46.53	13.6
22x6.6	1632	6374	82.54	93.7	13.52

Table 3.6: Thrust validation

The discrepancy between the experimental and theoretical values is between 13% and 14%, resulting from approximations made for unknown parameters of the propeller geometry, as well as from assumptions from the vortex theory's model itself. Despite the difference in results, the choice was validated for purchasing.

Due to shortage in supply, the propellers for the front rotors of configuration 2 through 4 were no longer available. To solve this problem, a propeller of the same model with higher diameter and pitch (12x4), ensuring the required thrust.

Since configurations three and four feature a vectored-thrust propulsion system, their components must

also be validated for forward-flight. This verification will take place in the next section, where the forward-flight performance is assessed.

3.3.2 Forward-Flight Selection and Validation

The method for the motor-propeller selection for forward-flight is similar to the VTOL process, basing the choice on required power rather than static thrust. To compute the required power Corke's propeller design method was used, as shown by equation 3.4.

$$P = \frac{TV}{\eta_p} = \frac{WV}{\frac{L}{D}\eta_p}, \tag{3.4}$$

where P is power in W, T is thrust in N, W is weight in N, V is the forward velocity in m/s, $\frac{L}{D}$ is the UAV's lift-to-drag ratio and η_p is the propeller's efficiency - typically 70% to 80% in cruise for commercial aircraft. The efficiency of propellers also depends on the number of blades, the operational Reynolds number, the scale and even the relationship between the diameter and the advance ratio. Table 3.7 presents the data used to compute the required power for cruise and dash, where the values of $\frac{L}{D}$ were obtained with Ansys® CFX simulations.

L/D	Configuration 1	Configuration 2	Configuration 3	Configuration 4
Cruise	16.44	13.91	18.55	19.34
Dash	6.74	5.67	8.05	8.73

Table 3.7: L/D for the different configurations

Pusher Selection

The selection of components for forward-flight was only necessary for configurations one and two, as the remaining feature a vectored-thrust propulsion system, tilting the rear VTOL rotors. Unfortunately, at this point, only configuration one had been fully designed and simulated, leaving the $\frac{L}{D}$ of configuration two as unknown at that moment. For this reason, the selection was aimed at satisfying configuration one's requirements, computing the penalties of the usage of the same components in configuration two later on.

Since power consumption is mostly determined by the propeller, the selection of this component took priority. Out of the known brands, APC was defined as the source for the propellers, as they offer experimental curves with performance data for their products, making it easier to estimate their behaviour.

To select the propeller, a MATLAB® script was developed, following the assumptions made on equation 3.4, where $T = D$ and $\frac{L}{D} = \frac{W}{T}$. The program's algorithm is described below.

1. Generate thrust vs RPM curves for cruise and dash velocity;
2. Calculate RPM at which cruise and dash thrust is achieved;
3. Generate power vs RPM curves for this flight condition;

4. Substitute RPM from item 2 to calculate absorbed power by the propeller;

5. Use equation 3.4 to compute efficiency;

The selection was performed based on the highest efficiency , as propeller mass variation was not significant. Table 3.8[1] shows the estimated performance of the chosen propeller - APC 15x13N - for configurations one and two.

	Flight Condition	Efficiency [%]	Power[2] [W]	RPM
Configuration 1	Cruise	80.68	103.37	3434.6
	Dash	96.27	370.42	5827.3
Configuration 2	Cruise	83.31	118.12	3621
	Dash	96.39	439.74	6070.3

Table 3.8: Estimated propeller performance

The motor choice criteria were based on the propeller power demands while ensuring that it was able to output the required RPM. However, a survey of the available products showed that motors that function within the range of power mentioned above are not compatible with the required 6S - 22.2V - batteries, which limited the choice to oversized motors that consume up to 1kW at maximum throttle.
Within the surveyed motors, three stood out as possible candidates, presenting reasonable characteristics and respecting all propulsion requirements. Once again, brands that showcased experimental data were favoured, reducing the choice to KDE's 4012 KV400 RPM/V.
To complete the propulsion system, an ESC was chosen from KDE to couple with the motor. The choice was KDE-UAS55HVC, as it can handle the voltage and current of the motor while featuring a protective case that decreases vibration noise.

Component Validation

Before purchasing, a second performance estimation was conducted using the vortex theory model previously mentioned. This model was used both to validate the choice for configuration one, as well as to ensure forward flight performance of the remaining configurations. Table 3.9 displays the values for power and efficiency for each configuration, confirming that the selected propulsion system is capable of reaching cruise and dash conditions.

The power estimated for cruise condition with the vortex theory model is 8% and 3.5% lower for configurations one and two, respectively, than the one estimated from propeller curves. Regarding dash, the difference between the experimental curves and the model is 7.32% and 8.65%. This discrepancy can be due to the errors induced by interpolating the experimental data, approximating propeller properties and assumptions made with the vortex theory model. In any case, the similarity of the results was close enough to validate the choice for purchasing[3].

[1] The data presented bellow was obtained from the manufacturer's website. The efficiency values are unusually high for a propeller of this type, which will be validated with fixed-wing flight tests in the future.

[3] The data gathered on the table 3.9 already accounts for the correct $\frac{L}{D}$, computed with Ansys® CFX

	Configuration 1	Configuration 2	Configuration 3	Configuration 4
Cruise Power [W]	95	114.16	92.02	92.64
Cruise Efficiency [%]	87.79	86.54	80.42	76.64
Dash Power [W]	400.44	481.39	387.32	390.79
Dash Efficiency [%]	89.05	88.06	77.17	70.45

Table 3.9: Power and efficiency of the different configurations

3.3.3 Power Distribution and Consumption

With the selected components it is possible to evaluate the installed power of each configuration, estimating the ratio available for forward-flight, as well as front-to-back power distribution. Table 3.10 shows these estimates for the different configurations.

Starting with the total installed power, configurations one and three present similar values, despite the difference in the number of motors. Although all four configurations are able to perform the mission, configuration four has the least excess power installed, as it only features three motors, while configuration two has the most excess power.

When it comes to forward-flight, the vectored-thrust configurations have more available power, since the tilting rear rotors are responsible for this flight condition. Configurations one and two feature less available power, as the pusher was sized specifically for forward-flight.

The ratio of front-to-back power for configurations one through three mirrors the thrust ratio between the rotors. Configuration four's slight discrepancy is due to having only one rear rotor, reducing the extra power available from motor oversizing.

	Configuration 1	Configuration 2	Configuration 3	Configuration 4
Total installed power [W]	3285.6	4040.4	3330	2490
Power forward-flight [%]	21	18	80	73
Power front rotors [W]	1287.6	666	666	666
Power front rotors [%]	50	20	20	27
Power rear rotors [W]	1287.6	2664	2664	1824
Power rear rotors [%]	50	80	80	73

Table 3.10: Available power per configuration

Besides studying the power distributions, it is relevant to estimate power consumption per configuration, assessing which are most efficiently sized. To do so, an estimation of the required power for cruise and hover was conducted. Table 3.11 presents these power estimations, where the data for hover was derived from the manufacturer's data - except for the power for front rotors of configurations two through four - and the power for cruise which were estimated with vortex theory. All relative data is presented as a function of the base configuration, configuration one.

In hover, configurations one through three show similar results, with a difference under 3% between them, while configuration four has the least power demands, consuming over 8% less.

Power	Configuration 1	Configuration 2	Configuration 3	Configuration 4
Hover [W]	1089.28	1119.6	1119.6	997.52
Hover [%]	100	102.8	102.8	91.6
Cruise [W]	95	114.16	92.02	92.64
Cruise [%]	100	120.3	96.9	97.5
Dash Power [W]	400.44	481.39	387.32	390.79
Dash Power [%]	100	120.3	96.8	97.7

Table 3.11: Power consumption per flight condition

In cruise, configuration two has a penalty of 20% increase in power consumption, when compared to configuration one, whereas configurations three and four reveal benefits under 5%, neutralising the lower efficiency of the propellers.
Similarly to cruise condition, configuration two requires the highest amount of power in dash, since it has the lowest value of $\frac{L}{D}$. Configurations three and four present lower values for required power, despite exhibiting lower propeller efficiency. Overall the relative power consumptions don't shift significantly from cruise to dash.

3.4 Propulsion System Mass Estimation

The mass of the propulsion system can be divided into two major contributors: the propulsive components and the battery. The components include the ESC-motor-propeller combinations, neglecting structural mass for motor mounts and supporting booms, as well as tilt-mechanisms and cabling, while the battery mass comprises the estimated required battery to fulfil the desired mission once. The battery mass estimation process is described in figure 3.7, following the criteria mentioned below.

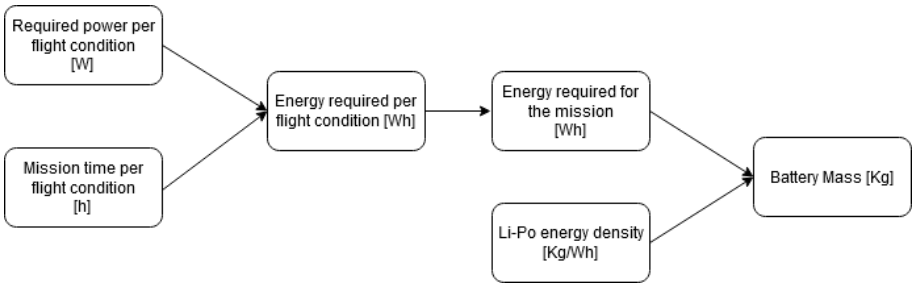

Figure 3.7: Battery mass estimation

1. The power required is the sum of the demands of the motors functioning at that mission segment;
2. The total energy required includes 20% backup;
3. The energy density used is 170.33 Wh/kg;

The energy density was estimated from the chosen battery itself. Knowing the capacity and the nominal voltage, the energy in Wh was calculated and divided by the weight of the battery to give an estimation

of the impact of the energy efficiency in the overall weight of the propulsion system and range of the mission.

The estimations of power for the VTOL motors were done by interpolating the manufacturer's experimental data for the motor-propeller combinations. This was not possible for the front rotors of configurations two through four, where this data was not available; for these configurations, as well as for all forward-flight power estimations the vortex theory model was used. Table 3.12 presents energy requirements, the total component mass, as well as the battery mass estimation for the mission.

	Configuration 1	Configuration 2	Configuration 3	Configuration 4
Energy [Wh]	77.91	81.27	72.42	75.29
Battery mass [kg]	0.46	0.48	0.43	0.44
Component mass [kg]	1.115	1.238	0.924	0.7595
Total mass [kg]	1.57	1.72	1.35	1.20
Mass difference [%]	0	9.08	-14.20	-23.59

Table 3.12: Total energy consumption and propulsion system's mass

As expected, configurations three and four have a lighter propulsion system, given that they feature fewer components. When it comes to energy demands, configuration three has the least required energy, due to a more efficient cruise condition - the longest mission segment. For this particular mission, both vectored-thrust configurations perform better than their lift-and-cruise competitors, having a lighter and more energy-efficient propulsion system.

Table 3.13 shows the percentage of battery consumption per mission segment to assess the influence of the VTOL flight conditions in the overall battery mass.

	Configuration 1	Configuration 2	Configuration 3	Configuration 4
Cruise [%]	48.77	56.19	50.82	49.22
VTOL [%]	51.23	43.81	49.17	50.78
Take-off [%]	30.02	23.83	26,74	28.78
Landing [%]	13.11	10.50	11.79	12.34
Max Throttle [%]	8.09	9.49	10.65	9.66

Table 3.13: Propulsion system's energy breakdown per mission segment

All configurations feature around 50% of their battery mass for the VTOL system and the remaining for cruise condition. When comparing the 100 seconds of VTOL system to the 1200 seconds of cruise, 50% of the battery for VTOL type seems excessive. A possible solution would be to revise project requirements and decrease the time allocated for VTOL.

Assuming all the prototypes have the same propulsive system mass of configuration one, the mass difference presented on table 3.12 can be translated into battery mass: lighter, more efficient configurations may have more battery mass whereas heavier, less efficient ones might have less battery mass. This difference is to be noted in cruise condition, where it can increase or decrease the range of the

configuration, while still accounting for the required energy to perform the VTOL mission segments. Table 3.14 presents the variation in range due to battery mass variation.
To compute these values, the mass difference was converted into energy and added to the energy assigned for cruise. With the energy and power consumption the endurance was calculated and multiplied by cruise velocity to obtain the new mission range.

	Configuration 1	Configuration 2	Configuration 3	Configuration 4
Range difference [km]	0	-20.79	23.22	46.00
Total Range [km]	24	3.21	47.22	70.00

Table 3.14: Range variation

The range of the mission suffers significant changes with the mass fluctuations between configurations, increasing to over double the initial range for configuration three and to almost triple the range for configuration four, while decreasing it to less than a sixth of the range for configuration two. This is due to having only 50% of the battery allocated for cruise, making a mass difference of 140g sufficient to reduce over 20Km in range for configuration two as well as increasing the range in 46 Km with 370g, for configuration four.
If the penalties in excessive mass of configuration two were to be distributed proportionally throughout the mission segments - with the percentages calculated on table 3.13- the decrease in mission range wouldn't be as significant. On the other hand, applying this battery distribution to the other configurations would result on a decrease of the total range - relative to the on presented on table 3.14 -, increasing the power available for the other mission segments. Table 3.15 presents the variation of time available for the different mission segments as well as the predicted variation of endurance and range with a proportional battery distribution.

Variation	Configuration 2	Configuration 3	Configuration 4
Take-off time [s]	-21.54	37.81	60.42
Landing time [s]	-10.77	18.9	30.21
Max throttle time [s]	-3.59	6.30	10.07
Endurance [s]	-430.8	756.12	1208.35
Range [Km]	-4.62	15.12	24.17

Table 3.15: Range variation with proportional battery distribution

With this battery distribution, the penalties in range are not as severe for configuration two, while maintaining the ability to perform take-off at the desired vertical climb velocity, making landing the mission segment the most problematic. As for the two other configurations, there is a significant increase in time - or power - allocated for each mission segment, with an increase of over 60% relative to the initial range for configuration three, reaching double the range for configuration four.

3.5 Rotor Coverage

As previously mentioned, some of the configurations feature designs that have partially covered rotors by the wing and/or the canard, which will affect the thrust output of the rotors. Leishman [108] has established through empirical data that the thrust decrease due to coverage is dependent on the relative covered area and the relative distance between the rotor and the covering surface, as shown in figure 3.8.

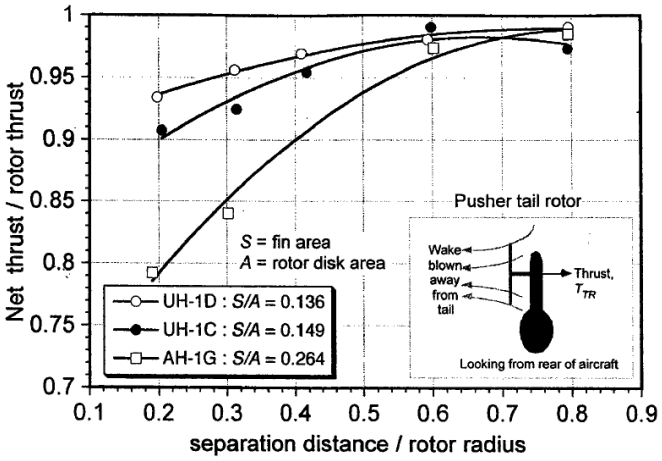

Figure 3.8: Rotor-tail interference for helicopters [108]

An estimation of this kind was deemed necessary for all configurations with partially covered rotors, assessing the net thrust available with the coverage defined in the design. To do so, the percentage of covered rotor area was calculated for each configuration.
Table 3.16 presents this data for the front and rear rotors of all configurations for VTOL.

Covered Area	Configuration 1	Configuration 2	Configuration 3	Configuration 4
Front Rotors [%]	0	10	10	10
Rear Rotors [%]	0	69	69	63

Table 3.16: Covered rotor area

To estimate the vertical distance from the wing at which the rotors much be placed, CFD studies were performed for different distances and covered areas. This study was performed with Ansys® CFX, based on an SST turbulence model and a sliding mesh algorithm - transient rotor-stator, where two domains were used:

- Rotational domain moving at 5000 RPM, containing a propeller with a 23” diameter,
- Static domain, containing the surrounding fluid.

An illustration of both domains may be seen on figure 3.9, where the dimensions are relative to the propeller size.[4] The width of the wing changed with the covered area, while the span was kept constant and equal to the length of the static domain - 5x propeller diameter.

[4] Figure 3.9 is not scaled, to save page space.

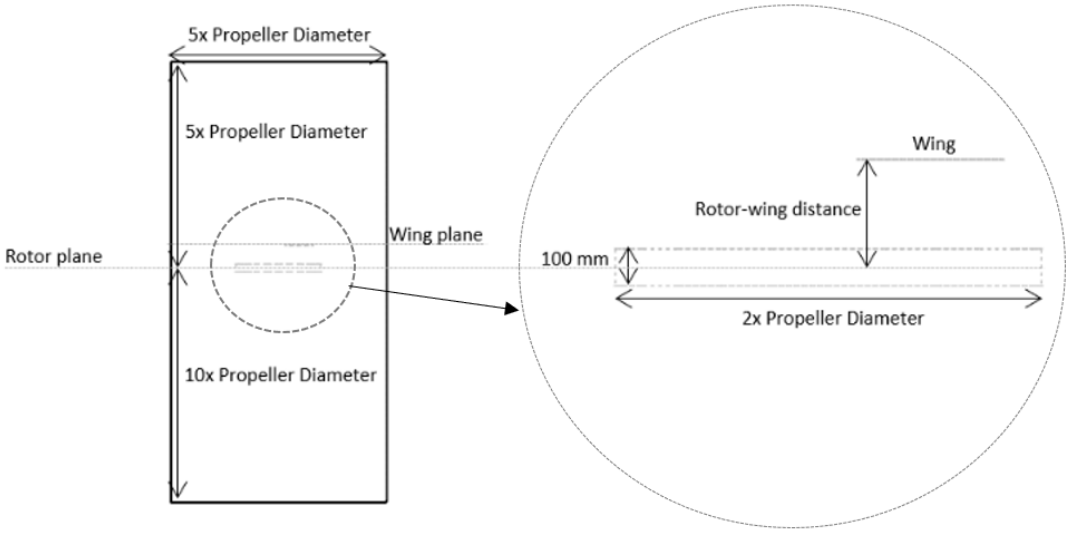

Figure 3.9: CFD domain representation

As for boundary conditions, the top face of the static domain was considered an inlet with 0 m/s airspeed, and the remaining were defined as openings with zero relative pressure. The wing and propeller were categorized with a no-slip wall boundary and the interfaces of the domains with transient rotor-stator (sliding mesh) mixing frame featuring no pitch change.

To ensure an acceptable degree of accuracy, multiple simulations were conducted for each case, increasing the number of elements of the mesh in both domains until the relative net force difference was under 1%. Table 3.10 presents the data obtained for an uncovered rotor, while figure 3.10 shows a graphical representation of its convergence. For the uncovered rotor, the thrust output was analysed, while net force - rotor + wing - was studied for covered rotors.

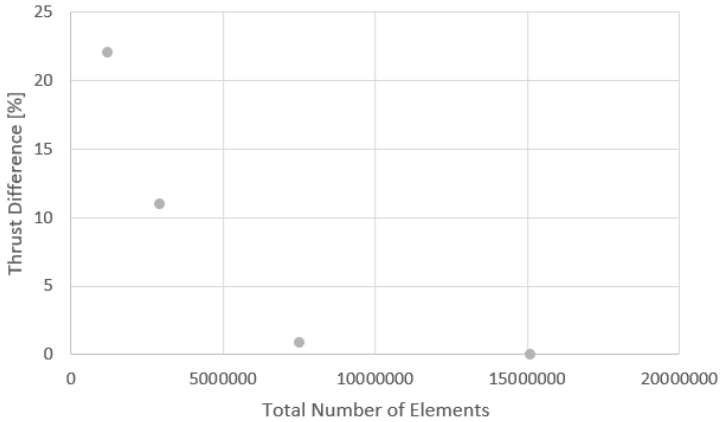

Number of Elements	Thrust [N]	Thrust Difference [%]
1203323	59.34	22.14
2922756	67.80	11.04
7487035	75.54	0.88
15088276	76.21	0.00

Table 3.17: Convergence data

Figure 3.10: Convergence for uncovered rotor

In the interest of estimating the variation of net force with distance and covered area, two types of simulations were performed. One where the covered area is kept constant, changing the distance between the rotor and the wing and another where the distance is kept constant and covered area is incremented. The results are presented on figure 3.11, where the net force is relative to an uncovered rotor and the

distance is relative to propeller radius.

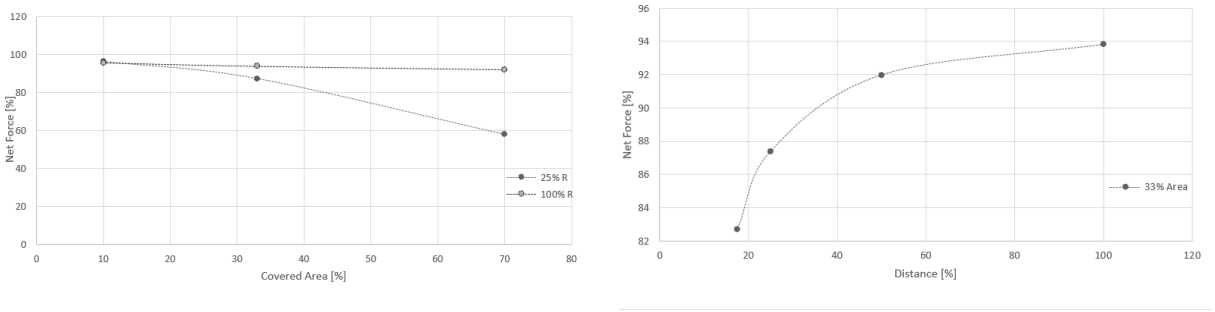

(a) Net force variation with covered area

(b) Net force variation with distance

Figure 3.11: Rotor coverage studies

Figure 3.11(a) shows a slight decrease in net force for 100% distance, decreasing below 4% for 10% to 70% area coverage. The 25% distance curve displays a much more significant net force decrease, losing up to 40% vertical force in the same area variation. Figure 3.11(b) presents the net force increase with distance, where there is a 10% variation on vertical force from 17.5% to 100% distance.

Assuming similar variations for different geometry propellers, the thrust losses for covered rotors in configurations two though four can be calculated, estimating the distance at which the rotors must be placed to fulfil project requirements - 1.3 T/W ratio. Since there was no available information for thrust output of the front rotors' motor+propeller combination, this study was only applied to the rear rotors, which were significantly covered.

Table 3.18 presents the required distance at which the rotors should be placed, as a function of their radius, in meters, to output a T/W ratio of 1.3. The data was obtained for the different covered areas through linear interpolation.

Rear Rotors	Configurations 2 & 3	Configuration 4
Available Thrust [N]	40.96	79.60
Required Thrust [%]	87.18	89.72
Required distance [%]	88.75	92.82
Required distance [m]	0.169	0.259

Table 3.18: Computational required rotor-wing distance

This data will be validated with experimental static tests to obtain the minimum required distance at which the rotors must be placed from the wing.

Chapter 4

Static Experimental Tests

This chapter contains the performance validation of the selected components, describing the test bench set up, software and requirements. It compares the experimental values with the ones obtained with theoretical models for uncovered and partially covered rotors and calculates the required constants for the tested motors.

4.1 Test Bench Set Up and Experimental Procedure

The static tests on the ESC-motor-propeller combinations were performed on a static test bench comprised of a motor mount, a power box, a data acquisition system, a power source and a safety button. Figure 4.1 presents the mentioned components.

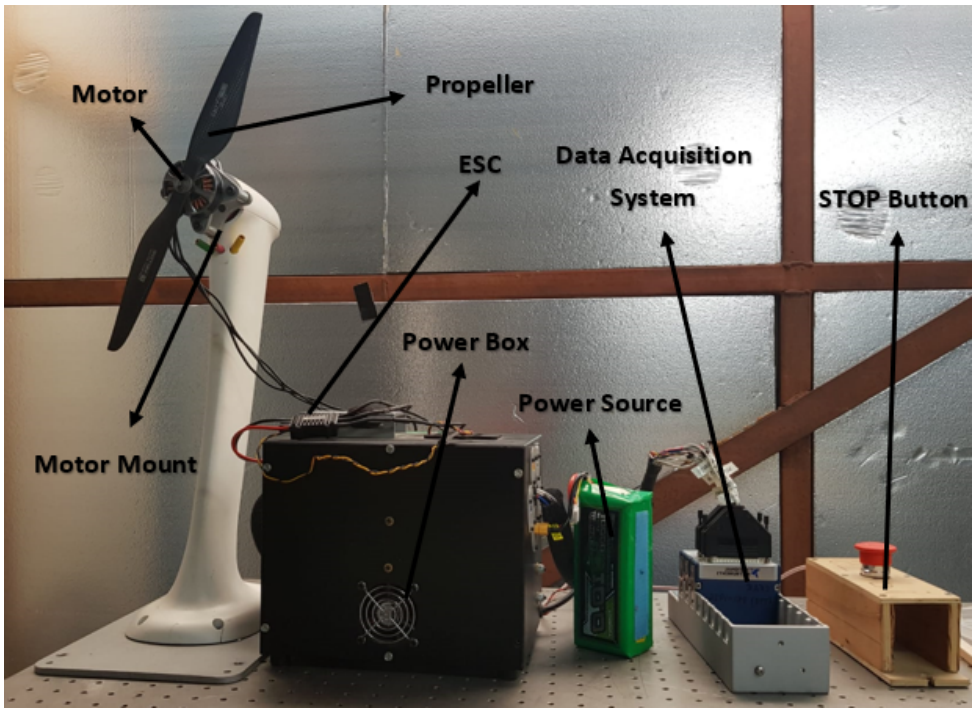

Figure 4.1: Test rig representation

The motor mount secures the motor to the table and features a load and torque cell that register net force and torque, respectively. Afterwards, there is the power box, that manages electric signals, sending the LabVIEW commands to the ESC and powering the motor with the connected power source. The power box is also connected to the data acquisition system, recording force, torque, current and voltage for a given throttle. Finally, the last component is the kill switch ”stop button”, that shuts down the motor. All the elements of the setup were developed in house, except the data acquisition hardware, that was purchased from National Instruments and the power source. The components of the test bench setup were assembled following the procedure described below.

- Screw the motor mount to the optic table;
- Mount the motor and propeller;
- Connect the power box the motor mount, plugging it in;
- Connect the ESC to the power box and motor;
- Connect the power supply to the power box;
- Connect the data acquisition system to the power box;

To control the setup hardware, a previously developed LabVIEW GUI was used. It's display is presented on figure 4.2.

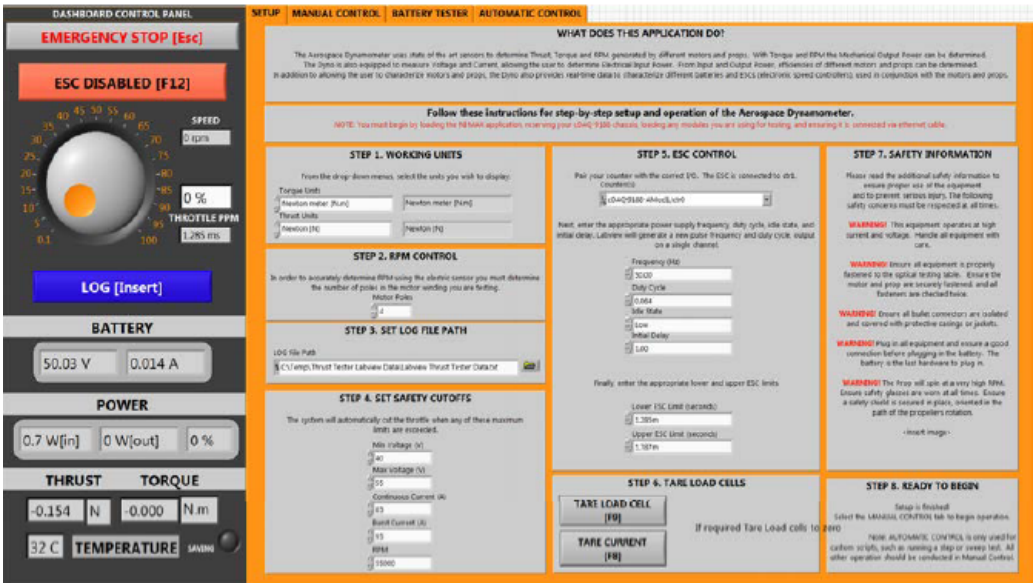

Figure 4.2: Software representation

On the right, the battery voltage and current are displayed as well as the power consumption and the measured thrust and torque. The throttle percentage and the ESC signal are also presented in this area. Of the remaining fields, the safety cutoff and ESC control were filled, ensuring motor operation.
Once all the components were assembled, the first step taken was calibrating the ESC to arm with a specific motor. The first approach is a gross estimation of the ESC's limits by connecting it to a servo and recording the values at which the motor starts working and at which its thrust stops increasing.

These limits were imput into the LabVIEW software to perform a finer tuning, where the upper limit was defined over the maximum thrust registered, to ensure peak thrust was reached. Once these limits were established, they were kept constant during testing. With the ESC properly calibrated, the experimental tests took place, with a minimum of three runs per case, going from 0% to 100% throttle in steps of 5%.

4.2 Experimental Results

The results were processed with a MATLAB® script, averaging the data of the different logs and taring thrust and torque values with the ones obtained for 0% throttle. Relations for thrust with throttle and power were derived, comparing the experimental values with the computational ones derived from vortex theory. Additionally, relations between RPM and thrust were derived to calculate thrust and torque and constants.

4.2.1 Thrust vs Throttle

As mentioned before, to ensure maximum thrust is achieved, the ESC's were calibrated beyond the estimated upper limit. These results were then re-scaled to reach peak thrust at maximum throttle - 100%. The thrust-throttle curves for all the purchased motor-propeller configurations are presented on figure 4.3[1].

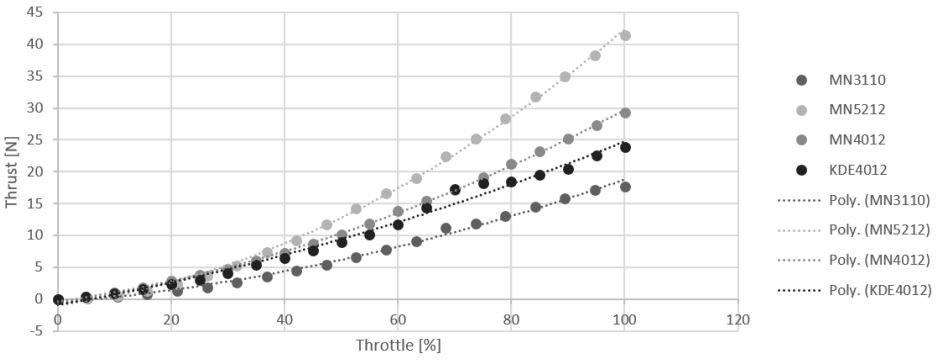

Figure 4.3: Thrust vs Throttle

The curves follow the expected quadratic relation for all motor-propeller combinations. Table 4.1 presents the throttle at which each motor reaches the required T/W ratio for hover, take-off and landing, as well as the T/W ratio available at maximum throttle.

All rotors respect the required T/W ratio, with significantly more thrust available. Configuration one performed VTOL with a 70%-75% throttle, having an available T/W ratio of 1.7. Since the avionics team determined that the controller wouldn't perform properly at a T/W ratio of 1.29, making 1.3 the bare minimum, the extra thrust available may come as a benefit. However, if after VTOL flight tests the thrust output is deemed too high, some estimations can be performed to determine whether a smaller propeller can increase efficiency while still respecting project requirements.

[1]Configuration four's rear motor was not purchased within the acceptable time-frame, therefore experimental data is only available for the remaining configurations.

	Configuration 1	Configuration 2 & 3	
	All Rotors	Front Rotors	Rear Rotors
Throttle Take-off [%]	73.94	51.15	82.20
Throttle Hover [%]	71.55	53.04	80.02
Throttle Landing [%]	69.08	51.15	77.71
T/W_{Max}	1.70	2.57	1.51

Table 4.1: Throttle and T/W comparison

On the other hand, configuration two is oversized, especially regarding the front rotors. The unavailability of the chosen propellers hinders efficiency since the motors will only be used at around 50% throttle. The other available propellers at T-motors with the desired diameter are significantly heavier and inadequate for the application, meaning other brands must be surveyed to find a better solution.
Nevertheless, the front and rear rotors of configurations two and three are partially covered, reducing the actual thrust output and thus the T/W ratio. The experimental results for rotor coverage presented later in this chapter will determine whether the chosen propulsion system is oversized.

4.2.2 Thrust vs Power

The relationship between thrust and power for the VTOL motors is showcased on figure 4.4, where black lines represent experimental data and grey lines data derived from vortex theory.

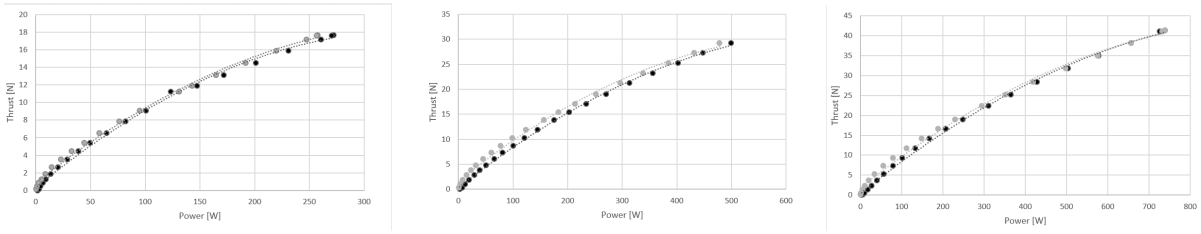

(a) Front rotors of configurations 2 & 3 (b) All rotors of configuration 1 (c) Rear rotors of configuration 2 & 3

Figure 4.4: Thrust vs Power performance

Regardless of the differences between the model and the experimental procedure, the results of the static test are very close to the ones from vortex theory for all three ESC-motor-propeller combinations, validating the previous use of the model to estimate performance in static cases. Table 4.2 presents the relative differences between the two results for the thrust obtained at 100% throttle, where the error goes up to 5.18%. At low throttle values, the error goes up to 20%. This, however, has a low impact on the system, as the motors will be used at higher throttle settings.
Comparing the maximum thrust output with the one provided by the manufacturer, all comparable motors present more thrust at maximum throttle while consuming additional power. The extra thrust can be explained by the use of a fully charged battery - over 22.2 V - during the experimental procedure, reaching higher RPM values and requiring more power. This comparison was not performed for the forward-flight system since there was no interest in assessing the static performance of the ESC-motor-propeller combination. The comparison with the model will be done with future flight tests featuring fixed-wing mission

	Configuration 1	Configuration 2 & 3	
	All Rotors	Front Rotors	Rear Rotors
Thrust [N]	29.23	17.61	41.12
Experimental Power [W]	498.92	270.48	725.50
Vortex Theory Power [W]	477.97	256.46	732.17
Difference [%]	4.20	5.18	0.92

Table 4.2: VTOL results

segments.

Table 4.3 presents the comparison in power demands for hover, take-off and landing for the different configurations, where the reference is the power required by configuration one.

	Configuration 1	Configuration 2 & 3
Hover [W]	936.99	948.57
Hover [%]	100	101.24
Take-off [W]	1000.94	1015.47
Take-off [%]	100	101.45
Landing [W]	874.78	883.58
Landing [%]	100	101.01

Table 4.3: VTOL experimental comparison

Configurations two and three consume slightly more power at every flight stage. However, the 1% difference is a small penalty when compared to the advantages of having an asymmetric thrust distribution. Additionally, the data corroborated the initial assumption that power consumption for a given T/W ratio and total disc area doesn't significantly change with rotor position [2].

With the power required for the different VTOL mission segments, a new estimation for battery mass can be performed to obtain a more accurate prediction of the mass of the propulsion system. Table 4.4 presents these results where the estimations for cruise power presented in the previous chapter were used [3][4].

	Configuration 1	Configuration 2	Configuration 3
Total Energy [Wh]	73.42	81.55	72.69
Total Energy [%]	100	111.07	99.01
Battery Mass [kg]	0.431	0.479	0.427
Total Mass [kg]	1.546	1.717	1.351
Total Mass [%]	100	111.06	87.39

Table 4.4: VTOL system's mass - uncovered

When compared to the estimations performed in Chapter 3, the same tendency is observed and the total system mass of the different configurations doesn't change significantly, confirming the accuracy of

[2] The total disc area of configurations two and three is 94% relative to the disc area of configuration one.
[3] The relative results use configuration one as reference
[4] Without the rear motor of configuration four, its performance was not experimentally assessed.

the initial predictions.

Evaluating the configurations relative to each other, configuration three has the least energy demands and component mass, resulting in a significantly lighter propulsion system. While having the same VTOL system as configuration three, configuration two has a severe penalty in power consumption during cruise condition, due to a lower $\frac{L}{D}$, as well as a heavier component mas, featuring one extra rotor, that results in a significant propulsion system mass difference.

4.3 Rotor Coverage Experimental Results

To estimate the actual thrust output decrease due to wing-rotor interference and calculate the minimum distance between surfaces to fulfil project requirements, an experimental procedure was performed partially covering the rotors. Figure 4.5 presents the added components to the conventional static test bench.

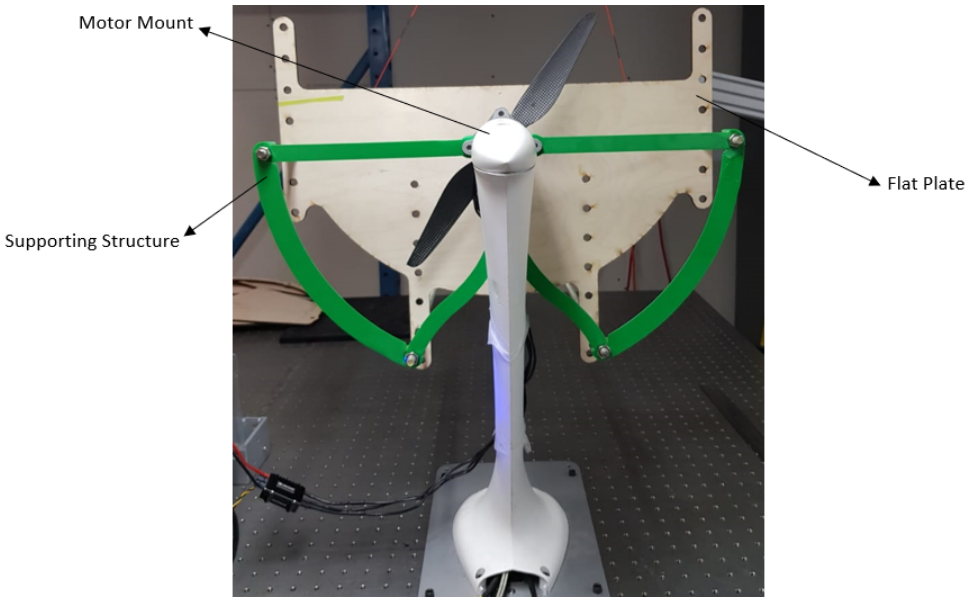

Figure 4.5: Experimental rotor coverage setup

The system is comprised of one 3D printed support structure, one wooden flat plate, four rods and eight washers. The green structure is attached to the motor mount, ensuring the load cells detect the net force produced. From this structure, four rods are screwed in, connecting the covering plate to the green support. The plate can move horizontally across the rods, reaching a maximum distance of 42 cm. As for the covered area, the plate can be moved vertically, changing the percentage of covered area, that will depend on the propeller used for the tests - 15”, in this case.

Covered Area and Distance

Prior to the experimental tests, the desired distance and covered area, relative to propeller dimensions had to be computed. Regarding the distance, it was defined that four different distances would be tested, going from 25% to 100%, relative to the propeller radius, plus an extra test at 200% to find

whether the predicted asymptotic behaviour of the curve was correct. The possible covered areas were pre-determined by the existing holes on the flat plate that together with the propeller dimensions would define the possible percentages of covered area. The method to calculate the covered area from the height of the plate is presented on figure 4.6.

$$d = R_P \cos\left(\frac{\theta}{2}\right) \tag{4.1}$$

$$\theta = 2\cos^{-1}\left(\frac{d}{R_P}\right) \tag{4.2}$$

$$A_c = {R_P}^2\left(\frac{\theta - \sin\theta}{2}\right) \tag{4.3}$$

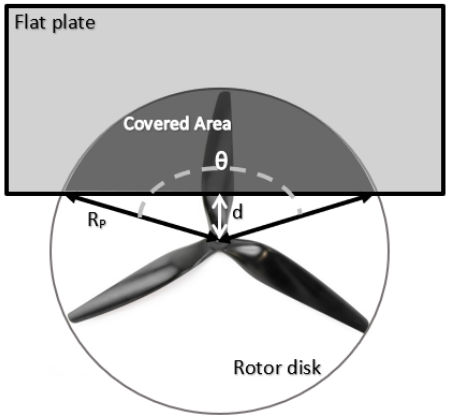

Figure 4.6: Covered area illustration

Knowing the vertical distance between the flat plate and the propeller d, as well as the propeller's radius R_P, the covered area can be calculated with equations 4.1 to 4.3 , where A_c is the covered area. Table 4.5 presents the covered areas with the propeller mentioned previously as reference.

	d [cm]	θ [rad]	A_c [cm^2]	A [%]
First position	8	2.28	274.45	24.07
Second position	4	2.72	418.77	36.73
Third position	0	π	570.05	50
Fourth position	-4	3.56	721.32	63.27
Fifth position	-8	4.01	865.63	75.93

Table 4.5: Experimental covered area

Each position corresponds to a set of four holes in the flat plate, where the rods should be placed in order to achieve the calculated covered area. Having five sets of different covered areas and five distances to test, there will be 25 different experimental procedures, with three runs each, for a total of 75 static tests.

Testing Procedure

The experimental tests followed a slightly different procedure from the one mentioned previously, as the influence of the supporting structure had to be accounted for and all voltage variation had to be eliminated. Figure 4.7 shows the procedure followed to obtain the experimental data.

All tests were completed with the components for the rear rotors of configurations two and three since these were the ones with the highest percentage of covered area.

The first round of tests was carried out with a battery as a power source. However, nor a battery nor a set of batteries in parallel were able to maintain a constant voltage across a batch of tests, significantly

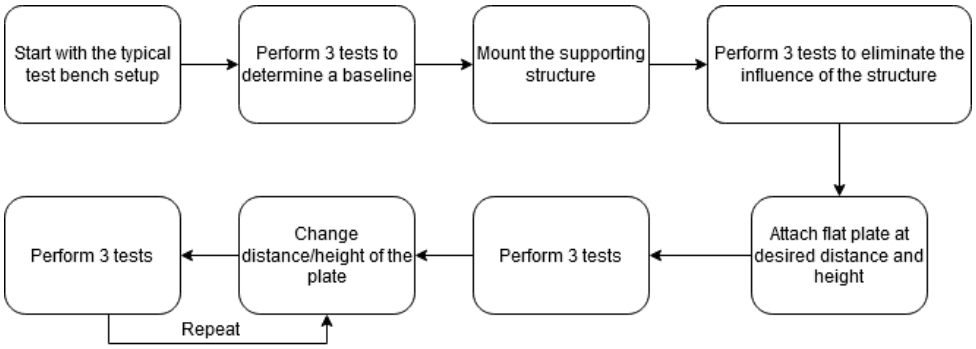

Figure 4.7: Experimental procedure

affecting the results. To solve this issue, a power source was used, keeping the available voltage and current at 24.5V and 50A, respectively. This solution allowed the tests to be performed on the same day, eliminating discrepancies associated with atmospheric conditions.

4.3.1 Data Treatment and Results

For each of the 25 cases, the three runs were averaged, having the thrust read at 0% throttle removed, as well as the influence of the green supporting structure. The results obtained are showcased on figures 4.8 and 4.9 [5].

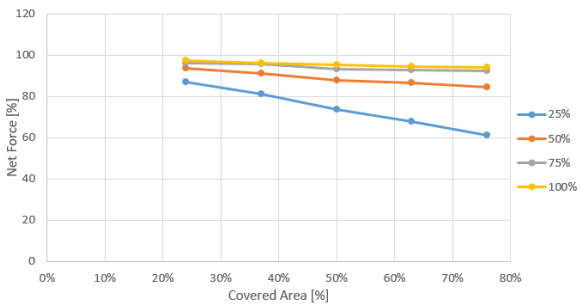

Figure 4.8: Net force variation with covered area

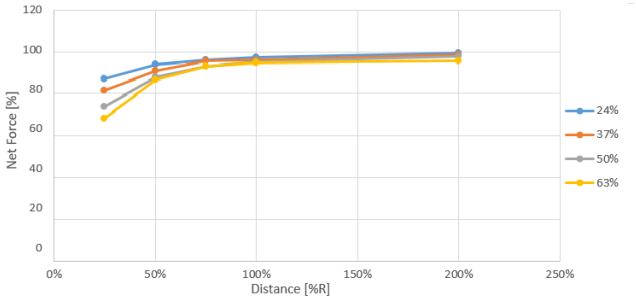

Figure 4.9: Net force variation with distance

In Figure 4.8, the predicted behaviour of thrust with the covered area is confirmed. For a distance of 25%, there is a decrease of over 25% in net force from a relative coverage of 24% to 76%, whereas for a distance of 100% the net force decrease is below 3.5%. Figure 4.9 also validates the tendency estimated with computational simulations, confirming the asymptotic behaviour of the net force with distance for all covered areas. As expected, the variation in net force is more significant for the cases with more covered area, decreasing 12.5% with coverage of 24% and 28% for a covered area of 63%, across the same relative distance variation.

Some conclusions can also be drawn for the data at 200% distance, where 24% coverage renders 99.63% net force while 63% coverage only renders 95.88% net force. This variation is significant enough to define that at 200% distance covered area still influences thrust output. Comparing the results at 100% and 200% distance, there is a difference from 1.2% to 2.2% between readings, implying that the

[5] The data for a covered area of 76% at 200% distance was omitted due to its clear contradiction of the remaining results.

asymptotic behaviour is already present at 100% relative distance.

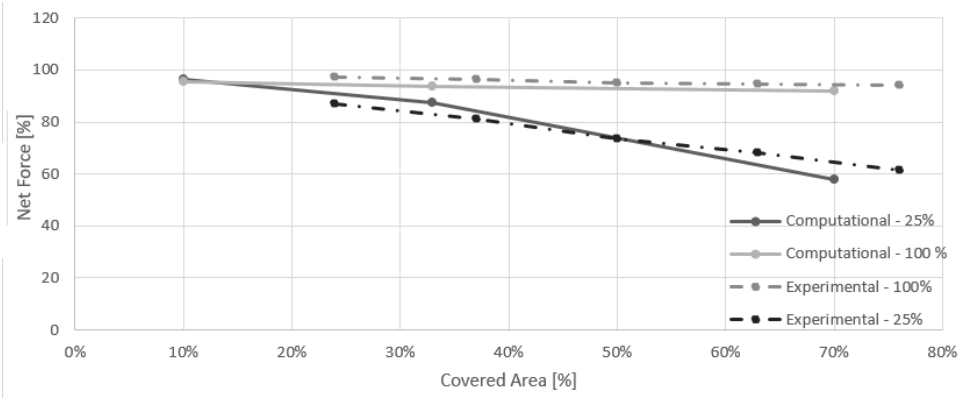

Figure 4.10: Experimental and computational data for a distance of 25% and 100%

Figure 4.10 presents the comparison between experimental and computational data for 25% and 100% distances relative to the radius. For both distances the experimental and computational data are similar, showing the same linear tendency.

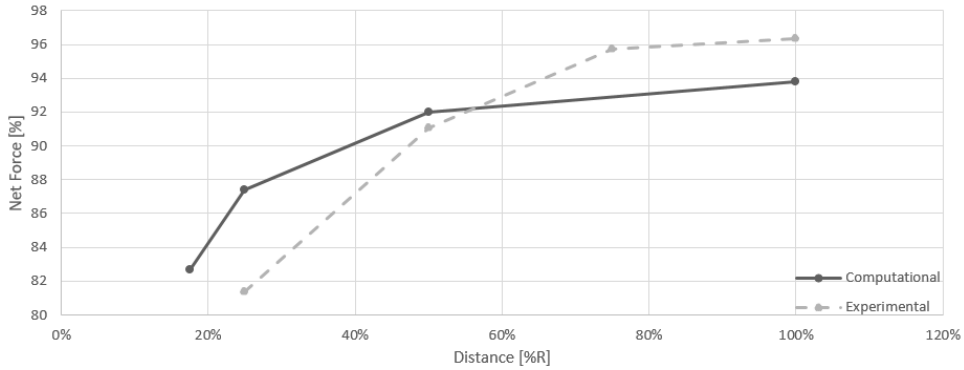

Figure 4.11: Experimental and computational data for a covered distance of 33% and 37%

On the other hand, figure 4.11 shows larger discrepancies between computational and experimental results. Given that the comparison is not done for the same covered area - 33% computational and 37% experimental - some differences are to be expected. Additionally, the data gathered from computational simulations were obtained with a 23” propeller with significantly different characteristics from the 15” propeller used experimentally. Regardless of the differences in the studies, both data curves show the beginning of an asymptotic behaviour at 100% relative distance as well as an increase in net force with distance.

With the experimental data, the minimum relative distance at which the rotors must be placed to fulfil project requirements can be calculated for the rear rotors of configurations two, three and four with interpolations[6]. The data from table 4.1 was used to estimate the minimum thrust required per motor-propeller configuration as well as the manufacturer’s data for the rear motor of configuration four. Table 4.6 shows these results.

The required thrust from both rotors is similar to the one obtained with computational data, having a

[6]This was not performed for the front rotors, which would require data extrapolation.

Rear Rotors	Configurations 2 & 3	Configuration 4
Available T/W	1.5	1.45
Required Thrust [%]	86.66	89.66
Required distance [%]	53.75	62.2
Required distance [cm]	10.25	17.34

Table 4.6: Experimental required rotor-wing distance

discrepancy of less than 1% relative to the predictions presented in the previous chapter.

To obtain a similar trend in both computational and experimental curves the difference between the data was linearized. Figure 4.12 presents both data sets.

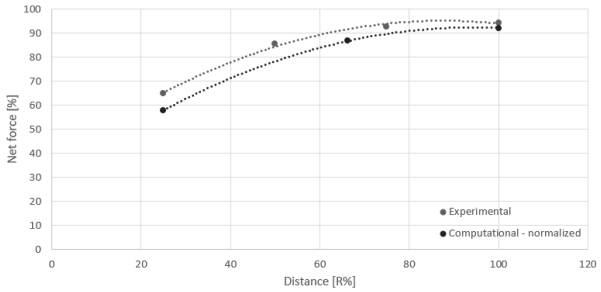

Figure 4.12: Experimental and computational data interpolated for an area of 69%

Table 4.7 shows the final results for the minimum required distance between the rotor and wing.

Rear Rotors	Configurations 2 & 3	Configuration 4
Available T/W	1.5	1.45
Required Thrust [%]	86.66	89.66
Required distance - Computational [%]	66.19	65.76
Required distance - Experimental [%]	53.75	51.22

Table 4.7: Experimental required rotor-wing distance

The difference between computational and experimental results is significant, with over 10% in both cases. As mentioned before, some of the discrepancies come from the use of different propellers as well as differences between the conditions set in the Ansys® model and the conditions during the experiment.

Given that the bare minimum to satisfy the project requirements is to place the rotors at about 65% of a radius of distance, a distance of 75% was defined, in order to have a safety margin. Assuming this 75% distance, the actual power consumption to perform the mission increases relative to uncovered rotors, increasing battery demands. Table 4.8 shows the new estimations for total mass of the system, accounting for the required battery of covered rotors at 75% distance, where once again the 10% coverage of front rotors of configurations two and three were neglected.

The data for configuration one is used as reference, since it is the base configuration, presenting all rotors uncovered. The 69% covered rotor area of configuration three affects its power consumption,

	Configuration 1	Configuration 2	Configuration 3
Total Energy [Wh]	73.42	84.8	75.96
Total Energy [%]	100	115.5	103.50
Battery Mass [kg]	0.431	0.498	0.446
Total Mass [kg]	1.546	1.736	1.370
Total Mass [%]	100	112.3	88.6

Table 4.8: VTOL system's mass - covered

increasing it relative to the uncovered case. Regardless, it performs the mission with over 10% less propulsion system mass due to an efficient cruise condition as well as a light component mass.
On the other hand, configuration two, with the same covered area, presents over 10% more propulsion system mass as a result of having a lift-and-cruise configuration with a pusher motor and a low $\frac{L}{D}$. Comparing with the uncovered situation, both configurations feature around 1% total mass increase, since the variation in required energy is about 4.5%. The data for configuration four was not presented, since its rear motor was not purchased for testing.

4.4 Motor Constants

The flight dynamics model developed for this UAV requires the torque and thrust constants of each motor, representing the torque and thrust relations to the propeller rotation, respectively. Since the static test bench setup does not include an RPM sensor, the propeller's angular speed was derived from the known power and torque, as seen in equation 4.4, where τ represents torque in Nm and Ω_p the propeller's rotation in rad/s.

$$P = \tau\Omega_p \tag{4.4}$$

Thrust Constant

The thrust constant K_T describes the relationship between thrust and rotation and can be derived from equation 4.5, below.

$$C_T = \frac{T}{\rho n^2 {d_P}^4} \Rightarrow T = C_T \rho d_P^4 n^2 = C_T \rho {d_P}^4 4\pi^2 {\Omega_p}^2 \Rightarrow K_T = C_T \rho {d_P}^4 4\pi^2, \tag{4.5}$$

where K_T is in $N/(rad/s)^2$, ρ is air density in kg/m^3, d_P is propeller diameter, *n* is the propeller rotational speed in rps, C_T is the thrust coefficient and Ω_p is the propeller rotational speed in rad/s.
To obtain this relation, the experimental thrust output of each motor-propeller combination was divided by the square of the angular velocity, in rad/s.

Torque Constant

Similarly to the thrust constant - K_τ, in $\frac{Nm}{rad/s^2}$ the torque constant represents the relationship between torque and propeller angular rotation. Its value can be determined analytically through equation 4.6.

$$C_\tau = \frac{\tau}{\rho n^2 d^5} \Rightarrow \tau = C_\tau \rho d^5 n^2 = C_\tau d^5 4\pi^2 {\Omega_p}^2 \Rightarrow K_\tau = C_\tau \rho d^5 4\pi^2 \tag{4.6}$$

This constant was also derived from experimental data by calculating the slope of trendline of the torque relationship with the square of propeller rotation. Figure 4.13 presents the curves obtained experimentally to calculate the required constants.

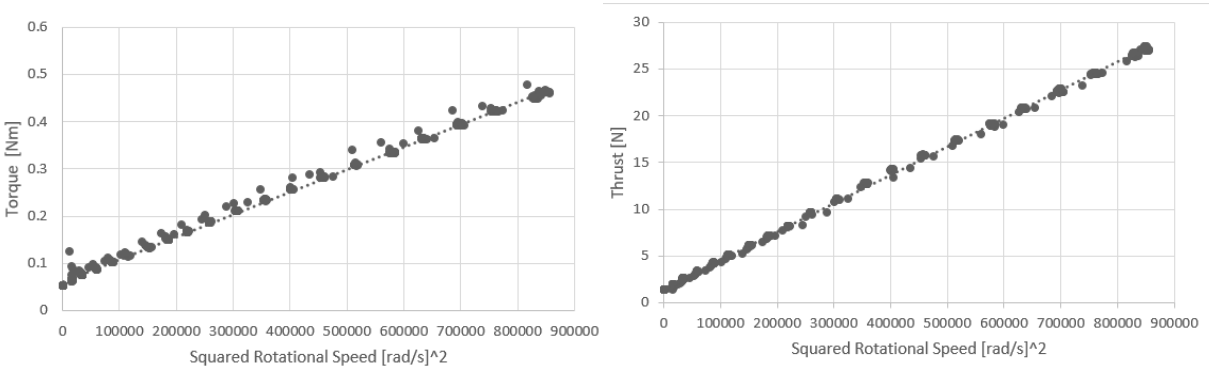

Figure 4.13: Thrust and torque curves with propeller rotational speed

Table 4.9 presents the averaged constants derived from experimental data for all the purchased motors.

Constant	$K_T \left[\frac{N}{rad/s^2}\right]$	$K_\tau \left[\frac{Nm}{rad/s^2}\right]$
MN4012 KV480	3.18×10^{-5}	4.95×10^{-7}
MN3110 KV470	1.71×10^{-5}	2.37×10^{-7}
MN5212 KV420	4.90×10^{-5}	8.36×10^{-7}
KDE4012 KV400	4.00×10^{-5}	1.29×10^{-7}

Table 4.9: Thrust and torque constants

Chapter 5

Flight Dynamic Modeling

This chapter describes the flight dynamics model developed for configurations one through three, listing the changes that must be made to adapt it into a trirotor propulsion system for configuration four. It explains the assumptions and approximations made during the model's development, presents the controller and its tuning, showcasing the results obtained.

5.1 Quadrotor Dynamics

The typical dynamics model of a quadrotor assumes the UAV is a point-mass rigid-body and accounts for thrust and torque, neglecting aerodynamic forces. This approximation is somewhat accurate due to the size and type of airframe of the usual quadrotor.
However, the developed configurations follow a geometry similar to an aircraft, with a wing and canard as well as actuators that produce aerodynamic forces too significant to neglect, even in multicopter mode. The derived model describes the dynamics of the quadrotor configurations when functioning in multicopter mode with the system of six equations presented below.

$$\begin{cases} F_{x_a} + F_{x_p} = m(\dot{u} + qw - vr) + W\sin\theta \\ F_{y_a} + F_{y_p} = m(\dot{v} + ur - pw) - W\cos\theta\sin\phi \\ F_{z_a} + F_{z_p} = m(\dot{w} + vp - uq) - W\cos\theta\cos\phi \\ M_{x_a} + M_{x_p} = I_{xx}\dot{p} - I_{xz}(\dot{r} + pq) + qr(I_{zz} - I_{yy}) \\ M_{y_a} + M_{y_p} = I_{yy}\dot{q} + I_{xz}(p^2 - r^2) + pr(I_{xx} - I_{zz}) \\ M_{z_a} + M_{z_p} = I_{zz}\dot{r} + I_{xz}(qr - \dot{p}) + pq(I_{yy} - I_{xx}) \end{cases} \tag{5.1}$$

Where F_{x_a}, F_{y_a}, F_{z_a}, M_{x_a}, M_{y_a} and, M_{z_a} are aerodynamic forces and moments, F_{x_p}, F_{y_p}, F_{z_p}, M_{x_p}, M_{y_p} and, M_{z_p} are propulsive forces and moments, *m* is mass in kg, W is the UAV's weight in N and I is the UAV's moment of inertia in kgm^2. The linear velocity is represented by the three dimensional vector of components u, v, w in m/s, the angular velocity is given by p, q, r, in rad/s, and the Euler angles are given by ϕ, θ and ψ, in the x, y and z directions, respectively, in rad.

5.1.1 Propulsive Forces and Moments

The propulsive components of force and moments can be accounted for as a function of propeller rotational speed, as mentioned in the previous chapter. Equations 5.2 and 5.3 translate this relation.

$$T_i = K_{T_i} {\Omega_{p_i}}^2 \tag{5.2}$$

$$\tau_i = K_{\tau_i} {\Omega_{p_i}}^2 \tag{5.3}$$

Where T_i, τ_i and Ω_{p_i} are the thrust, torque and angular velocity of the i^{th} rotor. The K_τ and K_T constants correspond to the torque and thrust constants calculated previously. Using the relations presented on equations 5.2 and 5.3, as well as the reference frame shown on figure 5.1, the propulsive force and torque can be computed, calculating the moments that arise as consequence.

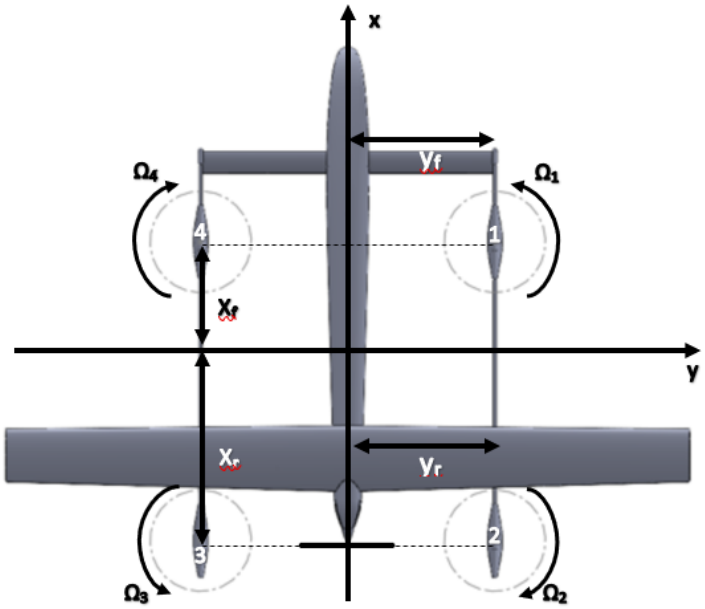

Figure 5.1: Reference Frame

Since the studied case is a UAV in quadcopter mode, there is only thrust in the z-direction, neglecting the thrust produced by a pusher in the other directions during fixed-wing flight. The equations that define the propulsive forces and moments are presented on the system 5.4, below.

$$\begin{cases} F_{z_p} = -(K_{T_1} {\Omega_{p_1}}^2 + K_{T_2} {\Omega_{p_2}}^2 + K_{T_3} {\Omega_{p_3}}^2 + K_{T_4} {\Omega_{p_4}}^2) \\ M_{x_p} = y_f(K_{T_4} {\Omega_{p_4}}^2 - K_{T_1} {\Omega_{p_1}}^2) + y_r(K_{T_3} {\Omega_{p_3}}^2 - K_{T_2} {\Omega_{p_2}}^2) \\ M_{y_p} = xf(K_{T_1} {\Omega_{p_1}}^2 + K_{T_4} {\Omega_{p_4}}^2) - x_r(K_{T_3} {\Omega_{p_3}}^2 + K_{T_2} {\Omega_{p_2}}^2) \\ M_{z_p} = K_{\tau_1} {\Omega_{p_1}}^2 - K_{\tau_2} {\Omega_{p_2}}^2 + K_{\tau_3} {\Omega_{p_3}}^2 - K_{\tau_4} {\Omega_{p_4}}^2 \end{cases} \tag{5.4}$$

These equations assume rotors one and four are at distance (x_f, y_f) of the centre of gravity while rotors two and three are at distance (x_r, y_r). This differentiation allows the model to be easily adjusted from

configuration one to configurations two and three. Table 5.1 shows the values of these variables for each configuration.

Distance	Configuration 1	Configuration 2 & 3
x_f [m]	0.5238	0.891
x_r [m]	0.5238	0.222
y_f [m]	0.51	0.483
y_r [m]	0.51	0.242

Table 5.1: Rotor distance to the CG

5.1.2 Aerodynamic Forces and Moments

The quadrotor is subject to several complex aerodynamic effects, such as ground effect, propeller performance, wall effect and even rotor inflow damping [111][112]. These may be relevant to analyze performance but can be neglected in the scope of a simplified flight dynamics model.

Furthermore, the approximation of the UAV's motion to a simple multicopter, eliminating fixed-wing flight mode, can reduce the aerodynamic effects to drag in the multiple directions, as well as the moments that arise from it.

The drag in the longitudinal direction was computed traditionally, using the drag coefficient obtained through Ansys® simulations. Regarding the lateral direction, the drag force was approximated to the fuselage drag, since wing and canard are less influential. Finally, the vertical drag force was estimated, accounting for the components with origin in the fuselage, canard and wing. Equations 5.5 to 5.7 present the estimated drag components in the three directions.

$$F_{a_x} = D_x = -\frac{1}{2}\rho C_{d_0} S_w u^2 \tag{5.5}$$

$$F_{a_y} = D_y = -\frac{1}{2}\rho C_{d_f} S_f v^2 \tag{5.6}$$

$$F_{a_z} = D_z = -\frac{1}{2}\rho (C_{d_w} S_w + C_{d_c} S_c + 0.5 C_{d_f} S_f) w^2 \tag{5.7}$$

Where S_c, S_f and S_w represent the canard, fuselage and wing bottom surfaces in m^2. Table 5.2 presents the values of the surface areas of the different UAV parts.

Surface	Canard	Fuselage	Wing
Surface Area [m^2]	0.08	0.61	0.5

Table 5.2: Aerodynamic surface areas

The drag coefficient $C_{d_{\alpha_0}}$, shown on equation 5.5, corresponds to the zero angle of attack coefficient, where the induced drag was neglected due to insufficient production of lift. As for the drag coefficient of the fuselage C_{d_f}, present on equations 5.6 and 5.7, it was approximated to the cylinder drag coefficient.

The remaining drag coefficients, C_{d_w} and C_{d_c}, were approximated to the drag coefficient of a flat plate. The values of the coefficients used are presented below.

- Drag coefficient on a flat plate - C_{d_c} & C_{d_w} - 1.98 [113]
- Drag coefficient on a cylinder - C_{d_f} - 2.1 [114]
- Zero angle of attack drag coefficient - C_{d_0} - 0.044284 and 0.0506, for configurations one and two & three, respectively.

Knowing the aerodynamic forces acting on the quadrotor, the aerodynamic moments can also be estimated. In the longitudinal direction, the moment is approximated to zero, since the influence of v, p and r are assumed to be negligible. The lateral moment M_{a_y} was calculated from F_{a_z}, multiplying the different drag components by their distance to the centre of gravity. Figure 5.2 presents an illustration of the position of the vertical aerodynamic forces.

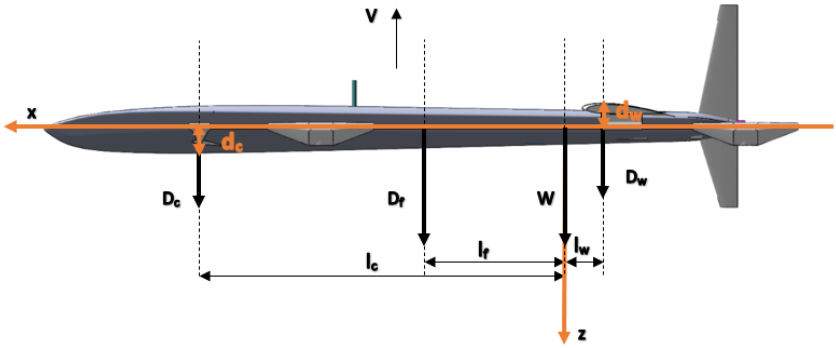

Figure 5.2: Vertical aerodynamic forces

Table 5.3 presents the distances required to compute the lateral moment, where it was assumed that the drag forces of the wing and canard are applied at mid-chord, and not quarter chord, as it is an approximation to a flat plate and not an airfoil. The fuselage drag is assumed to be at the geometric centre of the fuselage.

Surface	Canard	Fuselage	Wing
Distance [m]	0.822	0.438	0.138

Table 5.3: Aerodynamic distances

Using the data presented in table 5.3, the lateral moment was computed with equation 5.8.

$$M_{a_y} = \frac{1}{2}\rho(-C_{d_w}S_w d_w + C_{d_c}S_c d_c + 0.5C_{d_f}S_f d_f)w^2 \tag{5.8}$$

The moment in the vertical direction - given by equation 5.9 - was computed by assuming a uniform distribution of drag along the fuselage in the lateral direction, applied at the geometric centre.

$$M_{a_z} = -\frac{1}{2}\rho C_{d_f}\frac{S_f}{2}d_f v^2 \tag{5.9}$$

Figure 5.3, illustrates the position of the force relative to the centre of gravity.

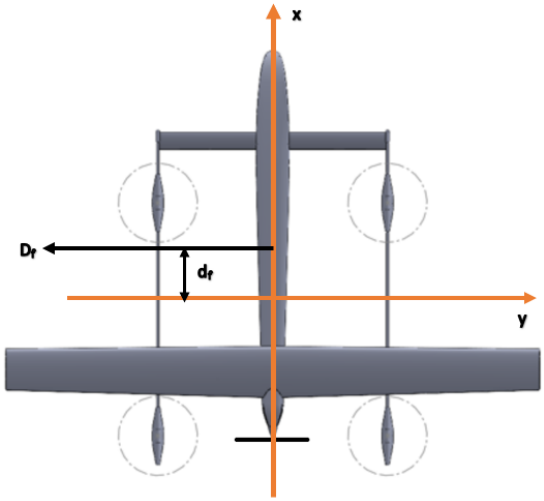

Figure 5.3: Vertical aerodynamic moment

5.1.3 Linearization

Admitting that physical systems have nonlinearities, their behaviour can often be represented with a reasonable degree of accuracy by a linear approximation around an equilibrium point. This approach has the advantage of simplifying the system, allowing the application of linear control techniques, at the cost of only being valid within a range, containing the chosen equilibrium point. To linearize the system, each variable was decomposed in two - the equilibrium value and the variation, as shown in equation 5.10.

$$x = x_0 + \Delta x \tag{5.10}$$

Where x_0 represents the equilibrium term and Δx the disturbance term. Applying this method to the rotational and translational equations of motion presented above, the force and moment variations can be computed, as shown in equation 5.11.

$$\begin{cases} \Delta F_x = m(\Delta \dot{u} + q_0\Delta w + w_0\Delta q - v_0\Delta r - r_0\Delta v + g\cos\theta_0\Delta\theta) \\ \Delta F_y = m(\Delta \dot{v} + u_0\Delta r + r_0\Delta u - p_0\Delta w - w_0\Delta p - g\cos\theta_0\cos\phi_0\Delta\phi + g\sin\theta_0\sin\phi_0\Delta\theta) \\ \Delta F_z = m(\Delta \dot{w} + v_0\Delta p + p_0\Delta v - u_0\Delta q - q_0\Delta u + g\cos\theta_0\sin\phi_0\Delta\phi + g\sin\theta_0\cos\phi_0\Delta\theta) \\ \Delta M_x = I_{xx}\Delta\dot{p} - I_{xz}(\Delta\dot{r} + p_0\Delta q + q_0\Delta p) + (I_{zz} - I_{yy})(q_0\Delta r + r_0\Delta q) \\ \Delta M_y = I_{yy}\Delta\dot{q} + 2I_{xz}(p_0\Delta p - r_0\Delta r) + (p_0\Delta r + r_0\Delta p)(I_{xx} - I_{zz}) \\ \Delta M_z = I_{zz}\Delta\dot{r} - I_{xz}\Delta\dot{p} + (p_0\Delta q + q_0\Delta p)(I_{yy} - I_{xx}) + I_{xz}(q_0\Delta r + r_0\Delta q) \end{cases} \tag{5.11}$$

Assuming the state of equilibrium around which the equations are linearized is hover - compatible with a UAV in multicopter mode, all equilibrium variables have the value of zero, simplifying the equations to the ones presented below.

$$\begin{cases} \Delta F_x = m\Delta\dot{u} + mg\Delta\theta \\ \Delta F_y = m\Delta\dot{v} - mg\Delta\phi \\ \Delta F_z = m\Delta\dot{w} \\ \Delta M_x = I_{xx}\Delta\dot{p} - I_{xz}\Delta\dot{r} \\ \Delta M_y = I_{yy}\Delta\dot{q} \\ \Delta M_z = I_{zz}\Delta\dot{r} - I_{xz}\Delta\dot{p} \end{cases} \tag{5.12}$$

Propulsive Forces and Moments

The propulsive terms can also be linearized around an equilibrium point, by calculating the trim propeller rotation - Ω_0 required to achieve hover condition. This calculation was performed for configuration one as well as configurations two and three and presented on equations 5.13 and 5.14, respectively.

$$\begin{cases} \Omega_{0_1} = \sqrt{\frac{mg}{4K_T}} \\ \Omega_{0_2} = \sqrt{\frac{mg}{4K_T}} \\ \Omega_{0_3} = \sqrt{\frac{mg}{4K_T}} \\ \Omega_{0_4} = \sqrt{\frac{mg}{4K_T}} \end{cases} \tag{5.13}$$

$$\begin{cases} \Omega_{0_1} = \sqrt{\frac{0.1mg}{K_T}} \\ \Omega_{0_2} = \sqrt{\frac{0.4mg}{K_T}} \\ \Omega_{0_3} = \sqrt{\frac{0.4mg}{K_T}} \\ \Omega_{0_4} = \sqrt{\frac{0.1mg}{K_T}} \end{cases} \tag{5.14}$$

Linearizing equations 5.4, the following system of equations can be obtained.

$$\begin{cases} \Delta F_{z_p} = -2(K_{T_1}\Omega_{0_1}\Delta\Omega_1 + K_{T_2}\Omega_{0_2}\Delta\Omega_2 + K_{T_3}\Omega_{0_3}\Delta\Omega_3 + K_{T_4}\Omega_{0_4}\Delta\Omega_4) \\ \Delta M_{x_p} = 2y_f(K_{T_4}\Omega_{0_4}\Delta\Omega_4 - K_{T_1}\Omega_{0_1}\Delta\Omega_1) + 2y_r(K_{T_3}\Omega_{0_3}\Delta\Omega_3 - K_{T_2}\Omega_{0_2}\Delta\Omega_2) \\ \Delta M_{y_p} = 2x_f(K_{T_1}\Omega_{0_1}\Delta\Omega_1 + K_{T_4}\Omega_{0_4}\Delta\Omega_4) - 2x_r(K_{T_3}\Omega_{0_3}\Delta\Omega_3 + K_{T_2}\Omega_{0_2}\Delta\Omega_2) \\ \Delta M_{z_p} = 2K_{\tau_1}\Omega_{0_1}\Delta\Omega_1 - 2K_{\tau_2}\Omega_{02}\Delta\Omega_2 + 2K_{\tau_3}\Omega_{0_3}\Delta\Omega_3 - 2K_{\tau_4}\Omega_{0_4}\Delta\Omega_4 \end{cases} \tag{5.15}$$

Aerodynamic Forces and Moments

Similarly to the previous section, the aerodynamic forces and moments can be linearized around hover condition, as shown in equation 5.16.

$$\begin{cases} \Delta F_{x_a} = \rho C_{d_0} S_w u_0 \Delta u \\ \Delta F_{y_a} = -\rho C_{D_f} S_f v_0 \Delta v \\ \Delta F_{z_a} = -\rho(C_{d_w} S_w + C_{d_c} S_c + C_{d_f}\frac{S_f}{2}) w_0 \Delta w \\ \Delta M_{x_a} = 0 \\ \Delta M_{y_a} = M_w = \rho(C_{D_w}(S_c d_c - S_w d_w) + C_{D_f}\frac{S_f}{2} d_f) w_0 \Delta w \\ \Delta M_{z_a} = -\frac{1}{2}\rho C_{d_f}\frac{S_f}{2} d_f v_0 \Delta v \end{cases} \tag{5.16}$$

Since all equilibrium terms are zero, the aerodynamic forces aren't accounted for in the current linear model. To address this issue, considering that drag is the most relevant aerodynamic force acting on the quadcopter, the components that arise due to the square of the perturbation shall be considered, introducing non-linearities in the system, as shown below.

$$\begin{cases} F_{x_a} = -\frac{1}{2}\rho C_{d_0} S_w \Delta u^2 = X_u \Delta u \\ F_{y_a} = -\frac{1}{2}\rho C_{D_f} S_f \Delta v^2 = Y_v \Delta v \\ F_{z_a} = -\frac{1}{2}\rho (C_{d_w}(S_w + S_c) + 0.5 C_{d_f} S_f) \Delta w^2 = Z_w \Delta w \\ M_{x_a} = 0 \\ M_{y_a} = -\frac{1}{2}\rho (C_{D_w}(S_w d_w + S_c d_c) + C_{D_f} \frac{S_f}{2} d_f) \Delta w^2 = M_w \Delta w \\ M_{z_a} = -\frac{1}{2}\rho C_{d_f} \frac{S_f}{2} d_f \Delta v^2 = N_v \Delta v \end{cases} \tag{5.17}$$

Where X_u, Y_v, Z_w, M_w and N_v are variable matrix coefficients and not the force derivatives, as they are used in other literature.

5.1.4 Mathematical Model

Given the equations derived previously, it is possible to express the dynamics of the system in matrix form, by means of equation 5.18.

$$\begin{bmatrix} \Delta F \\ \Delta M \end{bmatrix} = A\Delta x + B\Delta u \tag{5.18}$$

Where ΔX is the state vector, comprised of the variations in linear and angular velocity, as well as the Euler angles and earth frame positions, and ΔU is the actuator vector, containing the variations in rotor angular velocity. Both these vectors are presented on equations 5.19 and 5.20.

$$\Delta X = \begin{bmatrix} \Delta u & \Delta v & \Delta w & \Delta p & \Delta q & \Delta r & \Delta x & \Delta y & \Delta z & \Delta \phi & \Delta \theta & \Delta \psi \end{bmatrix}^T \tag{5.19}$$

$$\Delta U = \begin{bmatrix} \Delta \Omega_1 & \Delta \Omega_2 & \Delta \Omega_3 & \Delta \Omega_4 \end{bmatrix}^T \tag{5.20}$$

The A and B matrices represent the dynamics and actuation of the system, respectively. These matrices and their coefficients are presented below.

$$A = \begin{bmatrix} X_u & 0 & 0 & 0 & 0 & 0 & 0 & 0 & 0 & 0 & -mg & 0 \\ 0 & Y_v & 0 & 0 & 0 & 0 & 0 & 0 & 0 & mg & 0 & 0 \\ 0 & 0 & Z_w & 0 & 0 & 0 & 0 & 0 & 0 & 0 & 0 & 0 \\ 0 & 0 & 0 & 0 & 0 & 0 & 0 & 0 & 0 & 0 & 0 & 0 \\ 0 & 0 & M_w & 0 & 0 & 0 & 0 & 0 & 0 & 0 & 0 & 0 \\ 0 & N_v & 0 & 0 & 0 & 0 & 0 & 0 & 0 & 0 & 0 & 0 \end{bmatrix} \tag{5.21}$$

The A matrix accounts for all the aerodynamic effects, such as drag and the moments it produces, as well as the weight components on each direction. It accounts for the non-linearities and changes at each timestep, as it contains variables of the state vector in its coefficients.

$$B = \begin{bmatrix} 0 & 0 & 0 & 0 \\ 0 & 0 & 0 & 0 \\ -2K_{T_1}\Omega_{0_1} & -2K_{T_2}\Omega_{0_2} & -2K_{T_3}\Omega_{0_3} & -2K_{T_4}\Omega_{0_4} \\ -2\Omega_{0_1}K_{T_1}y_f & -2\Omega_{0_2}K_{T_2}y_r & 2\Omega_{0_3}K_{T_3}y_r & 2\Omega_{0_4}K_{T_4}y_f \\ 2x_fK_{T_1}\Omega_{0_1} & -2x_rK_{T_2}\Omega_{0_2} & -2x_rK_{T_3}\Omega_{0_3} & 2x_fK_{T_4}\Omega_{0_4} \\ 2\Omega_{0_1}K_{\tau_1} & -2\Omega_{0_2}K_{\tau_2} & 2\Omega_{0_3}K_{\tau_3} & -2\Omega_{0_4}K_{\tau_4} \end{bmatrix} \tag{5.22}$$

The B matrix accounts for the force and moment variations due to rotor actuation, using the thrust and torque constants as well as the trim velocity. Unlike the A matrix, the B matrix does not have any non-linear coefficients.

With all the necessary vectors and matrices defined, the quadrotor's dynamics can be computed from equation 5.18, by substituting the mentioned variables, as seen below.

$$\begin{bmatrix} \Delta F_x \\ \Delta F_y \\ \Delta F_z \\ \Delta M_x \\ \Delta M_y \\ \Delta M_z \end{bmatrix} = \begin{bmatrix} X_u & 0 & 0 & 0 & 0 & 0 & 0 & 0 & 0 & 0 & -mg & 0 \\ 0 & Y_v & 0 & 0 & 0 & 0 & 0 & 0 & 0 & mg & 0 & 0 \\ 0 & 0 & Z_w & 0 & 0 & 0 & 0 & 0 & 0 & 0 & 0 & 0 \\ 0 & 0 & 0 & 0 & 0 & 0 & 0 & 0 & 0 & 0 & 0 & 0 \\ 0 & 0 & M_w & 0 & 0 & 0 & 0 & 0 & 0 & 0 & 0 & 0 \\ 0 & N_v & 0 & 0 & 0 & 0 & 0 & 0 & 0 & 0 & 0 & 0 \end{bmatrix} \Delta X \; + \; \begin{bmatrix} 0 & 0 & 0 & 0 \\ 0 & 0 & 0 & 0 \\ -2K_{T_1}\Omega_{0_1} & -2K_{T_2}\Omega_{0_2} & -2K_{T_3}\Omega_{0_3} & -2K_{T_4}\Omega_{0_4} \\ -2\Omega_{0_1}K_{T_1}y_f & -2\Omega_{0_2}K_{T_2}y_r & 2\Omega_{0_3}K_{T_3}y_r & 2\Omega_{0_4}K_{T_4}y_f \\ 2x_fK_{T_1}\Omega_{0_1} & -2x_rK_{T_2}\Omega_{0_2} & -2x_rK_{T_3}\Omega_{0_3} & 2x_fK_{T_4}\Omega_{0_4} \\ 2\Omega_{0_1}K_{\tau_1} & -2\Omega_{0_2}K_{\tau_2} & 2\Omega_{0_3}K_{\tau_3} & -2\Omega_{0_4}K_{\tau_4} \end{bmatrix} \Delta U$$

This mathematical model will be used in the Simulink® model to predict the behaviour of the quadrotor, computing the variation in forced and moments due to a variation in state and actuation at each timepstep.

5.2 Simulink ® Model

A Simulink ® model was derived, in combination with MATLAB ® scripts to simulate the behaviour of the quadrotor, registering its response to different stimuli. This model is comprised of three MATLAB® scripts, that calculate trim conditions, forces and moments and actuator gains, as well as a Simulink® block.

5.2.1 Model Description

The model is run through a MATLAB® script, where the *trim* function is called. This function computes the hover propeller rotation for a given choice of configuration, knowing the motor's thrust and torque constants, as well as the UAV's mass and inertia. It outputs the reference state vector, xref. This vector is subtracted from the current state to obtain Δx, that goes into the function *dof*, together with the actuator vector Δu. This function will then calculate the variation in forces and moments, through the derived flight dynamics model, and input them into the last block. Figure 5.4 presents the process described thus far.

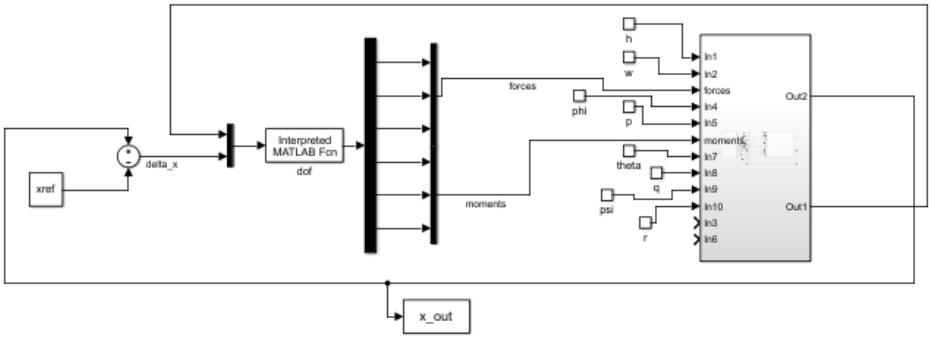

Figure 5.4: Simulink model overview

The calculated variations on the forces and moments are then imputed into a six degree of freedom equation of motion (6DOF EoM) Simulink ® block, that calculates velocity and rates in the body frame, Euler angles as well as the position in the fixed frame coordinates, corresponding to the new state. This state is then transmitted to the control block, as shown in figure 5.5.

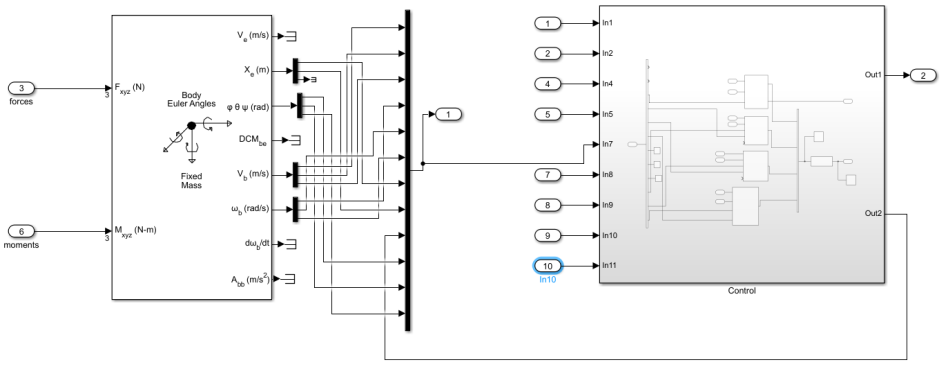

Figure 5.5: Simulink model DOF and control blocks

The control block contains one block for altitude control and three blocks for attitude control, in roll, pitch and yaw, respectively. The altitude and attitude blocks have the same type of structure, outputting a signal each that is then passed to the *gains* function, that calculates the new Δu vector, defining the actuation on all four rotors. This is presented on figure 5.6.

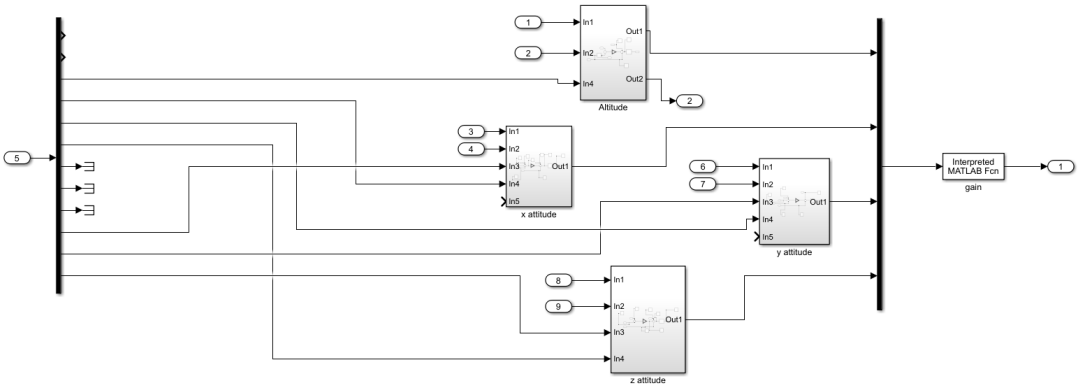

Figure 5.6: Simulink control blocks

The *gains* function uses a mixer matrix to calculate the inputs to the rotors from the signals that exit the PID controllers. The operation behind it is presented below.

$$\begin{bmatrix} \Delta\Omega_1 \\ \Delta\Omega_2 \\ \Delta\Omega_3 \\ \Delta\Omega_4 \end{bmatrix} = \begin{bmatrix} -2K_{T_1}\Omega_{0_1}/m & -2K_{T_2}\Omega_{0_2}/m & -2K_{T_3}\Omega_{0_3}/m & -2K_{T_4}\Omega_{0_4}/m \\ -2\Omega_{0_1}\frac{I_{xz}K_{\tau_1}+I_{zz}K_{T_1}y_f}{I_{xx}I_{zz}-{I_{xz}}^2} & 2\Omega_{0_2}\frac{I_{xz}K_{\tau_2}-I_{zz}K_{T_2}y_r}{I_{xx}I_{zz}-{I_{xz}}^2} & 2\Omega_{0_3}\frac{-I_{xz}K_{\tau_3}+I_{zz}K_{T_3}y_r}{I_{xx}I_{zz}-{I_{xz}}^2} & 2\Omega_{0_4}\frac{I_{xz}K_{\tau_4}+I_{zz}K_{T_4}y_f}{I_{xx}I_{zz}-{I_{xz}}^2} \\ \frac{2x_fK_{T_1}\Omega_{0_1}}{I_{yy}} & \frac{-2x_rK_{T_2}\Omega_{0_2}}{I_{yy}} & \frac{-2x_rK_{T_3}\Omega_{0_3}}{I_{yy}} & \frac{2x_fK_{T_4}\Omega_{0_4}}{I_{yy}} \\ 2\Omega_{0_1}\frac{I_{xx}K_{\tau_1}-I_{xz}K_{T_1}y_f}{I_{xx}I_{zz}-{I_{xz}}^2} & -2\Omega_{0_2}\frac{I_{xx}K_{\tau_2}+I_{xz}K_{T_2}y_r}{I_{xx}I_{zz}-{I_{xz}}^2} & 2\Omega_{0_3}\frac{I_{xx}K_{\tau_3}+I_{xz}K_{T_3}y_r}{I_{xx}I_{zz}-{I_{xz}}^2} & 2\Omega_{0_4}\frac{I_{xx}-K_{\tau_4}+I_{xz}K_{T_4}y_f}{I_{xx}I_{zz}-{I_{xz}}^2} \end{bmatrix}^{-1} \begin{bmatrix} PID_1 \\ PID_2 \\ PID_3 \\ PID_4 \end{bmatrix} \tag{5.23}$$

Altitude Controller

The altitude controller is done with an integrator, a proportional gain and a PID controller. The velocity on the vertical direction is integrated and subtracted from the desired altitude to compute the error. This error is then multiplied by a proportional constant K and added to the difference between the current velocity and the desired velocity. Finally, this value is transmitted to the PID controller that outputs a signal. This process is shown in figure 5.7.

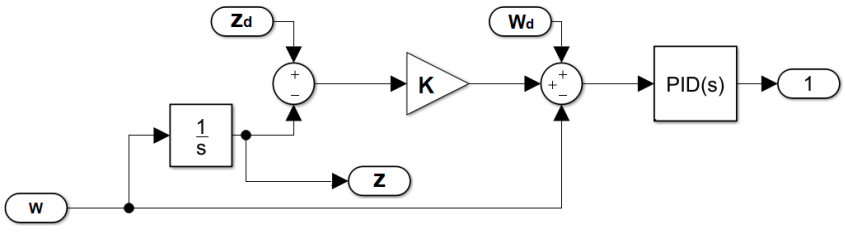

Figure 5.7: Altitude controller

Attitude Controllers - Roll, Pitch and Yaw

The controller for each Euler angle and rate follows a similar process to the one described above. The angle value from the state vector is subtracted to the desired angle and the error is multiplied by a

proportional constant K. This new error is then added to the difference between the desired and the current angular rate, and entered into a PID controller, that outputs a signal, as shown in figure 5.8.

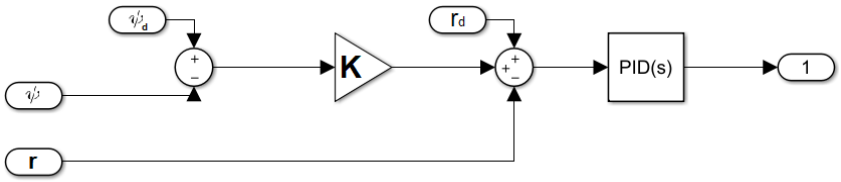

Figure 5.8: Z direction attitude controller

5.2.2 Controller Tuning

In order to achieve a stable model that does not oscillate unnecessarily, yet has a controlled and fast response, the gains of the proportional controllers as well as the ones from the PID controllers must be tuned.

The process of tuning the PID controllers is presented on figure 5.9, where the objective was to achieve minor deviations from the desired state, responding to changes in the latter quickly and with minimal overshoot. These two last objectives conflict with each other, therefore a compromise must be reached.

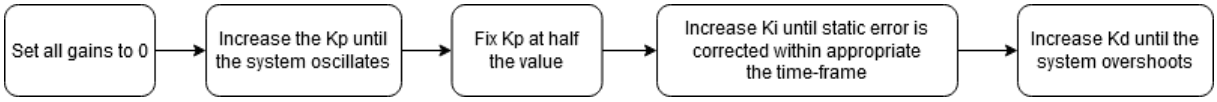

Figure 5.9: PID tuning process

With all the gains set to zero, the proportional gain K_p was increased until the system became unstable and oscillations presented themselves, taking approximately half that value. Afterwards, the integral gain K_I was increased, eliminating the offset to the desired condition with a reasonably fast response, without destabilising the system. Lastly, the derivative gain K_d is increased, affecting the damping oh the system.

Although this process was done manually, tuning the gains until the objectives were reached, there are other popular methods of PID tuning - Simulink® offers the option of autotune. The values defined for the main PID controllers of each block are presented of table 5.4.

Controller	Proportional	Integral	Derivative
Altitude	50	5	1
Roll	5	1	0
Pitch	5	1	1
Yaw	50	2	0

Table 5.4: PID tuning

Once the PID controllers were tuned with rates and axial velocity as inputs, the remaining proportional controllers were tuned with Euler angles and altitude, following an iterative process. The values obtained are presented on table 5.5.

	w	ϕ	θ	ψ
K_P	0.15	7	1	3

Table 5.5: Proportional controller tuning

5.3 Results

The results presented in this section were obtained for configuration one, as it is the one that was built, therefore worthy of comparing with the experimental results presented in the next chapter. During the tuning process, there was a clear decoupling between longitudinal and lateral dynamics. As such, the results of the flight dynamics model will be presented separately for each case. Additionally, with no trajectory tracking or active control for u, v, x and y variables, these will not be presented. Finally, a comparison is made between the results obtained for configuration one, and the ones obtained for configurations two and three, by adjusting the model, maintaining the same gains.

5.3.1 Longitudinal Dynamics

The longitudinal variables are the vertical velocity and position, as well as the pitch angle and rate. Figure 5.10 shows the controller's response to a request of -10m in altitude. The time to reach 90% of the request is about 15 seconds, requiring a rate of -1.5 m/s. The controller performs this request, forcing the velocity back to zero to maintain position. While there is a slight pitch manoeuvre, it is corrected, returning to the initial position. Figure 5.11 presents the response of the same controller to a request of -30m. The time to reach 90% of the request is similar to the one of the previous case, requiring a higher rate - -4m/s. The higher rate is due to a heavier motor actuation, within the saturation limits. In this case the pitch movement is more noticeable, but still stable, as it balances out.

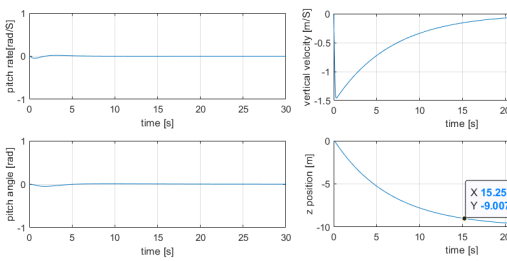

Figure 5.10: Configuration 1 - 10 m altitude request

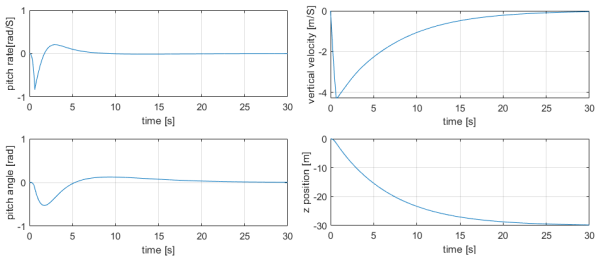

Figure 5.11: Configuration 1 - 30 m altitude request

The same type of analysis can be produced for pitch, requesting the UAV to perform a rotation around the y axis. For a request of 10º, the controller reaches the request within 5 seconds, with a pitch rate over 0.1 rad/s. The vertical velocity remains unchanged, allowing the position to remain constant at 0m,

as seen in figure 5.12. On figure 5.13, the response to a request of 30º is shown, where the same time is required to fulfil the desired attitude. Here, the rate achieved is about 0.3 rad/s, with a slight oscillation on the vertical velocity that is corrected.

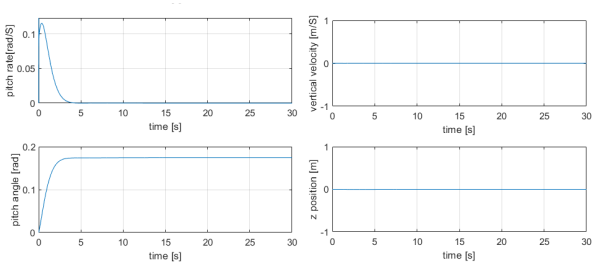

Figure 5.12: Configuration 1 - 10º pitch request

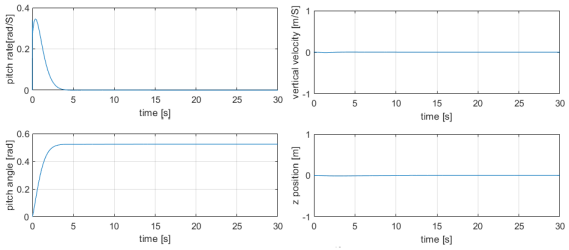

Figure 5.13: Configuration 1 - 30º pitch request

5.3.2 Lateral Dynamics

The variables used in the lateral dynamics are the roll rate and angle as well as the yaw rate and angle. These were excited, as in the longitudinal dynamics, to prove the system is stable and controllable. Figure 5.14 shows the behaviour of the UAV to a request of one degree in roll, where there is a slight overshoot, prior to reaching the desired attitude. Figure 5.15 shows a similar curve, reaching the 3º request within a similar time frame. In this case the roll rate achieved is about 0.2 rad/s, as opposed to the 0.1 achieved in the previous image. In both cases the yaw variation is negligible.

The model presented an unstable behaviour for requested angles over 3º for roll, due to the yaw moment that surfaced with the lateral velocity that is characteristic of this motion, which the torque of the motors couldn't balance with the implemented saturation. From the dynamics presented, either the lateral drag force is being overestimated, by assuming it has the drag coefficient of a cylinder, or the UAV itself can't perform aggressive roll manoeuvres, in which case the motors should be changed into ones with higher torque constant and/or KV to balance the aerodynamic yaw moment.

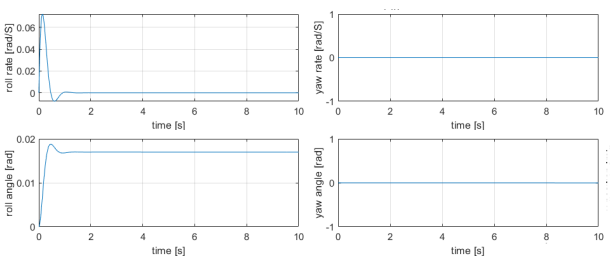

Figure 5.14: Configuration 1 - 1º roll request

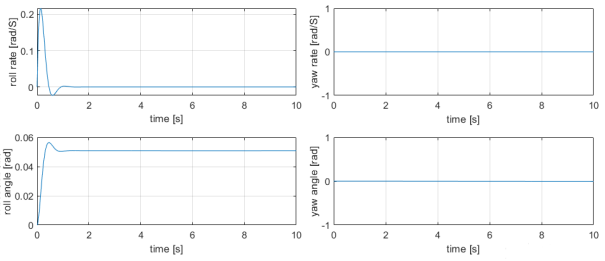

Figure 5.15: Configuration 1 - 3º roll request

Finally, there is the study of the yaw rate and angle. Figure 5.16 presents the behaviour of the system to an excitation of 10º, where the request is fulfilled with five seconds, with no oscillations in roll. The same can be seen on figure 5.17, where the rate achieved is over 0.4, as opposed to the 0.2 of the previous case.

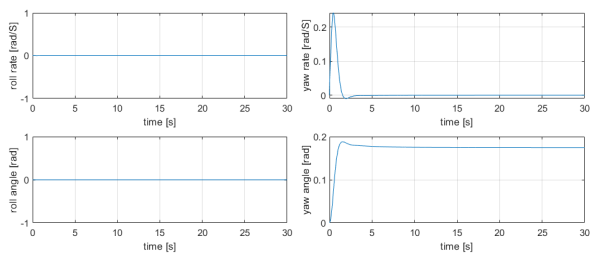

Figure 5.16: Configuration 1 - 10º yaw request

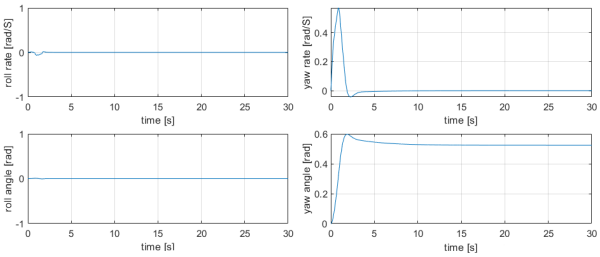

Figure 5.17: Configuration 1 - 30º yaw request

5.3.3 Configuration Comparison

Here a comparison of the behaviour of configurations two and three is displayed against the curves obtained for configuration one. In order to adjust the model for the two latter configurations, their C_{d0} was altered, as well as the moments of inertia and maximum allowed limits of rotation for each configuration. To simplify the analysis, it was assumed that configurations two and three would have the same moments of inertia, disregarding the pusher of configuration two. The values for the moments inertia are presented on table 5.6 [1].

Inertia	Configuration 1	Configuration 2 & 3
I_{xx}	0.62512	0.3539
I_{yy}	0.7109	0.3984
I_{zz}	1.3323	0.7487

Table 5.6: Configuration's moments of inertia

The variation of the moments of inertia is due to differences in structural components in their position, weight and geometry, as well as the shift in position of the motors, combined with their mass variation.

Longitudinal Dynamics

Regarding the longitudinal dynamics, to reach the same altitude configurations two and three require roughly the same time and the same rate - figure 5.18. However, a higher pitch rate is reached prior to stabilization. This difference can be due to a different inertia, as well as motor placement, as the front motors produce less thrust than the rear ones. As for the pitch manoeuvre, no differences can be seen, as displayed in figure 5.19.

Lateral Dynamics

The lateral dynamics will also be compared for both configurations. When regarding roll, the angle is reached within the same time frame, with a similar roll rate and no disturbances in yaw, as presented in figure 5.20. In contrast, figure 5.21 shows that the yaw manoeuvre has a higher rate to reach the desired

[1] The moments of inertia values were calculated with Solidworks, by a third party, the results from BFP were not used. The I_{xz} is assumed to remain constant at 0.013

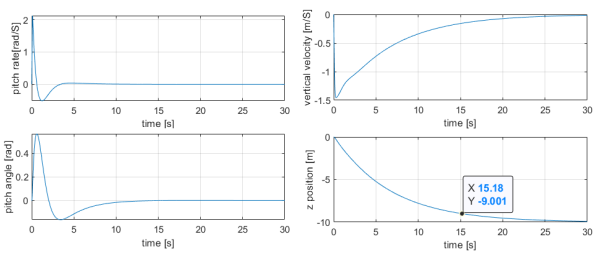

Figure 5.18: Configuration 2 & 3 - 10m altitude

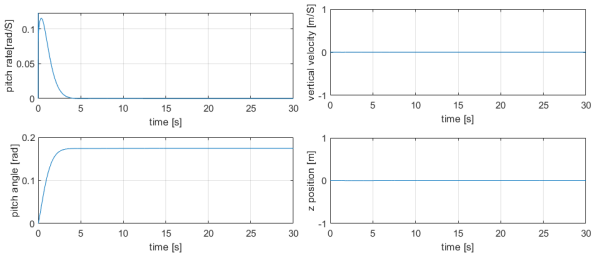

Figure 5.19: Configuration 2 & 3 - 10 º pitch

attitude, while exhibiting close to no overshoot. This is expected due to a lower inertia. Additionally, it features significant roll oscillations that are then stabilized.

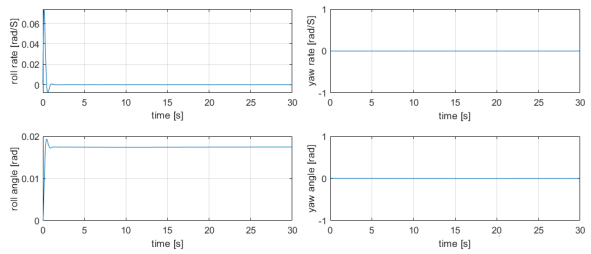

Figure 5.20: Configuration 1 - 1º roll

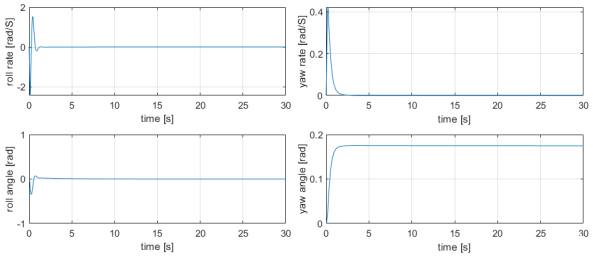

Figure 5.21: Configuration 1 - 10 º yaw

5.4 Tri-rotor Dynamics

In order to produce a fight dynamics model for configuration four, the dynamics equations must be adjusted to account for the different number of rotors, as well as its position.

Since the same structure will be used for this configuration, the aerodynamic forces and moments remain unchanged, leaving only the propulsive forces to adjust. With the loss of one rotor, another degree of freedom must be added to the system. To do so, a rotation of the booms that support the front rotors was added, to balance the moments. The rotation of the rotors around the booms will produce forces in all three components, as seen of figure 5.22.

Assuming both rotors rotate in the same direction, the forces and moments due to rotor actuation are

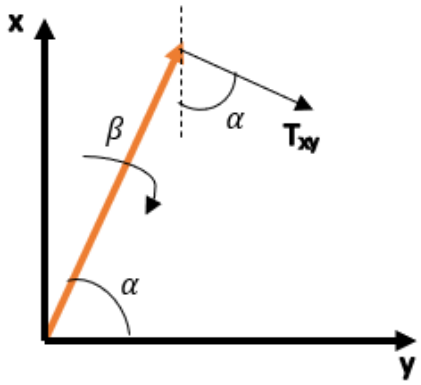

Figure 5.22: Thrust direction due to boom rotation

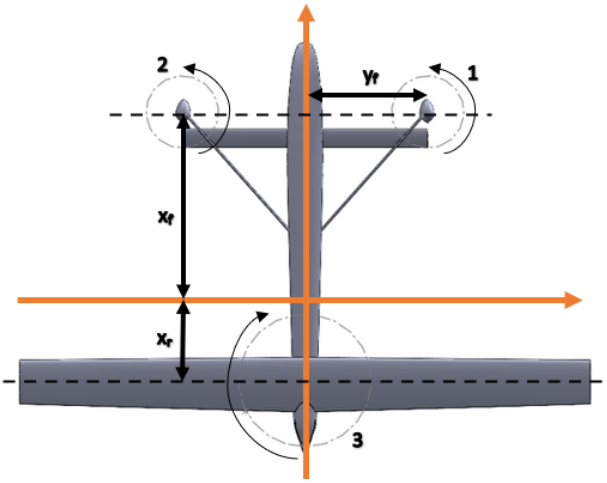

Figure 5.23: Tri-rotor rotor positioning

given by the system of equations below.

$$\begin{cases} F_{x_p} = -K_{T_1}{\Omega_1}^2 \sin\beta\cos\alpha + K_{T_2}{\Omega_2}^2 \sin\beta\cos\alpha \\ F_{y_p} = K_{T_1}{\Omega_1}^2 \sin\beta\sin\alpha + K_{T_2}{\Omega_2}^2 \sin\beta\sin\alpha \\ F_{z_p} = -K_{T_1}{\Omega_1}^2 \cos\beta - K_{T_2}{\Omega_2}^2 \cos\beta - K_{T_3}{\Omega_3}^2 \\ M_{x_p} = y_f(K_{T_2}{\Omega_2}^2 \cos\beta - K_{T_1}{\Omega_1}^2 \cos\beta) + \sin\beta\cos\alpha(K_{\tau_2}{\Omega_2}^2 - K_{\tau_1}{\Omega_1}^2) \\ M_{y_p} = x_f(K_{T_1}{\Omega_1}^2 \cos\beta + K_{T_2}{\Omega_2}^2 \cos\beta) - K_{T_3}{\Omega_3}^2 x_r + \sin\beta\sin\alpha(K_{\tau_1}{\Omega_1}^2 + K_{\tau_2}{\Omega_2}^2) \\ M_{z_p} = \cos\beta[y_f(K_{T_1}{\Omega_1}^2 + K_{T_2}{\Omega_2}^2) + x_f(K_{T_1}{\Omega_1}^2 + K_{T_2}{\Omega_2}^2) - (K_{\tau_1}{\Omega_1}^2 + K_{\tau_2}{\Omega_2}^2)] + K_{\tau_3}{\Omega_3}^2 \end{cases} \tag{5.24}$$

This system of equations was derived following the rotor positioning presented on figure 5.23, where the front rotors are at distance (x_f, y_f) of the centre of gravity and the rear rotor is at $(x_r, 0)$. These distances are the same as the ones presented for configurations two and three, previously presented. Rotors one and two rotate in the negative direction, producing torque upwards, while rotor three rotates in the opposite direction, producing positive torque. With such alterations, the tri-rotor dynamics can be given be derived, linearizing the equations above and adding them to the previously calculated matrices.

Chapter 6

Flight Testing

This chapter describes the flight testing procedure, the data gathering method and the process through which power consumption was estimated for hover condition for configuration one, comparing it with the one from the static bench tests.

6.1 Flight Test Preparations

Prior to the flight tests, several experimental preparations had to take place. From the mechanical point of view, the UAV had to be trimmed, the centre of gravity had to be verified and the inertia values had to be obtained. Additionally, structural tests were performed in the wing and canard to ensure it would endure the desired flight conditions. The avionics had to be tuned, guaranteeing a safe degree of robustness of the controller, by testing the same exact system in a smaller scale UAV. On the propulsion side, all motors were tested with the propellers and ESCs chosen for this configuration.

Mission Plan

Having configuration one fully built and instrumented, with all the required commissioning tasks performed, it could fly in both multicopter mode for VTOL and in fixed-wing mode for forward-flight. However, the transport authorities in Canada require specific bureaucracy to allow a UAV with over 0.25 kg to fly outdoors, which prevented the test of the forward-flight propulsion system within the available timeframe. With this constraint, configuration one was only tested in multicopter mode, since VTOL tests could be performed indoors, leaving the experimental testing of the forward-flight propulsion system do be carried out later on.

Pre-test assembly

Due to the large scale of the UAV, configuration one was transported disassembled to the testing facility and assembled on sight. The VTOL motors had already been secured to motor mounts fixed to the booms, and the pusher motor was integrated at the end of the fuselage. The ESCs were inserted in the

wing, with all cabling passing through the booms. Once all connections were made and the propellers attached, only the battery was missing to complete the propulsion system of the UAV. Figure 6.1 shows configuration one after the assembly process.

Figure 6.1: Configuration 1

Configuration one weighs 7.2 kg, 0.2 kg over the initial MTOM. All the fixed-wing actuators were set to zero degrees and the pusher propeller aligned with the rudder to avoid interference during the VTOL flights.

6.2 Flight Tests

In order to ensure safety of the crew, the first test performed was a hover test, confirming all rotors were rotating in the correct direction, that the centre of gravity was placed at the design position and that there are no severe structural oscillations. This flight lasted 30 seconds, with positive results, allowing the remaining tests to be performed.

The second flight test was performed with the goal of ensuring proper tuning of the controller with small inputs in roll, pitch and yaw. These tests were followed by tests where doublets were input into the UAV in the three directions to observe its response. Figure 6.2 presents the UAV performing roll, pitch and yaw manoeuvres.

(a) Roll manoeuvre

(b) Pitch manoeuvre

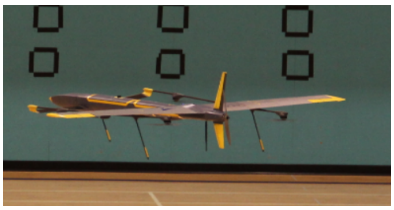

(c) Yaw manoeuvre

Figure 6.2: In-flight manoeuvres

With all the previous tests guaranteeing a high level of robustness of the controller, two tests in altitude

control mode were performed, discharging one full battery each.

6.2.1 Hover Power Consumption

The two last tests were used to assess the UAV's performance, since they had a longer duration, which resulted in an abundance of data to analyze during hover condition. However, the avionics part that had been responsible for recording the power allocated to each motor was malfunctioning and was removed. Lacking this device, the power consumption of each motor was unknown and had to be estimated from the battery consumption. Table 6.1 shows the battery consumed by the motors during each flight

Flight Test	Battery Consumption [Ah]	Avionics Consumption [Ah]	Motor Consumption [Ah]	Duration [s]
1	5.29	0.21	5.08	382
2	6.96	0.7	6.26	466

Table 6.1: Flight test power consumption

Knowing the total capacity consumed by the motors and the duration of the flight, the average current passing to each motor can be calculated, as presented on equation 6.1.

$$\frac{Capacity\ \ Consumption}{Flight\ \ Duration} = 4 \times Motor\ \ Current \Rightarrow Motor\ \ Current = \frac{Capacity\ \ Consumption}{4 \times Flight\ \ Duration} \quad (6.1)$$

The average current was multiplied by the average voltage per test to calculate the power consumption for each flight test.

Flight Test	Current [A]	Voltage [V]	Power [W]	Total Power [W]
1	11.97	23.81	285.0	1140.0
2	12.09	23.73	286.9	1147.6

Table 6.2: Hover performance

Comparing to the results obtained in the static test bench, these values are significantly higher than the expected, exceeding the estimations in 21.7% and 22.5% for flights one and two, respectively. While significant, the discrepancy can be explained by an accumulation of factors:

- The flight tests include manoeuvres where the rotors consume over hover power
- The UAV was slightly overweight
- The power was calculated with average voltage, that fluctuated with battery discharge
- There was significant aerodynamic interference from ground effect during take-off and landing
- There was visible structural bending in the structure, deviating the thrust vectors from the ideal vertical direction
- Presence of drag from the structures

- Rotor-wing interference - rear rotors
- Overestimation of propeller performance
- Differences in the atmospheric conditions

When comparing the average throttle setting at which the motors were operating to the expected throttle setting there is also a discrepancy. Figure 6.3 presents the throttle over time for flight two, where the average is around 76%.

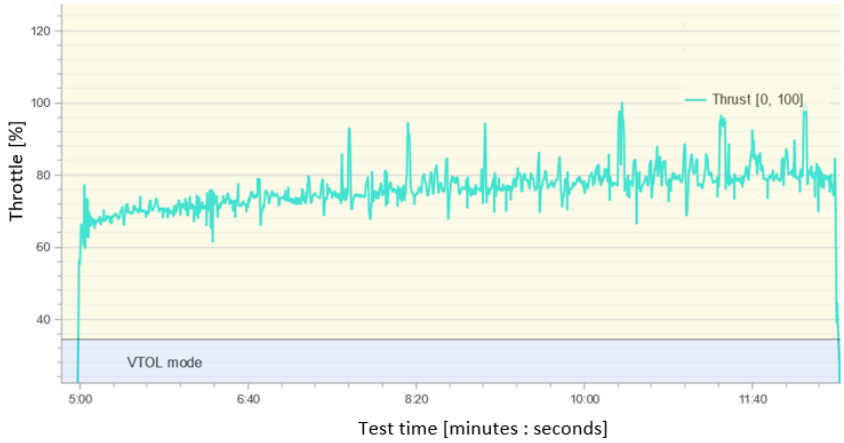

Figure 6.3: Average throttle

The estimated throttle for hover from the static tests was 71.55% , 4.45% lower than the setting required during the flight tests. This difference can be partially explained by the 3% added mass.
Regarding thrust, the 76% throttle setting can be matched to 78N of force which represent a hover condition for a 7.95 kg UAV. The extra thrust can be explained with the constant motor actuation to perform manoeuvres [1].

[1] Assuming a constant ESC calibration between static bench and hover tests

Chapter 7

Conclusions

This chapter presents a review of the work done so far, pointing out the achievements and hurdles encountered during the research. It compares the models used with the experimental data to evaluate their validity and accuracy, indicating which yielded the best results. Finally, the next steps in this research are enumerated, highlighting the major points and their significance to the project.

7.1 Summary

Under the supervision of DRDC, CfAR and Quaterinon Aerospace, the development of a VTOL UAV to detect submarines through their magnetic signature is taking place. This research has presented the sizing of the propulsion system of four scaled down eVTOL UAV prototypes with the aim of validating the sizing and design models, as well as ensuring the full scale UAV has the most adequate configuration for the mission.
The mission profile can be see in figure 7.1, where there are two VTOL segments, two transition segments and one forward-flight segment that may include both cruise and dash conditions.

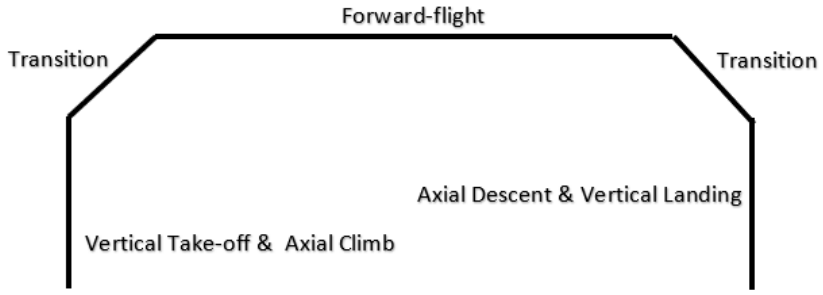

Figure 7.1: Mission profile

The importance of a mission as such is the ability to take-off and land in ships, by use of the VTOL system and then transitioning to forward-flight in order to detect and follow the intended targets. The evaluation criteria for the developed configurations became mission performance - being able to complete the mission efficiently and with the least required mass.

The four configurations chosen follow a logical path from the basic symmetric quadrotor to a vectored-thrust tri-rotor configuration, that was the preliminary propulsion system architecture chosen for the full scale UAV. Figure 7.2 shows the evolution of configurations one to four.

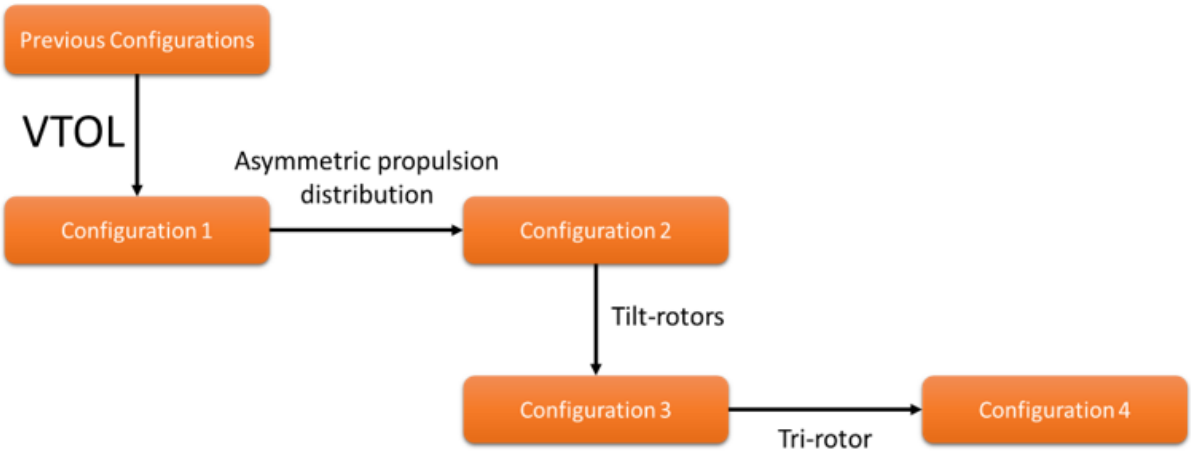

Figure 7.2: Configuration evolution

Configuration one adds a VTOL system to the previous UAVs developed for the mission, featuring a pusher to complete the lift-and-cruise architecture; comparatively, configuration two has the same architecture, but an asymmetric thrust distribution, with the rear rotors producing 80% of the thrust required during VTOL. On the other hand, configuration three has the same VTOL system of configuration two, but has a vectored-thrust architecture, tilting the rear rotors for forward flight. This configuration also features retractable front rotors to have a higher L/D during cruise condition. Finally, configuration four has the same features as configuration three - retractable booms, tilting rear rotor, having a tri-rotor VTOL system instead of a quadrotor.

The VTOL system selection of all configurations was conducted with experimental data from manufacturer websites, comparing it with the results of a vortex theory model for validation. The propulsion system selection for forward-flight of configurations one and two was performed with data from propeller manufacturers, choosing a motor that fulfils the power required by the propeller. Finally, configurations three and four were sized with the vortex theory model, by adjusting the required parameters.

Having all configurations sized, their performance was assessed, studying total installed power as well as power available for forward flight, the total mass of the system, and its energy requirements. Regarding installed power, configuration four performs the mission with the least excess power, having over 73% available for forward flight, while configuration two has the most installed power combined with the least available for forward-flight due to its lift-and-cruise architecture. As for power consumption, configuration four consumes the least power during hover condition - 91.6% relative to configuration one, whereas the VTOL system of configurations two and three consume the most, with 102.8% relative to the same configuration. While significant, cruise condition is likely to determine the overall energy efficiency of the system, since it is the longest mission segment. In cruise, configurations three and four are the most efficient, with 97 and 97.5% of the power of configuration one, while configuration two has a penalty of over 20%. The vectored-thrust configurations perform better in cruise, despite having a forward-flight

system sized for VTOL, due to having a higher L/D, when compared to the lift-and-cruise configurations. When evaluating mass, configurations three and four stand out, by having both least total energy requirements and the lightest component mass. Spending the mass difference in battery could result in doubling the cruise range of configuration four, increasing it in over 15Km for configuration three. These results were confirmed through static thrust tests, validating the models used thus far.

The increased performance of configurations three and four was hindered by having partially covered rotors, requiring a minimum distance between surfaces to achieve a satisfactory net force. With both the CFD simulations and the experimental results, the asymptotic behaviour of the curves was proved, concluding that for the given cases there is a minimum relative required distance of half a radius, having a penalty of 1% in total mass - including battery for one mission and all components- for a distance of 75% of the propeller radius; that still makes them the lightest, yet not the most energetically efficient.

Finally, a dynamic model was developed for configurations one through three, where it was concluded that all simulated configurations are controllable and stable, with close to no differences in behaviour for the same desired attitude. This model gave another degree of confidence to proceed with the flight tests that were performed shortly after.

From the flight test data it was concluded that the system consumed significantly - 20% - more power than estimated from static tests. Although this discrepancy is considerable, it can be explained through the approximations made when disregarding the manoeuvres done in-flight and the added power they required.

7.2 Achievements

The most significant achievement of this research, thus far, is undoubtedly the progress from starting with no definition of the UAV's propulsion system at the outset, to seeing the project hover. Actually, regardless of the lack of fixed-wing flight tests, the propulsion system of configuration one was able to successfully perform hover flight tests by use of its VTOL system, in spite of some structural flaws, ensuring the correct sizing of the system. This, however, does not encompass all the accomplishments evident in the process which lead to the eventual success.

As evidenced in this document, the initial set of objectives have been met; from sizing the propulsion system of all four configurations, to confirming that the target configuration better performs the stated mission in almost every metric.

With regard to the used models, the vortex theory model has been validated with marginal errors when compared to experimental tests. The CFD simulations on rotor coverage were similarly validated against experimental data confirming the asymptotic tendency of the net force curve as a function of the relative distance between surfaces. Furthermore, the experimental tests on rotor coverage can set a standard for determining the minimum relative distance between rotor and wing for a given covered area. This, in and of itself, is an achievement.

Other accomplishments include the development of a flight dynamics model, tuning the controller to respond correctly to step inputs in all its rates for all the quadrotor configurations.

7.3 Future Work

First and foremost, this research lacks the experimental evaluation of the chosen forward-flight propulsion system. As mentioned before, there are complicated steps that must be taken in order to fly a UAV outdoors in Canada, which is required to test the pusher rotor in fixed-wing mode. While the bureaucracy couldn't be completed within the time frame of this thesis, the UAV is ready to fly, and given permission from TA, the performance of the pusher rotor can be ascertained.

Secondly, the purchasing of the rear motor of configuration four should take place, in order to have experimental data to further validate it as the best choice for the mission.

Additionally, the evaluation of the magnetic signature of the VTOL system, comparing it against the previous configurations should take place, ensuring it doesn't compromise the purpose of the UAV. This step can take place as soon as the Qu-spin magnetic sensor is available, as the UAV was manufactured already accounting its mass and volume.

The quantification of the magnetic interference of the VTOL system of configuration one should be followed by the development of the remaining configurations, evaluating their performance and comparing it with the base configuration. This step will confirm the conclusions presented so far, ensuring the vectored-thrust tri-rotor configuration is the best for the chosen mission.

The next step requires the continuity of the project into the future, extending the partnership between the institutions to develop the full scale propulsion system. Since the full scale prototype weighs 25 kg, investigation into other types of propulsion, while maintaining the defined architecture should take place.

Bibliography

[1] J. Keane and S. Carr. A Brief History of Early Unmanned Aircraft. *Johns Hopkins Apl Technical Digest*, 32:558–571, Dec. 2013.

[2] J. G. Leishman. The breguet-richet quad-rotor helicopter of 1907. *Vertiflite*, 47(3):58–60, 2002.

[3] S. N. Ghazbi, Y. Aghli, M. Alimohammadi, and A. A. Akbari. QUADROTORS UNMANNED AERIAL VEHICLES: A REVIEW. *International Journal on Smart Sensing and Intelligent Systems*, 9(1), Mar. 2016. ISSN , 1178-5608. doi: 10.21307/ijssis-2017-872. URL `https://doi.org/`.

[4] G. Cai, J. Dias, and L. Seneviratne. A Survey of Small-Scale Unmanned Aerial Vehicles: Recent Advances and Future Development Trends. *Unmanned Systems*, 02:175–199, Apr. 2014. doi: 10.1142/S2301385014300017.

[5] A. Saeed, A. Bani Younes, S. Islam, J. Dias, L. Seneviratne, and G. Cai. A Review on the Platform Design, Dynamic Modeling and Control of Hybrid UAVs. June 2015. doi: 10.1109/ICUAS.2015.7152365.

[6] M. Boon, A. Drijfhout, and S. Tesfamichael. Comparison of a Fixed-Wing and Multi-Rotor Uav for Environmental Mapping Applications: a Case Study. 2017. doi: 10.5194/ISPRS-ARCHIVES-XLII-2-W6-47-2017.

[7] D. Finger. Comparative Performance and Benefit Assessment of VTOL and CTOL UAVs. Sept. 2016.

[8] O. Gur and A. Rosen. Optimizing Electric Propulsion Systems for UAVs. Sept. 2008. ISBN 9781600869822. doi: 10.2514/6.2008-5916.

[9] P. Stahl, C. Roessler, and M. Hornung. Modelling and Performance Impact of High Power/High Energy Battery Hybrids on Fixed-Wing eVTOL UAV. In *AIAA Scitech 2020 Forum*. American Institute of Aeronautics and Astronautics, Jan. 2020. doi: 10.2514/6.2020-0260. URL `https://arc.aiaa.org/doi/abs/10.2514/6.2020-0260`.

[10] D. F. Finger, C. Braun, and C. Bil. The impact of electric propulsion on the performance of VTOL UAVs. *66. Deutscher Luft-und Raumfahrtkongress DLRK 2017*, 2017.

[11] W. Ng and A. Datta. Development of Propulsion System Models for Electric-VTOL Aircraft. In *2018 AIAA Aerospace Sciences Meeting*. American Institute of Aeronautics and Astronautics, Jan. 2018. doi: 10.2514/6.2018-1750. URL https://arc.aiaa.org/doi/abs/10.2514/6.2018-1750.

[12] Arexy Monterroso. *Preliminary sizing, flight test, and performance analysis of small tri-rotor VTOL and fixed-wing UAV*. PhD thesis, San Diego State University, 2018. URL https://digitallibrary.sdsu.edu/islandora/object/sdsu%3A22098.

[13] Watcharapol Saengphet and Chalothorn Thumthae. Conceptual Design of Fixed Wing-VTOL UAV for AED transport. In *The 7th TSME International Conference on Mechanical Engineering*, 2016. URL https://www.researchgate.net/publication/312173247_Conceptual_Design_of_Fixed_Wing-VTOL_UAV_for_AED_transport.

[14] A. Bacchini and E. Cestino. Electric VTOL Configurations Comparison. *Aerospace*, 6(3):26, Mar. 2019. doi: 10.3390/aerospace6030026. URL https://www.mdpi.com/2226-4310/6/3/26.

[15] Mohamed Nadir Boukoberine, Zhibin Zhou, and Mohamed Benbouzid. A Critical Review on Unmanned Aerial Vehicles Power Supply and Energy Management: Solutions, Strategies, and Prospects. 255(113823), Dec. 2019. URL https://www.researchgate.net/publication/335564429_A_Critical_Review_on_Unmanned_Aerial_Vehicles_Power_Supply_and_Energy_Management_Solutions_Strategies_and_Prospects.

[16] Joseph Conroy, A. Kehlenbeck, and J. Sean Humbert. Characterization of Small DC Brushed and Brushless Motors. In *Proceedings of SPIE - The International Society for Optical Engineering*, 2014. URL https://www.semanticscholar.org/paper/Characterization-of-Small-DC-Brushed-and-Brushless-Harrington-Kroninger/d2f1abadee4224f30ec2f5fdc6692312f3fcd40f.

[17] D. Gabriel, J. Meyer, and F. du Plessis. Brushless DC motor characterisation and selection for a fixed wing UAV. pages 1–6, Sept. 2011. ISBN 9781612849928. doi: 10.1109/AFRCON.2011.6072087.

[18] B. Bilgin, J. Liang, M. Terzic, J. Dong, R. Rodriguez, E. Trickett, and A. Emadi. Modeling and Analysis of Electric Motors: State-of-the-Art Review. *IEEE Transactions on Transportation Electrification*, PP:1–1, July 2019. doi: 10.1109/TTE.2019.2931123.

[19] G. Kuiper. New developments and propeller design. *Journal of Hydrodynamics, Ser. B*, 22:7–16, Oct. 2010. doi: 10.1016/S1001-6058(09)60161-X.

[20] G. Hattenberger. Figure 11: Typical propeller efficiency curves as a function of advance... URL https://www.researchgate.net/figure/Typical-propeller-efficiency-curves-as-a-function-of-advance-ratio-J_fig3_281946347.

[21] O. Gur and A. Rosen. Propeller Performance at Low Advance Ratio. *Journal of Aircraft*, 42(2): 435–441, 2005. doi: 10.2514/1.6564. URL https://doi.org/10.2514/1.6564.

[22] J. Xu, W. Song, X. Yang, and H. Nie. Aerodynamic Performance of Variable-Pitch Propellers for High-Altitude UAVs. *IOP Conference Series: Materials Science and Engineering*, 686:012019, Dec. 2019. doi: 10.1088/1757-899X/686/1/012019.

[23] I. McAndrew, E. Navarro, and K. Witcher. Propeller Design Requirements for Quadcopters Utilizing Variable Pitch Propellers. *International Journal of Materials, Mechanics and Manufacturing*, 6(1): 51–56, Feb. 2018. doi: https://doi.org/ijmmm.2018.6.1.346. URL https://commons.erau.edu/publication/754.

[24] S. Wang, S. Zhang, and S. Ma. An Energy Efficiency Optimization Method for Fixed Pitch Propeller Electric Aircraft Propulsion Systems. *IEEE Access*, 7:159986–159993, 2019. ISSN 2169-3536. doi: 10.1109/ACCESS.2019.2950453.

[25] LUIS COMENDADOR. Propeller Thrust | Principle of flight, Apr. 2020. URL https://flightacademy.info/propeller-thrust.

[26] Q. Wald. The aerodynamics of propellers. *Progress in Aerospace Sciences*, 42:85–128, Feb. 2006. doi: 10.1016/j.paerosci.2006.04.001.

[27] R. Modarres. *Ideal Optimum Performance of Propellers, Lifting Rotors and Wind Turbines*. PhD thesis, Washington University in St. Louis, 2013. URL https://www.semanticscholar.org/paper/Ideal-Optimum-Performance-of-Propellers%2C-Lifting-Modarres/7e66a591b84b21bb23f2482e2c1254b2af90a34d.

[28] B. McKay. Ideal optimization of counterrotating propellers. In *24th Joint Propulsion Conference*, July 1988. URL https://arc.aiaa.org/doi/abs/10.2514/6.1988-2801.

[29] R. MacNeill and D. Verstraete. Blade element momentum theory extended to model low Reynolds number propeller performance. *The Aeronautical Journal*, 121(1240):835–857, 2017.

[30] H. A. Madsen, T. J. Larsen, G. R. Pirrung, A. Li, and F. Zahle. Implementation of the blade element momentum model on a polar grid and its aeroelastic load impact. *Wind Energy Science*, 5(1):1–27, Jan. 2020. ISSN 2366-7443. doi: https://doi.org/10.5194/wes-5-1-2020. URL https://wes.copernicus.org/articles/5/1/2020/.

[31] V. Dehouck, M. Lateb, J. Sacheau, and H. Fellouah. Application of the Blade Element Momentum Theory to Design Horizontal Axis Wind Turbine Blades. *Journal of Solar Energy Engineering*, 140: 014501–9, Sept. 2017. doi: 10.1115/1.4038046.

[32] J. Chattot. OPTIMIZATION OF PROPELLERS USING HELICOIDAL VORTEX MODEL. Jan. 2003. ISSN 978-981-238-317-4. doi: 10.1142/9789812796837_0022.

[33] L. K. Chang and J. P. Sullivan. Optimization of Propeller Blade Twist by an Analytical Method. *AIAA Journal*, 22(2):252–255, Feb. 1984. ISSN 0001-1452. doi: 10.2514/3.48441. URL https://arc.aiaa.org/doi/10.2514/3.48441.

[34] M. H. Rizk and W.-H. Jou. Propeller design by optimization. *AIAA Journal*, 24(9):1554–1556, 1986. ISSN 0001-1452. doi: 10.2514/3.9479. URL https://doi.org/10.2514/3.9479.

[35] W. F. Phillips and D. O. Snyder. Modern Adaptation of Prandtl's Classic Lifting-Line Theory. *Journal of Aircraft*, 37(4):662–670, 2000. doi: 10.2514/2.2649. URL https://doi.org/10.2514/2.2649.

[36] R. A. Eppler and M. Hepperle. A Procedure for Propeller Design by Inverse Methods, 2003. URL /paper/A-Procedure-for-Propeller-Design-by-Inverse-Methods-Eppler-Hepperle/1af1328770f8b310d1b2038395e198c67d09468d.

[37] S. Albert, P. Epple, B. Willinger, and A. Delgado. High Efficiency Propeller Design Based on the Betz Minimum Induced Loss Condition and CFD Validation on an APC 8 in Propeller. volume 7, Nov. 2013. doi: 10.1115/IMECE2013-64382.

[38] S. Goldstein and L. Prandtl. On the vortex theory of screw propellers. *Proceedings of the Royal Society of London. Series A, Containing Papers of a Mathematical and Physical Character*, 123(792):440–465, Apr. 1929. doi: 10.1098/rspa.1929.0078. URL https://royalsocietypublishing.org/doi/10.1098/rspa.1929.0078.

[39] S. Rashahmadi, M. Abbaszadeh, S. Hoseyni, and R. Alizadeh. Design of a constant chord single-rotating propeller using lock and goldstein techniques. 56:1585–1589, Jan. 2011.

[40] L. Piancastelli, A. Castagnoli, L. Frizziero, G. Donnici, and S. Pica. Direct comparison of fsi optimized theodorsen and larrabee propellers. 10:7250–7258, Jan. 2015.

[41] E. Larrabee and Susan French. PROPELLER DESIGIN AND ANALYSIS FOR PEDAL DRIVEN AND OTHER ODD AIRCRAFT. 7(2):49–65, 1981. URL https://journals.sfu.ca/ts/index.php/ts/article/view/950.

[42] E. Eugene Larrabee and S. E. French. Minimum induced loss windmills and propellers. *Journal of Wind Engineering and Industrial Aerodynamics*, 15(1):317–327, Dec. 1983. ISSN 0167-6105. doi: 10.1016/0167-6105(83)90201-5. URL http://www.sciencedirect.com/science/article/pii/0167610583902015.

[43] F. Dominguez, J.-L. Achard, J. Zanette, and C. Corre. Fast power output prediction for a single row of ducted cross-flow water turbines using a BEM-RANS approach. *Renewable Energy*, 89:658–670, Apr. 2016. ISSN 0960-1481. doi: 10.1016/j.renene.2015.12.042. URL http://www.sciencedirect.com/science/article/pii/S0960148115305462.

[44] M. Tabib, M. S. Siddiqui, A. Rasheed, and T. Kvamsdal. Industrial scale turbine and associated wake development -comparison of RANS based Actuator Line Vs Sliding Mesh Interface Vs Multiple Reference Frame method. *Energy Procedia*, 137:487–496, Oct. 2017. ISSN 1876-6102.

doi: 10.1016/j.egypro.2017.10.377. URL http://www.sciencedirect.com/science/article/pii/S1876610217353602.

[45] P. Dewi, G. Hadi, M. Kusnaedi, A. Budiyarto, and A. Budiyono. Design of Separate Lift and Thrust Hybrid Unmanned Aerial Vehicle. Technical report, Jan. 2016.

[46] Jean-Mathieu Gagnon and Claire Deschênes. Numerical Simulation with Flow Feature Extraction of a Propeller Turbine - Unsteady Rotor-Stator Interaction. In *Thirteenth International Conference on Computational Methods and Experimental Measurements*, 2007. URL https://www.researchgate.net/publication/235007088_Numerical_Simulation_with_Flow_Feature_Extraction_of_a_Propeller_Turbine_-_Unsteady_Rotor-Stator_Interaction.

[47] M. Chen and J. P. Hubner. Experimental Investigation of Wing-on-Rotor Effect at Low Disk Loading and Reynolds Number. *Journal of Aircraft*, 0(0):1–10, 2020. doi: 10.2514/1.C035763. URL https://doi.org/10.2514/1.C035763.

[48] V. Becerra. Autonomous Control of Unmanned Aerial Vehicles. *Electronics*, 8:452, Apr. 2019. doi: 10.3390/electronics8040452.

[49] Q. Quan. *Introduction to Multicopter Design and Control*. June 2017. ISBN 9789811033810. doi: 10.1007/978-981-10-3382-7.

[50] B. Emran and H. Najjaran. A review of quadrotor: An underactuated mechanical system. *Annual Reviews in Control*, 46, Oct. 2018. doi: 10.1016/j.arcontrol.2018.10.009.

[51] R. Amin, L. Aijun, and S. Band. A Review of Quadrotor UAV: Control Methodologies and Performance Evaluation. *International Journal of Automation and Control*, 10, Dec. 2015. doi: 10.1504/IJAAC.2016.076453.

[52] G. Szafranski and R. Czyba. Different approaches of PID control UAV type quadrotor. 2011.

[53] A. Zulu and S. John. A Review of Control Algorithms for Autonomous Quadrotors. *Open Journal of Applied Sciences*, 04:547–556, Jan. 2014. doi: 10.4236/ojapps.2014.414053.

[54] A. Salih, M. Moghavvemi, M. Haf, and K. Gaeid. Flight PID Controller Design for a UAV Quadrotor. *Scientific research and essays*, 5:3660–3667., Dec. 2010.

[55] S. Khatoon, M. Shahid, I. Nasiruddin, and H. Chaudhary. Dynamic modeling and stabilization of quadrotor using PID controller. pages 746–750, Sept. 2014. doi: 10.1109/ICACCI.2014.6968383.

[56] M. Eatemadi. Mathematical Dynamics , Kinematics Modeling and PID Equation Controller of QuadCopter, 2019. URL /paper/Mathematical-Dynamics-%2C-Kinematics-Modeling-and-PID-Eatemadi/ffd229130cb47b35fb9e0a04d54433556cdfda90.

[57] P. Wang, Z. Man, Z. Cao, J. Zheng, and Y. Zhao. Dynamics modelling and linear control of quadcopter. In *2016 International Conference on Advanced Mechatronic Systems (ICAMechS)*, pages 498–503, Nov. 2016. doi: 10.1109/ICAMechS.2016.7813499. ISSN: 2325-0690.

[58] K. Oner, E. Cetinsoy, E. Sirimoglu, C. Hancer, T. Ayken, and M. Unel. LQR and SMC Stabilization of a New Unmanned Aerial Vehicle. *Proc.Of the 2009 World Academy of Science, Engineering and Technology*, 58, July 2011.

[59] F. Lescher, J. Zhao, and P. Borne. Robust gain scheduling controller for pitch regulated variable speed wind turbine. *Studies in Informatics and Control*, 14, Jan. 2006.

[60] H. Mo and G. Farid. Nonlinear and Adaptive Intelligent Control Techniques for Quadrotor UAV – A Survey. *Asian Journal of Control*, 21, Apr. 2017. doi: 10.1002/asjc.1758.

[61] T. Başar and P. Bernhard. *H-Infinity Optimal Control and Related Minimax Design Problems: A Dynamic Game Approach*. Springer Science & Business Media, Jan. 2008. ISBN 9780817647568. Google-Books-ID: uUexRFa8_q8C.

[62] P. P. Khargonekar, I. R. Petersen, and K. Zhou. Robust stabilization of uncertain linear systems: quadratic stabilizability and H/sup infinity / control theory. *IEEE Transactions on Automatic Control*, 35(3):356–361, Mar. 1990. ISSN 1558-2523. doi: 10.1109/9.50357.

[63] M. Hertneck, J. Köhler, S. Trimpe, and F. Allgöwer. Learning an Approximate Model Predictive Controller With Guarantees. *IEEE Control Systems Letters*, 2(3):543–548, July 2018. ISSN 2475-1456. doi: 10.1109/LCSYS.2018.2843682.

[64] D. Thiele. Robust adaptive model predictive controller with tuning to compensate for model mismatch, May 2012. URL `https://patents.google.com/patent/US8185217B2/en`.

[65] Z. T. Dydek, A. M. Annaswamy, and E. Lavretsky. Adaptive Control of Quadrotor UAVs: A Design Trade Study With Flight Evaluations. *IEEE Transactions on Control Systems Technology*, 21(4): 1400–1406, July 2013. ISSN 1558-0865. doi: 10.1109/TCST.2012.2200104.

[66] P. Mattavelli, L. Rossetto, G. Spiazzi, and P. Tenti. General-purpose sliding-mode controller for DC/DC converter applications. In *Proceedings of IEEE Power Electronics Specialist Conference - PESC '93*, pages 609–615, June 1993. doi: 10.1109/PESC.1993.471989.

[67] A. SULFICAR. *MODELING, SIMULATION AND COMPLETE CONTROL OF A QUADCOPTER*. PhD Thesis, NATIONAL INSTITUTE OF TECHNOLOGY KARNATAKA SURATHKAL, 2017.

[68] I. Dikmen, A. Arisoy, and H. Temeltas. Attitude control of a quadrotor. pages 722–727, July 2009. doi: 10.1109/RAST.2009.5158286.

[69] B. Erginer and E. Altug. Modeling and PD control of a quadrotor VTOL vehicle. pages 894–899, July 2007. doi: 10.1109/IVS.2007.4290230.

[70] H. Zhang, K. Zhang, Y. Cai, and J. Han. Adaptive Fuzzy Fault-Tolerant Tracking Control for Partially Unknown Systems With Actuator Faults via Integral Reinforcement Learning Method. *IEEE Transactions on Fuzzy Systems*, 27(10):1986–1998, Oct. 2019. ISSN 1941-0034. doi: 10.1109/TFUZZ.2019.2893211.

[71] P. Bouffard, A. Aswani, and C. Tomlin. Learning-based model predictive control on a quadrotor: Onboard implementation and experimental results. In *2012 IEEE International Conference on Robotics and Automation*, pages 279–284, May 2012. doi: 10.1109/ICRA.2012.6225035. ISSN: 1050-4729.

[72] Lebao Li, Lingling Sun, and Jie Jin. Survey of advances in control algorithms of quadrotor unmanned aerial vehicle. In *2015 IEEE 16th International Conference on Communication Technology (ICCT)*, pages 107–111, Oct. 2015. doi: 10.1109/ICCT.2015.7399803.

[73] J. Lieh, E. Spahr, A. Behbahani, and J. Hoying. Design of Hybrid Propulsion Systems for Unmanned Aerial Vehicles. July 2011. ISBN 9781600869495. doi: 10.2514/6.2011-6146.

[74] M. Jaeger and D. Adair. Conceptual Design of a High-Endurance Hybrid Electric Unmanned Aerial Vehicle. Aug. 2016.

[75] D. P. Thipphavong, R. Apaza, B. Barmore, V. Battiste, B. Burian, Q. Dao, M. Feary, S. Go, K. H. Goodrich, J. Homola, H. R. Idris, P. H. Kopardekar, J. B. Lachter, N. A. Neogi, H. K. Ng, R. M. Oseguera-Lohr, M. D. Patterson, and S. A. Verma. Urban Air Mobility Airspace Integration Concepts and Considerations. In *2018 Aviation Technology, Integration, and Operations Conference*. American Institute of Aeronautics and Astronautics, June 2018. doi: 10.2514/6.2018-3676. URL https://arc.aiaa.org/doi/abs/10.2514/6.2018-3676.

[76] M. Tyan, N. V. Nguyen, and S. Kim. Comprehensive preliminary sizing/resizing method for a fixed wing – VTOL electric UAV - ScienceDirect. 71:30–41, 2017. URL https://www.sciencedirect.com/science/article/abs/pii/S1270963817300871.

[77] F. FOLE. From da Vinci to the present - A review of airscrew theory for helicopters, propellers, windmills, and engines. In *9th Fluid and PlasmaDynamics Conference*. American Institute of Aeronautics and Astronautics, July 1976. doi: 10.2514/6.1976-367. URL https://arc.aiaa.org/doi/abs/10.2514/6.1976-367.

[78] T. C. Corke. *Design of aircraft*. Prentice Hall Englewood Cliffs, NJ, 2003.

[79] B. Moffitt, T. Bradley, D. Parekh, and D. Mavris. Validation of Vortex Propeller Theory for UAV Design with Uncertainty Analysis. In *46th AIAA Aerospace Sciences Meeting and Exhibit*. American Institute of Aeronautics and Astronautics, Jan. 2008. doi: 10.2514/6.2008-406. URL https://arc.aiaa.org/doi/abs/10.2514/6.2008-406.

[80] W. F. Phillips. *Mechanics of Flight*. John Wiley & Sons, Jan. 2004. ISBN 9780471334583.

[81] W. F. Phillips. Propeller Momentum Theory with Slipstream Rotation. *Journal of Aircraft*, 39(1): 184–187, 2002. doi: 10.2514/2.2914. URL https://doi.org/10.2514/2.2914.

[82] SimScale. What is CFD | What is Computational Fluid Dynamics? URL https://www.simscale.com/docs/simwiki/cfd-computational-fluid-dynamics/what-is-cfd-computational-fluid-dynamics/.

[83] NPD solutions. Computational Fluid Dynamics Overview, 2019. URL https://www.npd-solutions.com/cfd.html.

[84] Franco Concli, Carlo Gorla, Augusto Della Torre, and Gianluca Montenegro. Analysis of the power losses in geared transmissions - measurements and CFD calculations based on open source codes. In *Open Source CFD International Conference*, 2013. URL https://www.researchgate.net/publication/303673133_Analysis_of_the_power_losses_in_geared_transmissions_-_measurements_and_CFD_calculations_based_on_open_source_codes.

[85] R. Franzke, S. Sebben, T. Bark, E. Willeson, and A. Broniewicz. Evaluation of the Multiple Reference Frame Approach for the Modelling of an Axial Cooling Fan. 2019. doi: 10.3390/EN12152934.

[86] E. Dick, J. Vierendeels, S. Serbruyns, and J. Vande Voorde. Performance prediction of centrifugal pumps with CFD-tools. *TASK QUARTERLY*, 5:579–594, Jan. 2001.

[87] J. D. Denton. Some Limitations of Turbomachinery CFD. pages 735–745. American Society of Mechanical Engineers Digital Collection, Dec. 2010. doi: 10.1115/GT2010-22540. URL https://asmedigitalcollection.asme.org/GT/proceedings/GT2010/44021/735/346936.

[88] D. Witteck, D. Micallef, and R. Mailach. Comparison of Transient Blade Row Methods for the CFD Analysis of a High-Pressure Turbine. volume 2, June 2014. doi: 10.1115/GT2014-26043.

[89] J. Mcnaughton, I. Afgan, D. Apsley, S. Rolfo, T. Stallard, and P. Stansby. A simple sliding-mesh interface procedure and its application to the CFD simulation of a tidal-stream turbine. *International Journal for Numerical Methods in Fluids*, 74, Feb. 2014. doi: 10.1002/fld.3849.

[90] R. Steijl and G. Barakos. Sliding mesh algorithm for CFD analysis of helicopter rotor–fuselage aerodynamics. *International Journal for Numerical Methods in Fluids*, 58(5):527–549, 2008. ISSN 1097-0363. doi: https://doi.org/10.1002/fld.1757. URL https://onlinelibrary.wiley.com/doi/abs/10.1002/fld.1757.

[91] R. Izmaylov, H. Lopulalan, and G. Norimarna. Unsteady Flow Modeling Using Transient Rotor–Stator Interface. volume 6, June 2013. doi: 10.1115/GT2013-95788.

[92] N. Kumar, M. Kiran, and P. Kumar. Design and Analysis of Marine Propeller with Leading Edge Protuberances. *International Journal for Research in Applied Science & Engineering Technology*, 6(X), Oct. 2028. URL https://1library.net/document/yr3pm28y-design-analysis-marine-propeller-leading-edge-protuberances.html.

[93] F. Menter. Zonal Two Equation k-w Turbulence Models For Aerodynamic Flows. In *23rd Fluid Dynamics, Plasmadynamics, and Lasers Conference*, Fluid Dynamics and Co-located Conferences. American Institute of Aeronautics and Astronautics, July 1993. doi: 10.2514/6.1993-2906. URL https://arc.aiaa.org/doi/10.2514/6.1993-2906.

[94] F. R. Menter. Two-equation eddy-viscosity turbulence models for engineering applications. *AIAA Journal*, 32(8):1598–1605, Aug. 1994. ISSN 0001-1452. doi: 10.2514/3.12149. URL https://arc.aiaa.org/doi/10.2514/3.12149.

[95] F. Moukalled, L. Mangani, and M. Darwish. The Finite Volume Method. In F. Moukalled, L. Mangani, and M. Darwish, editors, *The Finite Volume Method in Computational Fluid Dynamics: An Advanced Introduction with OpenFOAM® and Matlab*, Fluid Mechanics and Its Applications, pages 103–135. Springer International Publishing, Cham, 2016. ISBN 9783319168746. doi: 10.1007/978-3-319-16874-6_5. URL https://doi.org/10.1007/978-3-319-16874-6_5.

[96] T. Kringeland. *Modelling and Control of a Vertical Take-Off and Landing Fixed-Wing Unmanned Aerial Vehicle*. PhD thesis, UNIVERSITY OF OSLO, Oslo, 2019.

[97] E. Balasubramanian and R. Vasantharaj. Dynamic Modeling and Control of Quad Rotor. 2013. URL /paper/Dynamic-Modeling-and-Control-of-Quad-Rotor-Balasubramanian-Vasantharaj/0a633124c8c3991d10f0b0205b2076bb3a4795f9.

[98] J. Azinheira. Controlo de Voo. Jan. 2009. URL basedados.aeroubi.pt.

[99] A. Moutinho and R. J. Azinheira. Drone X - Introduction. May 2018.

[100] R. W. Beard. *Quadrotor Dynamics and Control*. PhD thesis, Brigham Young University, Feb. 2008.

[101] A. Moutinho and R. J. Azinheira. DroneX -Analise. May 2018.

[102] H. t. M. N. ElKholy. *Dynamic Modeling and Control of a Quadrotor Using Linear and Nonlinear Approaches*. PhD thesis, The American University in Cairo, 2014.

[103] Z. Tahir, M. Jamil, S. Liaqat, L. Mubarak, W. Tahir, and S. Gilani. State Space System Modeling of a Quad Copter UAV. *Indian Journal of Science and Technology*, 9, July 2016. doi: 10.17485/ijst/2016/v9i27/96613.

[104] A. Moutinho and R. J. Azinheira. DroneX - Modelação. May 2018.

[105] A. Moutinho and R. J. Azinheira. DroneX - Controlo. May 2018.

[106] Thorlabs. PID Tutorial. URL https://www.thorlabs.com/tutorials.cfm?tabID=5DFCA308-D07E-46C9-BAA0-4DEFC5C40C3E.

[107] Ashish Singla. Figure 3 Auto and manually tuned PID v/s PD controllers. URL https://www.researchgate.net/figure/Auto-and-manually-tuned-PID-v-s-PD-controllers_fig9_287208133.

[108] J. G. Leishman. *Principles of Helicopter Aerodynamics*. Cambridge University Press, Dec. 2002. ISBN 9780521523967.

[109] A. M. Kamal and A. Ramirez-Serrano. Design methodology for hybrid (VTOL + Fixed Wing) unmanned aerial vehicles. 2(3):165–176, 2018.

[110] AvStop. Load Factors in Steep Turns. URL http://avstop.com/ac/flighttrainghandbook/loadfactorsinsteepturns.html.

[111] E. B. Davis. Aerodynamic force interactions and measurements for micro quadrotors. 2018.

[112] G. Hoffmann, H. Huang, S. Waslander, and C. Tomlin. Quadrotor Helicopter Flight Dynamics and Control: Theory and Experiment. Aug. 2007. doi: 10.2514/6.2007-6461.

[113] The Engineering Toolbolx. Drag Coefficient. URL https://www.engineeringtoolbox.com/drag-coefficient-d_627.html.

[114] C. F. Heddleson, D. L. Brown, and R. T. Cliffe. SUMMARY OF DRAG COEFFICIENTS OF VARIOUS SHAPED CYLINDERS. Technical Report APEX-299, General Electric Co. Aircraft Nuclear Propulsion Dept., Cincinnati, Apr. 1957. URL https://www.osti.gov/biblio/4373890.